

AD-A060 395 ILLINOIS UNIV AT URBANA-CHAMPAIGN COORDINATED SCIENCE LAB F/G 17/1  
SURFACE ACOUSTIC WAVE TRANSDUCER STUDY.(U)  
MAY 78 B J HUNSINGER

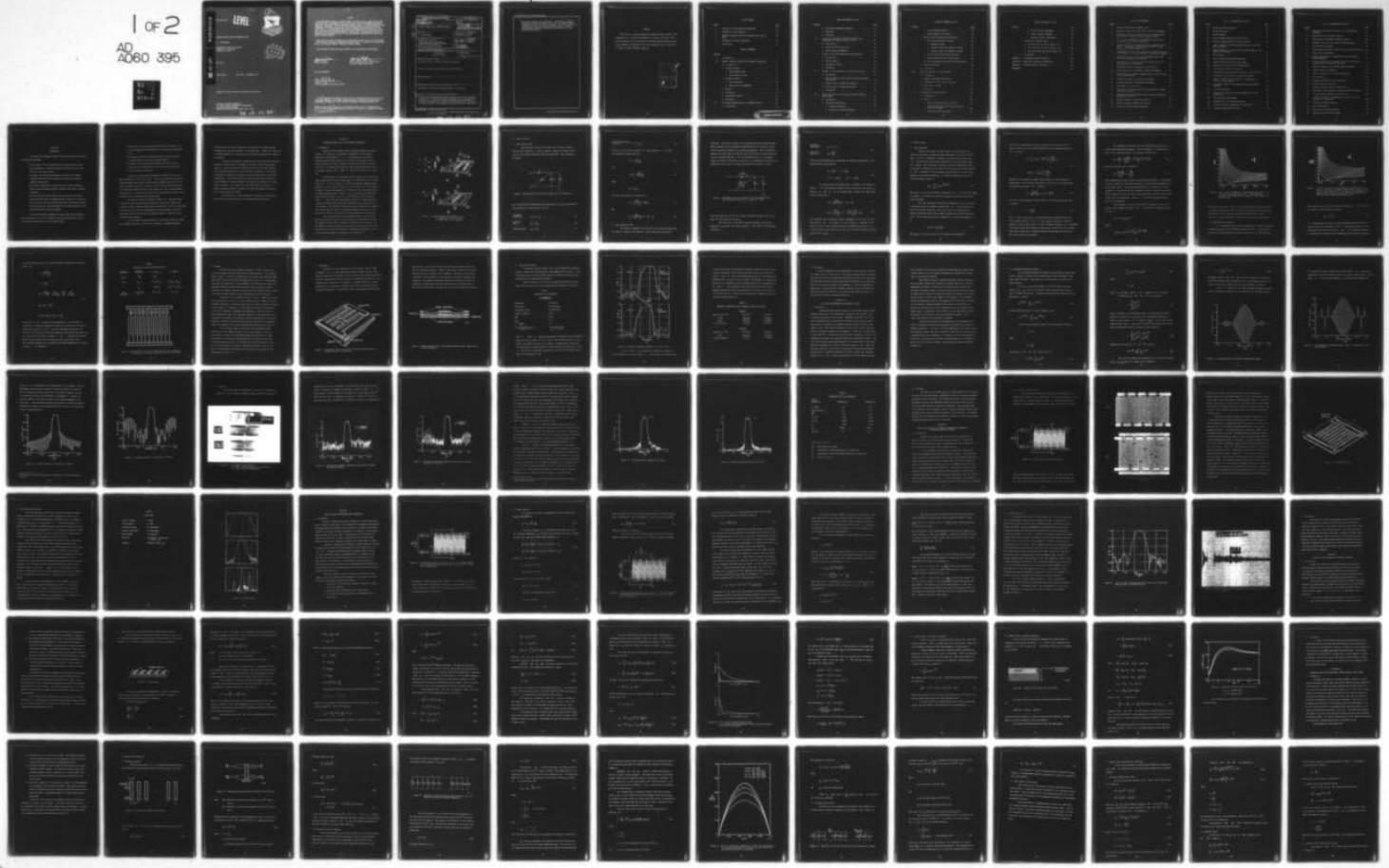
F33615-75-C-1291

UNCLASSIFIED

AFAL-TR-78-60

NL

1 of 2  
AD  
A060 395



AD A060395

AFAL-TR-78-60

LEVEL II



SURFACE ACOUSTIC WAVE TRANSDUCER STUDY

B. J. Hunsinger

Coordinated Science Laboratory  
University of Illinois  
Urbana, IL 61801



May 1978

DDC FILE COPY

Final Report

May 1975 - September 1977

Approved for public release; distribution unlimited.

AIR FORCE AVIONICS LABORATORY  
AIR FORCE WRIGHT AERONAUTICAL LABORATORIES  
AIR FORCE SYSTEMS COMMAND  
WRIGHT-PATTERSON AIR FORCE BASE, OHIO 45433

78 10 16 003

NOTICE

When Government drawings, specifications, or other data are used for any purpose other than in connection with a definitely related Government procurement operation, the United States Government thereby incurs no responsibility nor any obligation whatsoever; and the fact that the government may have formulated, furnished, or in any way supplied the said drawings, specifications, or other data, is not to be regarded by implication or otherwise as in any manner licensing the holder or any other person or corporation, or conveying any rights or permission to manufacture, use, or sell any patented invention that may in any way be related thereto.

This report has been reviewed by the Information Office (OI) and is releasable to the National Technical Information Service (NTIS). At NTIS, it will be available to the general public, including foreign nations.

This technical report has been reviewed and is approved for publication.

James E. Adair  
JAMES E. ADAIR  
Project Engineer

Alan R. Mertz  
ALAN R. MERTZ, CAPT., USAF  
Chief, Microwave Tech. & Appl Group  
Microwave Technology Branch

FOR THE COMMANDER

DONALD S. REES  
DONALD S. REES  
Chief, Microwave Technology Branch

"If your address has changed, if you wish to be removed from our mailing list, or if the addressee is no longer employed by your organization please notify AFAL/DHM, N-PAGE, OH 45433 to help us maintain a current mailing list".

Copies of this report should not be returned unless return is required by security considerations, contractual obligations, or notice on a specific document.

SECURITY CLASSIFICATION OF THIS PAGE (When Data Entered)

<b>REPORT DOCUMENTATION PAGE</b>		<b>READ INSTRUCTIONS BEFORE COMPLETING FORM</b>
1. REPORT NUMBER <b>(18) AFAL TR-78-60</b>	2. GOVT ACCESSION NO.	3. DISTRIBUTION/CATALOG NUMBER
4. TITLE (and Subtitle) <b>Surface Acoustic Wave Transducer Study</b>		5. TYPE OF REPORT & PERIOD COVERED <b>FINAL REPORT, 28 May 75 - 30 Sep 77</b>
6. AUTHOR(s) <b>B. J. Hunsinger</b>	7. CONTRACT OR GRANT NUMBER(s) <b>(15) F33615-75-C-1291</b>	8. PROGRAM ELEMENT PROJECT, TASK & WORK UNIT NUMBERS <b>(16) 20020346 (17) 03</b>
9. PERFORMING ORGANIZATION NAME AND ADDRESS <b>University of Illinois Coordinated Sciences Laboratory Urbana, Champaign County, Ill 61801</b>	10. REPORT DATE <b>(11) May 1978</b>	11. NUMBER OF PAGES
11. CONTROLLING OFFICE NAME AND ADDRESS <b>Air Force Avionics Laboratory Air Force Wright Aeronautical Laboratories Wright Patterson AFB, OH 45433</b>	12. SECURITY CLASS. (of this report) <b>UNCLASSIFIED</b>	13. DECLASSIFICATION/DOWNGRADING SCHEDULE
14. MONITORING AGENCY NAME & ADDRESS (if different from Controlling Office) <b>(12) 162p</b>	15. DISTRIBUTION STATEMENT (of this Report)  Approved for public release; distribution unlimited.	
16. DISTRIBUTION STATEMENT (of the abstract entered in Block 20, if different from Report)		
17. SUPPLEMENTARY NOTES		
18. KEY WORDS (Continue on reverse side if necessary and identify by block number)  <b>Transducers, Filters Surface Acoustic Waves. IC capacitors</b>		
19. ABSTRACT (Continue on reverse side if necessary and identify by block number)  <b>A theoretical and experimental study of surface acoustic wave transducers is carried out to improve the modeling technique and the implementation configuration. The capacity weighted transducer with the response controlled by integrated circuit capacitors has been developed. The response is improved because the SAW beam has a uniform width and the transducer</b>		

DD FORM 1 JAN 73 1473 EDITION OF 1 NOV 65 IS OBSOLETE

097700 SECURITY CLASSIFICATION OF THIS PAGE (When Data Entered) 5B

10 16 003

~~SECURITY CLASSIFICATION OF THIS PAGE(When Data Entered)~~

taps may be adjusted over a wide range. The excitation theory of transducers has been reformulated to account for nearest neighbor interactions over a wide range of harmonics. This modeling approach significantly expands the versatility and accuracy of the model. An experimental procedure for measuring the transducer excitation function is described.

~~SECURITY CLASSIFICATION OF THIS PAGE(When Data Entered)~~

## PREFACE

The ability to accurately model and implement surface acoustic wave transducers is of significant importance to the U.S. Air Force. This report describes a new more versatile transducer modeling technique and a new transducer configuration that uses integrated circuit capacitors to control the SAW transducer response.

ACCESSION for	
NTIS	White Section <input checked="" type="checkbox"/>
DDC	Buff Section <input type="checkbox"/>
UNANNOUNCED <input type="checkbox"/>	
JUSTIFICATION	
BY	
DISTRIBUTION/AVAILABILITY CODES	
REF	SL and/or SPECIAL
A	-

## LIST OF TABLES

TABLE		PAGE
1	Comparison of tap weighting techniques.	16
2	Parameters of CW transducer.	20
3	Measured impedance and loss parameters that verify model.	22
4	Parameters for test transducers.	37
5	CW-UDT data.	44

## TABLE OF CONTENTS

SECTION		
I.	Introduction . . . . .	1
II.	Reduced Reactance Capacitively Weighted Transducers . . . . .	4
	A. Introduction . . . . .	4
	B. Single Tap Model . . . . .	6
	1. Ideal Lossless Case . . . . .	6
	2. Lossy Dielectric Case . . . . .	7
	C. Multistrip Model . . . . .	10
	1. Input Admittance . . . . .	10
	2. Optimization of Parameters . . . . .	12
	D. Design . . . . .	17
	E. Fabrication . . . . .	18
	F. Experimental Results . . . . .	20
	G. Conclusion . . . . .	23
III.	Tap Weighted Enhancement for Broadband Filters . . . . .	23
	A. Introduction . . . . .	23

TABLE OF CONTENTS (cont'd)

SECTION		PAGE
	B. Tap Weight Enhancement Analysis . . . . .	25
	C. Experiment . . . . .	31
	D. Conclusion . . . . .	38
IV.	Group Type Capacitively Weighted Unidirectional Transducers for Highly Selective Filters . . . . .	38
	A. Introduction . . . . .	38
	B. Group Type CW-UDT Structure . . . . .	39
	C. Filter Design and Results . . . . .	43
V.	Tuning of Group Type Unidirectional Transducers . . . . .	46
	A. Introduction . . . . .	46
	B. Network Analysis . . . . .	48
	C. Experimental Results . . . . .	53
	D. Conclusions . . . . .	56
VI.	Analysis of SAW Propagation in Layered Structures . . . . .	56
	A. Introduction . . . . .	56
	B. Surface Waves on a Free Surface with an Electrical Open Circuit . . . . .	58
	C. Surface Waves on Conductive Surfaces . . . . .	66
	D. Surface Waves in Layered Structures . . . . .	67
	E. Conclusions . . . . .	70
VII.	Scattering Model for Electrically Coupled Periodic Metal Strips . . . . .	70
	A. Introduction . . . . .	70
	B. Theoretical Formulation . . . . .	72
	1. Transmission Matrix . . . . .	72
	2. Evaluation of Matrix Elements . . . . .	74

TABLE OF CONTENTS (cont'd)

SECTION		PAGE
	3. Strip Resistance Losses . . . . .	79
	4. Normal Modes of the Coupler . . . . .	81
C.	C. Special Cases with Analytical Solutions . . . . .	82
	1. Two Track Surface Wave Coupler . . . . .	82
	a. Identical Tracks . . . . .	83
	b. Unequal Tracks with Identical Periods . . .	84
	c. Unequal Tracks with Different Periods . . .	84
	2. Strip Coupled Surface Wave Amplifier . . . . .	85
	3. Normal Modes of the Two Track Coupler . . . . .	86
	4. Strip Resistance Losses for Two Track Coupler .	87
D.	D. Numerical Analysis . . . . .	88
E.	E. Conclusion . . . . .	91
VIII.	VIII. Harmonic Analysis of SAW Transducers . . . . .	91
	A. Introduction . . . . .	91
	B. Sampled Time Domain Calculations . . . . .	92
	C. Segregation of Time Limited Responses . . . . .	94
	D. Experimental Results . . . . .	96
	E. Conclusion . . . . .	102
IX.	IX. A Generalized Transducer Model . . . . .	103
	A. Introduction . . . . .	103
	B. Theory . . . . .	105
	1. Basic Charge Distribution Function . . . . .	106
	2. Charge Distribution in Periodic Array with Arbitrary Voltages . . . . .	109
	3. Transducer Input Admittances . . . . .	114

TABLE OF CONTENTS (cont'd)

SECTION	PAGE
a. Direct Coupled, Unapodized . . . . .	114
b. Direct Coupled, Apodized . . . . .	116
c. Capacity Coupled, Unapodized . . . . .	120
C. Evaluation of Special Cases . . . . .	126
1. Two Electrodes per Period (Figure 54a) . . . . .	126
2. Four Electrodes per Period (Figure 54b) . . . . .	128
3. Three Electrodes per Period (Figure 54c) . . . . .	130
D. Conclusions . . . . .	132
Appendix A: Time-Domain Analysis Procedure . . . . .	133
Appendix B: Time-Domain Analysis Implementation . . . . .	143
Appendix C: Modified Laguerre Polynomials . . . . .	145
REFERENCES . . . . .	147

LIST OF ILLUSTRATIONS

FIGURE		PAGE
1	Capacity weighted SAW transducer taps.	5
2	Equivalent circuit for ideal single tap of CW transducer.	6
3	Equivalent circuit for single tap of CW transducer where the attenuator capacitors have dielectric losses.	8
4	Plot of the CW transducer Q, normalized by the value of $Q_R$ , versus $\alpha_R$ for various values of $S'$ .	13
5	Plot of the ratio of the thin film loss inductance to the acoustic conductance, normalized with respect to $Q_R/Q_T$ , versus $\alpha_R$ for various values of $S'$ .	14
6	Representation of thin film capacitors as ideal attenuators for weighting of the taps connected to the positive bus bar.	16
7	Perspective view of a tap in a CW transducer where each electrode represents 1/8 wavelength.	18
8	Cross sectional view of the layered structure used in fabricating the CW transducer.	19
9	Unmatched frequency responses of Filter A and B.	21
10	Conventional set of periodically spaced tap weights.	27
11	Corresponding tap enhanced weights using a 4:1 compression in the time sidelobes.	28
12	Frequency response of reference tap weights.	29
13	Frequency response of compressed tap weights.	30
14	Photograph of actual device.	31
15	Superimposed unmatched theoretical and measured frequency response for Filter A.	32
16	Superimposed unmatched theoretical and measured frequency response for Filter B.	33
17	Matched frequency response for Filter A.	35
18	Matched frequency response for Filter B.	36
19	Group type unidirectional transducer.	39

LIST OF ILLUSTRATIONS (cont'd)

FIGURE		PAGE
20	CW-UDT metalization pattern.	40
21	CW-UDT perspective.	42
22	CW-UDT response.	45
23	Series tuning approach for block type UDT.	47
24	Parallel tuning approach for block type UDT.	49
25	Filter frequency response measured relative to a 41 MHz center frequency.	54
26	Impulse response of filter with the triple transit 44 dB below the main signal.	55
27	Surface waves.	58
28	Plot of field distributions with depth.	64
29	Layered structure with $\text{SiO}_2$ over $\text{LiTaO}_3$ .	67
30	Variation of velocity with film thickness.	69
31	A multistrip coupler with M tracks.	72
32	Incoming and outgoing waves in M tracks of the $n^{\text{th}}$ strip.	73
33	Equivalent circuit for one strip with M tracks.	75
34	Ratio of single strip conductance to capacitance as a function of strip period.	78
35	Equivalent circuit for one strip with strip resistance included.	79
36	A strip-coupled UDT.	89
37	Reverse to forward ratio versus frequency for a strip coupled UDT.	90
38	Time frequency relationship.	92
39	Segregation of time limited responses.	94
40	Transfer function representation of SAW device.	95
41	Original measured harmonic data.	98

LIST OF ILLUSTRATIONS (cont'd)

FIGURE		PAGE
42	Frequency response after deletion of all non-SAW time components.	99
43	Theoretically derived phase function.	100
44	Experimentally calculated excitation function.	100
45	Comparison with four term Fourier series expansion.	101
46	Periodic array transducer.	106
47	Basic Charge Distribution Function in a single tap structure.	107
48	Element factor parameters.	110
49	Charge distribution in a periodic array with arbitrary voltage sequences.	111
50	Charge distribution in a periodic array as a superposition of basic charge distribution functions.	113
51	Apodized transducer with shorted dummy electrodes.	117
52	Capacity weighted transducer.	121
53	Spectral response due to capacitive couplers.	124
54	IDT structures.	127
55	Radiation conductance for IDT structures.	129
A1	Harmonic analysis flow chart.	136
A2	Original measured harmonic magnitude data.	137
A3	Measurement system harmonic frequency response magnitude.	137
A4	Initial impulse response time shift to t=0.	138
A5	Frequency response of fundamental after deletion of all non-SAW time components.	139
A6	Composite frequency response.	140
A7	Auto deconvolution.	141
A8	Phase offsets between harmonics.	142
A9	Measurement system block diagram.	144

## SECTION I

### INTRODUCTION

A universal SAW transducer theory and structure has been developed having these advantages

- \* A wide range of center frequencies may be achieved with a given electrode spacing - single electrode and double electrode transducers are two special cases.
- \* A general theory has been developed to provide the transducer frequency response over all harmonics accounting for nearest neighbor interactions.
- \* The theory is applicable to general periodic array transducers which include withdrawal weighted, apodized, and capacity coupled structures.
- \* The filter design is more direct since the affect of electrode structure on the overall response has been reduced to a single tap filter function that may be deconvolved from the specified response. The tap weights are then determined by an inverse transform of the modified specified frequency response.

The capacity weighted transducer structure which uses integrated circuit capacitors to control the response has been improved significantly over the structure described in the interim report.

- \* The response accuracy has been improved with the realization of precise nonsymmetrical pass bands having selectivities exceeding 55 db.
- \* The coupling structure and design procedure has been improved for lower insertion loss and increased bandwidth.
- \* A unidirectional structure with weighted taps has resulted in filters with 55 db selectivity, 6 dB insertion loss and 44 dB of triple transit suppression.

This report details these developments and builds on the information presented in the interim report. That report describes the sampled impulse response filter design concept and the original description of the capacity weighted structure. Section II and III deals with modifications to the capacity weighted structure that reduce loss, and increase bandwidth and selectivity. Sections IV and V describe the weighted tap unidirectional transducer and the associated matching networks.

The capacity weighted transducer consists of a layered structure in which the lower electrodes are essentially a multistrip coupler (MSC) coupled by lumped element integrated circuit capacitors. Section VI describes a new theory which simplifies the analysis of SAW propagation in layered structures and Section VII derives a powerful element by element circuit approach to MSC analysis.

The time domain analysis described in the interim report provided the amplitude and phase of each tap for purposes of transducer analyses.

With the advent of harmonic operation of SAW devices it becomes necessary to analyze the excitation function of individual taps. Section VIII describes a technique whereby the fine structure of the single tap excitation function is measured.

Section IX describes a universal theory for predicting the harmonic response of a wide range of transducers utilizing a newly defined basis function. Former theories have used the electrode as the basis function. Since the charge distribution on an electrode is dependent on the voltage of neighboring elements the response of each electrode must be determined individually. This newly defined basis function described in Section IX is not dependent on nearest neighbors and the analysis reduces to a simple Fourier transform. The simplicity of the theory makes it possible to analyze withdrawal weighted, apodized, and capacity weighted transducers with the same design algorithms.

The combination of these theoretical technological developments have contributed significantly to the universal SAW device design.

## SECTION II

### REDUCED REACTANCE CAPACITIVELY WEIGHTED TRANSDUCERS

#### A. Introduction

The capacitive tap weight network transducer (CTWN) has been presented in the interim as an alternative to apodization for the dynamic weighting of SAW transducers [1, 2]. The CTWN transducer provides a uniform beam width which allows direct cascading of two weighted filters without a multistrip coupler. However, the uniform beam width is obtained at the cost of a higher filter Q than a similar apodized device which leads to increased insertion loss. Figure 1a shows the structure for a single tap.

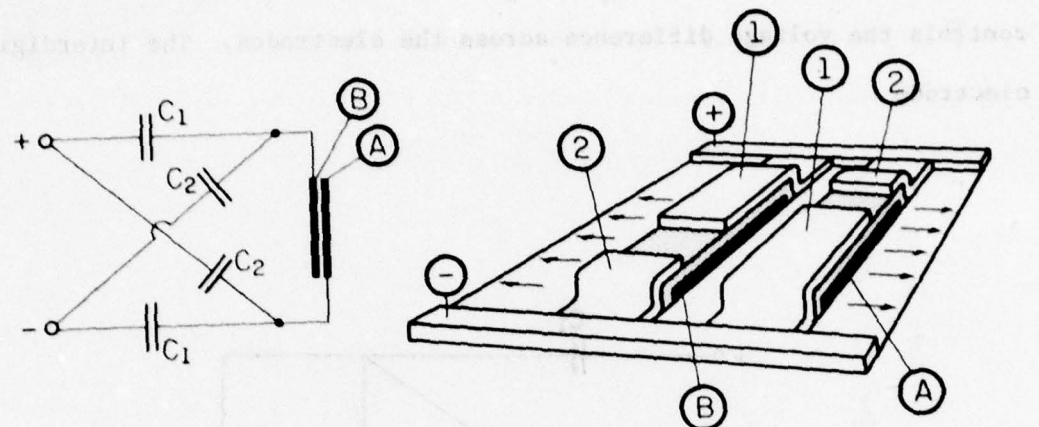
A modification of the original structure results in a significantly lower transducer Q while maintaining dynamic tap weighting and a uniform beam width [3]. This new structure of capacitive weighting, hereafter simply referred to as CW, is shown in Figure 1b for a single tap. The structural difference is merely the grounding of electrode A in the CW transducer while the CTWN transducer allows electrode A to have an applied voltage dependent on the capacitor values of  $C_1$  and  $C_2$ . The equivalent circuits, shown in Figure 1 reveal that the tap attenuator network for a CTWN transducer is a capacitive bridge circuit while the CW transducer has a capacitive attenuator network. This structural modification greatly reduces the CW transducer's input capacitance with respect to the CTWN transducer resulting in a lower device Q and lower filter insertion loss for broadband filter applications.

This section describes the CW transducer model, which takes the thin film capacitor dielectric losses in account, and presents the detailed CW transducer design analysis necessary for bandpass filter synthesis. The CW, CTWN, and apodized transducers are compared to illustrate the differences and similarities between the structures. Experimental verification is provided using CW transducers in bandpass filter applications.

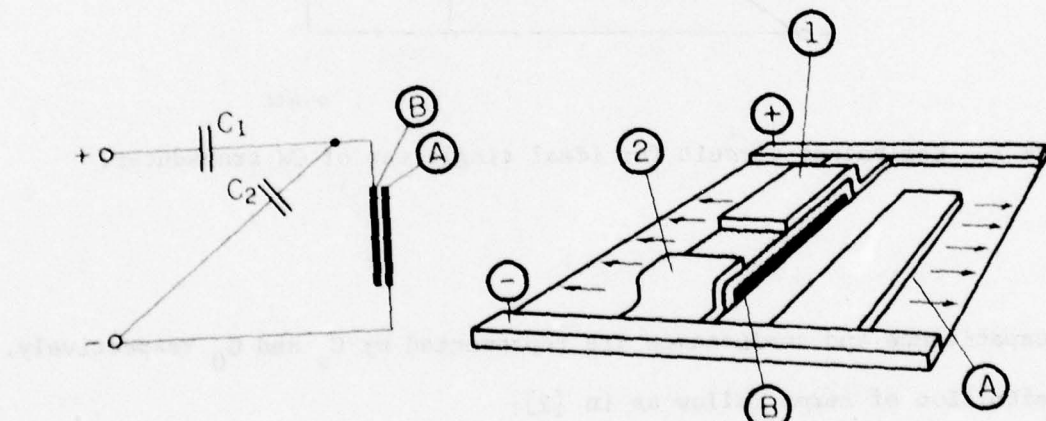
lelectret signal

and configured lead

A single or multi tap SAW transducer has two electrodes with one side deposited on the surface of a substrate and has two conductors with one side deposited on the surface of a substrate with the other side



a)



b)

Figure 1. Capacity weighted SAW transducer taps.

- a) Single tap of CTWN transducer.  
b) Single tap of CW transducer.

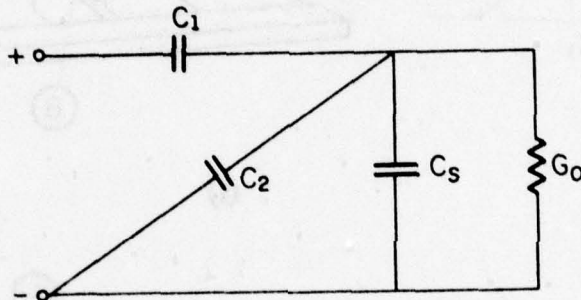
KP-923

## B. Single Tap Model

### 1. Ideal Lossless Case

The equivalent circuit for a single tap is shown in Figure 2.

The thin film capacitors,  $C_1$  and  $C_2$ , compose a reactive attenuator which controls the voltage difference across the electrodes. The interdigital electrode



KP-1403

Figure 2. Equivalent circuit for ideal single tap of CW transducer.

pair capacitance and conductance are represented by  $C_s$  and  $G_0$  respectively.

The definition of terms follow as in [2]:

attenuator capacitance  $C_T = C_1 + C_2$  (1)

reactance ratio  $\alpha_R = C_s / C_T$  (2)

attenuator gain  $\alpha_w = C_1 / C_T$  (3)

capacitive coupling coefficient  $K^2 = (1 + \alpha_R)^{-2}$

Solution of the network of Figure 1b using equations 1 - 4 yields the attenuator transfer function

$$|A| = \frac{\alpha_w}{(1 + \alpha_R)} \quad (5)$$

and

$$\arg |A| = \frac{\alpha_R Q_o^{-1}}{(1 + \alpha_R)} \quad (6)$$

where

$$Q_o = \omega C_s / G_o$$

The input admittance for a single tap is

$$G_a' = \frac{\alpha_w^2 G_o}{(1 + \alpha_R)^2} = \alpha_w^2 K^2 G_o \quad (7)$$

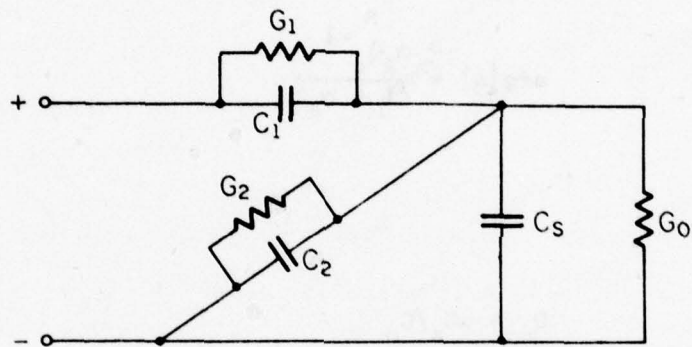
and

$$C_o' = \frac{\alpha_w C_s}{\alpha_R (1 + \alpha_R)} (1 + \alpha_R - \alpha_w) \quad (8)$$

## 2. Lossy Dielectric Case

The apodized transducer has thin film losses associated only with the metallic conductors and dielectric losses within the piezoelectric

substrates. The resistive losses are calculated using the conductor material, sheet resistance and the transducer beam width while the dielectric losses in the piezoelectric material are generally negligible. The CW transducer, however, has both conductor losses and thin film dielectric losses associated with the coupling capacitors. For the following analysis, it is assumed either the metallic conductance is infinite or is combined with the dielectric conductance loss to yield an effective dielectric conductance. Figure 3



KP-1402

Figure 3. Equivalent circuit for single tap of CW transducer where the attenuator capacitors have dielectric losses.

shows the equivalent circuit for a single tap when including a loss conductance for each capacitor  $C_1$  and  $C_2$ .

The total area of the upper electrodes determine the relative magnitude of  $C_T$  and the thin film conductance. This leads to the following definitions:

attenuator  
conductance

$$G_T = G_1 + G_2$$

(9)

thin film  
dielectric Q

$$Q_T = \frac{\omega C_o}{G_T}$$

The thin film capacitance and conductance are directly proportional to the upper electrode area yielding

$$C_1 = \alpha_w C_T; \quad G_1 = \alpha_w G_T$$

(10)

$$C_2 = (1 - \alpha_w) C_T; \quad G_2 = (1 - \alpha_w) G_T$$

The following results assume  $Q_T \gg 1$ . Solution of the network of Figure 3 for the attenuator transfer function yields the same results as given in (5) and (6) for the lossless case. However, the input admittance of the network is

$$C_{IN} = \frac{\alpha_w C_s}{\alpha_R (1 + \alpha_R)} (1 + \alpha_R - \alpha_w) \quad (11)$$

$$G_{IN} = \frac{\alpha_w^2 G_o}{(1 + \alpha_R)^2} + \left(1 - \frac{\alpha_w (1 + 2\alpha_R)}{(1 + \alpha_R)^2}\right) \alpha_w G_T \quad (12)$$

The transducer input capacitance remains unchanged from the ideal lossless case given in (8). The input conductance, however, is composed of two terms; the first term yielding the acoustic conductance as given in (7) and the bracketed term being the thin film loss conductance which is directly proportional to  $\alpha_w G_T$ .

### C. Multitap Model

#### 1. Input Admittance

Based on the single tap model results, it is now possible to determine the impulse response and input admittance for a multitap transducer. Since it is desirable to maintain a constant delay between taps, (6) dictates that  $\alpha_K$  must remain constant for every tap, which implies  $K$  is constant. The tap weights, therefore, are set by appropriate choice of  $\alpha_w$  which is determined by the upper electrode area that defines capacitor  $C_1$ . This is analogous to the tap weight being proportional to the finger overlap of an apodized transducer. For uniformly spaced electrodes, the effective number of taps is:

$$N_{\text{eff}} = \sum_{n=1}^N \alpha_w(n) e^{j2\pi f_o \tau_o n} \quad (13)$$

where  $\alpha_w(n)$  is the  $n$ -th tap weight as defined in (3),  $N$  is the total number of fingers,  $\tau_o$  corresponds to the delay between taps and  $f_o$  is the filter center frequency.

The input admittance for a multitap transducer at center frequency is determined using the impulse response model [4] and the single tap analysis previously described. The acoustic and loss conductances are analyzed separately since both are small compared to the capacitive susceptibility. The CW transducer acoustic conductance is found upon expanding (7) as

$$G'_a(\omega_o) = N_{\text{eff}}^2 K^2 G_o \quad (14)$$

where  $N_{\text{eff}}$  is the vector sum of the tap weights as determined in

The total loss conductance term due to the thin film dielectric for N parallel taps is the sum of each individual tap loss conductance given in (12) yielding

$$G_{TF} = \sum_{n=1}^N (\alpha_w(n) - \overline{\alpha_w^2}) \frac{(1 + 2\alpha_R)}{(1 + \alpha_R)^2} G_T \quad (15)$$

$$= N \alpha_w G_T (1 - \overline{\alpha_w^2} / \alpha_w^2) \frac{(1 + 2\alpha_R)}{(1 + \alpha_R)^2}$$

where  $\overline{\alpha_w}$  is the average tap weight value and  $\overline{\alpha_w^2}$  is the mean squared tap weight value. The transducer capacitance is the sum of all the individual tap capacitances given in (8) yielding

$$C_o' = \frac{\overline{\alpha_w} NC_s}{\alpha_R (1 + \alpha_R)} (1 + \alpha_R - \overline{\alpha_w^2} / \overline{\alpha_w}) \quad (16)$$

The ratio of mean squared tap weight value to the average tap weight value is defined:

$$S' = \overline{\alpha_w^2} / \overline{\alpha_w} \quad (17)$$

This is a useful term since it provides qualitative information about the device impulse response. For  $S' = 1$ ,  $\overline{\alpha_w^2} = \overline{\alpha_w}$  which requires all the tap weights to be unity and yields a  $\sin(x)/x$  frequency response. As  $S'$  approaches 0, the mean squared tap weights are approaching 0 faster than the tap weight value which transforms to frequency responses having high selectivity and very narrow transition bandwidths.

The transducer Q and thin film loss are determined using the calculated input admittance parameters. The CW transducer Q is defined as the ratio of the input susceptance to the acoustic conductance as

$$Q'_R = \frac{\omega_o C'_o}{G'_a} = \frac{\omega_o C_s \overline{N\alpha_w}}{G_o N_{eff}}^2 \frac{(1 + \alpha_R - S') (1 + \alpha_R)}{\alpha_R} \quad (18)$$

The first bracketed term is defined as

$$Q_R = \frac{\omega_o C_s \overline{N\alpha_w}}{G_o N_{eff}}^2 = Q_o \frac{\overline{N\alpha_w}}{N_{eff}^2} \quad (19)$$

and is approximately equal to the Q of an apodized transducer. The magnitude of  $Q_R$  is a function of the substrate material, filter percent bandwidth and filter shape factor. The second term in brackets is a function of  $S'$  and  $\alpha_R$  where  $S'$  is determined by the tap weights necessary to achieve the desired filter response and  $\alpha_R$  is the ratio of the electrode to electrode capacitance to the thin film capacitance. Figure 4 is the plot of  $Q'_R/Q_R$  versus  $\alpha_R$  with  $S'$  as a parameter.

The magnitude of the thin film loss is determined by the ratio of the thin film conductance given in (15) to the acoustic conductance given in (14) as

$$L_{TF} = (1 + G_{TF}/G'_a)^{-1}$$

where

$$G_{TF}/G'_a = Q_R/Q_T \frac{(1 + \alpha_R)^2 - S'(1 + 2\alpha_R)}{\alpha_R} \quad (20)$$

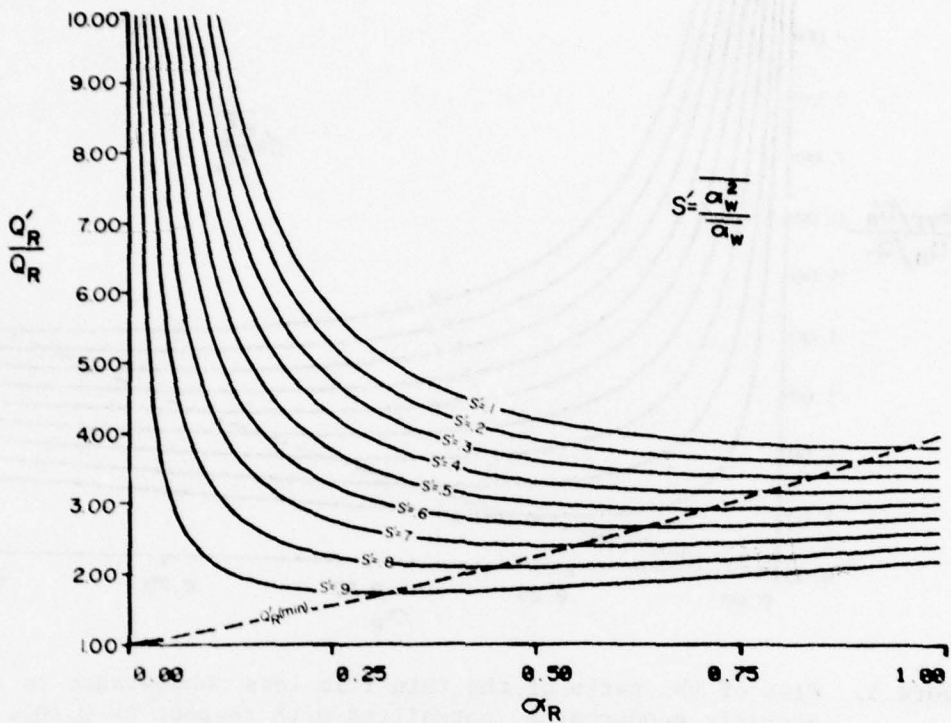


**Figure 4.** Plot of the CW transducer  $Q'$ , normalized by the value of  $Q_R$ , versus  $\alpha_R$  for various values of  $S'$ . The dashed curve represents the minimum value of  $Q'_R/Q_R$  for every value of  $\alpha_R$  between 0 and 1.

The ratio of  $Q_R$  given in (19) to the thin film dielectric  $Q_T$  determines the relative magnitude of the loss. Thin film dielectrics with high  $Q$  and narrow band filters having low  $Q_R$  minimize the loss term. Figure 5 is the plot of  $G_{TF}/G_a'$  normalized to  $Q_R/Q_T$  versus  $\alpha_R$  with  $S'$  as a parameter.

## 2. Optimization of Parameters

It is desirable for most filter applications to obtain the minimum transducer  $Q'$  while also minimizing the thin film loss. The only design variable not yet determined by the filter response is  $\alpha_R$ . The value of  $\alpha_R$

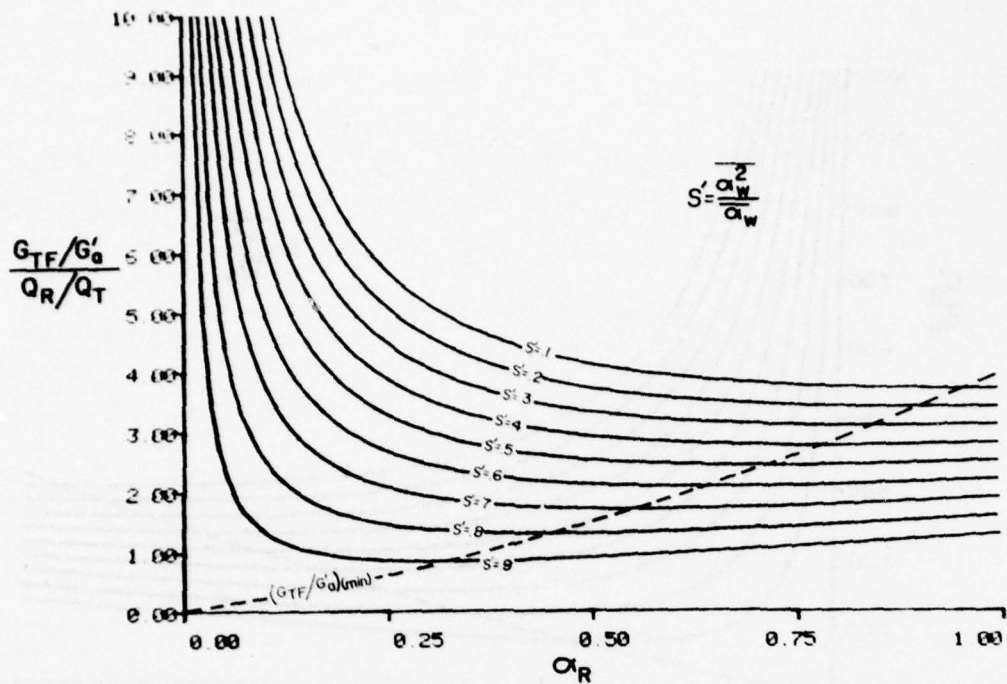


Figure 5. Plot of the ratio of the thin film loss conductance to the acoustic conductance, normalized with respect to  $Q_R/Q_T$ , versus  $\alpha_R$  for various values of  $S'$ . The dashed curve represents the minimum value of  $G_{TF}/G'_0$  (which yields the lowest thin film loss) for every value of  $\alpha_R$  between 0 and 1.

which minimizes  $Q'_R$  is found by taking the derivative of (18) and setting the result to zero yielding the solution

$$\alpha'_R = \sqrt{1 - S'} \quad (21)$$

In a similar manner the value of  $\alpha_R$  which minimizes the thin film loss is found by taking the derivative of (20) and setting the result to zero which yields the same solution as in (21). It is possible, therefore, to simultaneously minimize the CW transducer  $Q'_R$  and the thin film loss by

using the optimum value of  $\alpha'_R$ . The CW transducer parameters are rewritten using (21).

$$G'_a = \frac{N_{eff}^2 G_o}{(1 + \alpha'_R)^2}$$

$$C'_o = \overline{\alpha_w} N C_s$$

$$G_{TF} = \frac{N \overline{\alpha_w} \omega_o C_s}{Q_T} \quad \frac{2\alpha'_R}{(1 + \alpha'_R)} = \frac{\omega_o C'_o}{Q_T} \quad \frac{2\alpha'_R}{(1 + \alpha'_R)}$$

(22)

$$Q'_R = Q_R (1 + \alpha'_R)^2$$

$$G_{TF}/G'_a = Q_R/Q_T [2\alpha'_R (1 + \alpha'_R)]$$

The results in (22) show the input capacitance of a CW transducer is identical to an apodized transducer but there is a decrease in the acoustic conductance given by  $(1 + \alpha'_R)^{-2}$ . The loss conductance term due to the dielectric film is easily calculated knowing the device design and dielectric  $Q_T$ . The broken line curves in Figures 4 and 5 represent the minimum  $Q'_R$  and loss term when using the optimized value of  $\alpha'_R$  given in (21). The transducer parameters for apodized, CW and CTWN transducers are provided in Table 1 for comparison.

TABLE 1  
COMPARISON OF TAP WEIGHTING TECHNIQUES

<u>Parameter</u>	<u>APODIZED</u>	<u>CW</u>	<u>CTWN</u>
$C_{IN}/C_s$	$\overline{N\alpha_w}$	$\overline{N\alpha_w}$	$N$
$G_a/G_o$	$N_{eff}^2$	$(1+\alpha_R)^{-2} N_{eff}^2$	$(1+2\alpha_R)^{-2} N_{eff}^2$
$Q$	$Q_R$	$(1+\alpha_R)^2 Q_R$	$\overline{\alpha_w^{-1}} (1+2\alpha_R)^2 Q_R$
<b>Loss Mechanism</b>	Apodization Loss	Thin Film	Thin Film

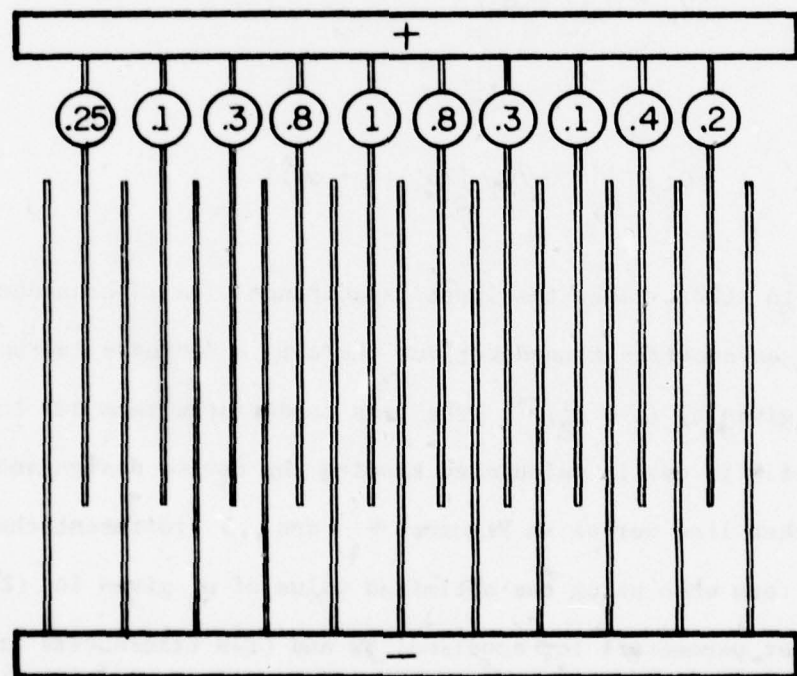


Figure 6. Representation of thin film capacitors as ideal attenuators for weighting of the taps connected to the positive bus bar.

#### D. Design

The desired filter frequency response is Fourier transformed to yield the analogue impulse response which is then sampled. A time sampling rate of  $(2f_o)^{-1}$  is chosen for symmetrical filters and a sampling rate greater than  $(2f_o)^{-1}$  must be chosen for non-symmetrical filters [5]. As previously mentioned, tap weighting for a CW transducer is achieved on only those taps connected between the busbar and the acoustic beam, as shown in Figure 6. Therefore, the negative samples are deleted from the impulse response leaving only positive samples which are then implemented by the CW transducer.

The deletion of the negative taps for a  $(2f_o)^{-1}$  sampling rate gives rise to harmonics at 0 and  $2f_o$  in the frequency domain. However, the total transducer response is obtained by multiplying the sampled frequency response by the response of a single cell. The single cell represents the smallest unit which is repetitive throughout the transducer. Smith and Pedler [6] have obtained the single cell frequency response for single and double electrodes and the analysis also yields the relative magnitudes for the various harmonics. The sharp nulls occurring at the even harmonics for single and double electrodes very effectively suppress the busharmonics at 0 and  $2f_o$ .

Given the tap weights as determined from the sampled impulse response, the total number of taps  $N$ , the effective number of taps  $N_{\text{eff}}$ , the average tap weight and the average squared tap weight are all known. Upon choice of the substrate material and thin film dielectric and given the sampled impulse response, the optimized CW transducer parameters given in (22) are calculated in a simple, straightforward manner. The  $S'$  term may be increased while maintaining the filter integrity by using the tap enhancement procedure [7].

#### E. Fabrication

Fabrication of CW transducers is very similar to that of CTWN transducers [2]. A mask consisting of equally spaced, parallel lines having the same width and length is used to define lower electrodes directly atop the piezoelectric substrate; with all the ground electrodes (i.e., non-weighted taps) connected to a common bus. A suitable dielectric is then deposited (i.e., evaporated, sputtered, etc.) over the entire surface to the desired thickness. A final mask is used to define the upper electrode

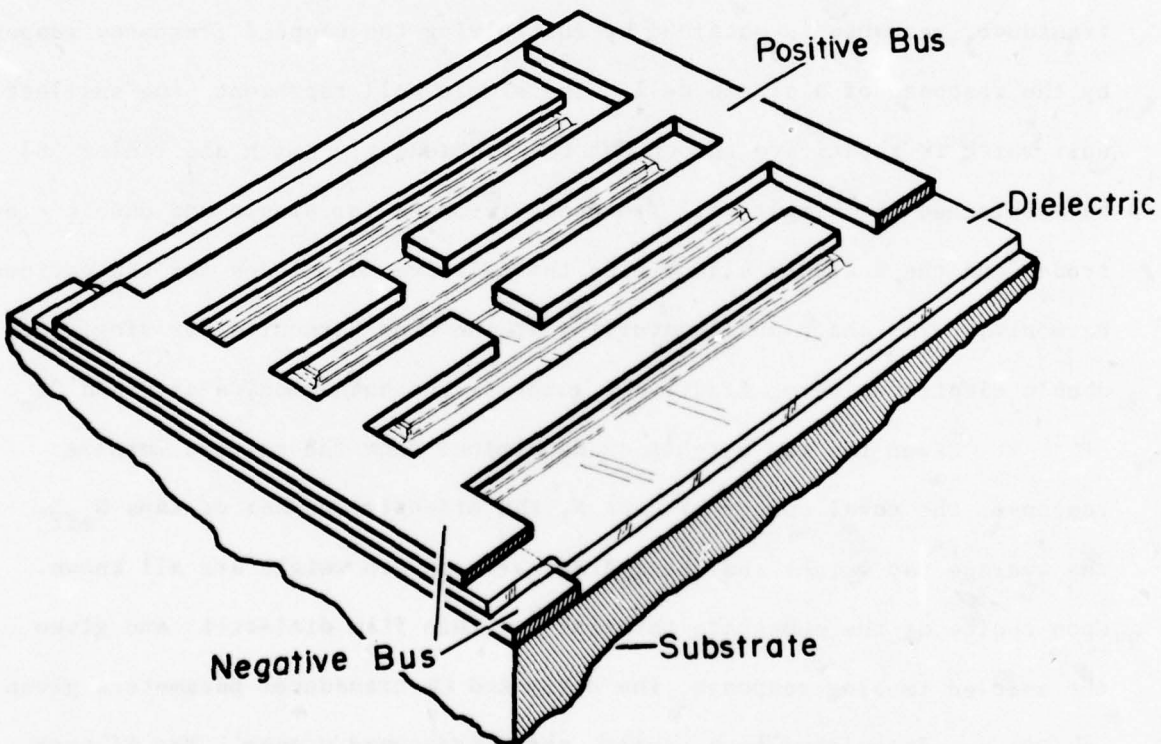
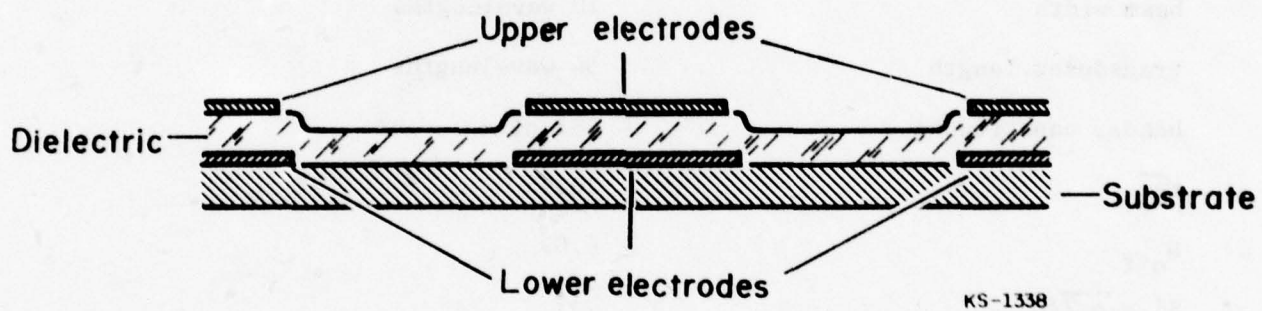


Figure 7. Perspective view of a tap in a CW transducer where each electrode represents 1/8 wavelength.

pattern which is precisely aligned over the lower electrodes forming the capacitor attenuator network. Figure 7 and 8 show a perspective and cross sectional view of a portion of a CW transducer. Each electrode in Figure 7 represents 1/8 wavelength and this structure is periodic throughout the transducer. The negative buses above and below the dielectric layer are capacitively coupled when providing a sufficiently low impedance short or are directly shorted when a suitable hole is provided through the dielectric.



KS-1338

Figure 8. Cross sectional view of the layered structure used in fabricating the CW transducer.

#### F. Experimental Results

To exemplify the most general case, two non-symmetrical frequency response filters are presented using a time sampling rate of  $(4f_0)^{-1}$ . Both filters were built on  $128^\circ$  YX LiNbO<sub>3</sub> with the transducers having 96 micron wavelengths and 10 wavelength beam widths.

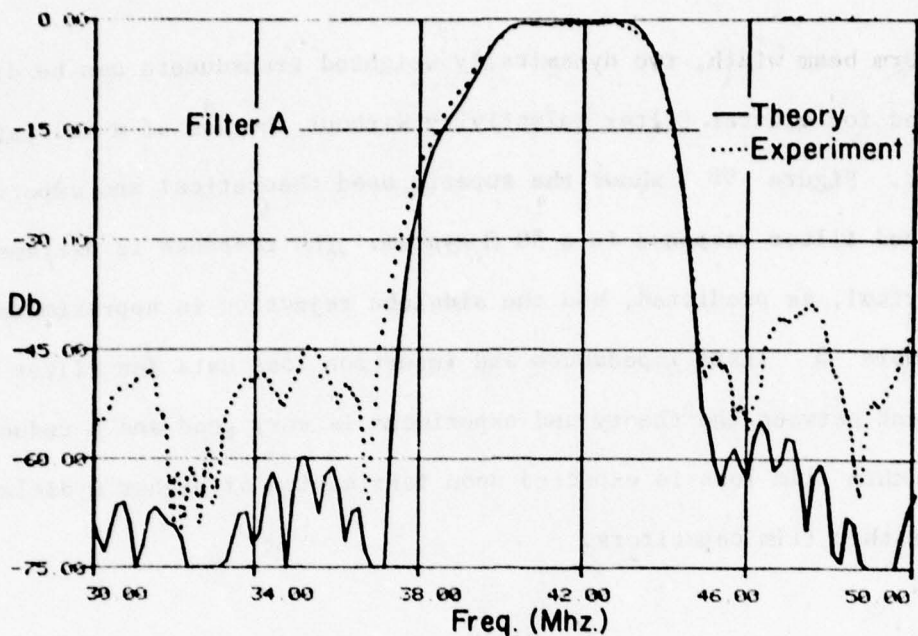
Filter A consists of a 10 pair, non-weighted interdigital transducer (IDT) in cascade with a CW transducer whose parameters are given in

TABLE 2  
PARAMETERS OF CW TRANSDUCER

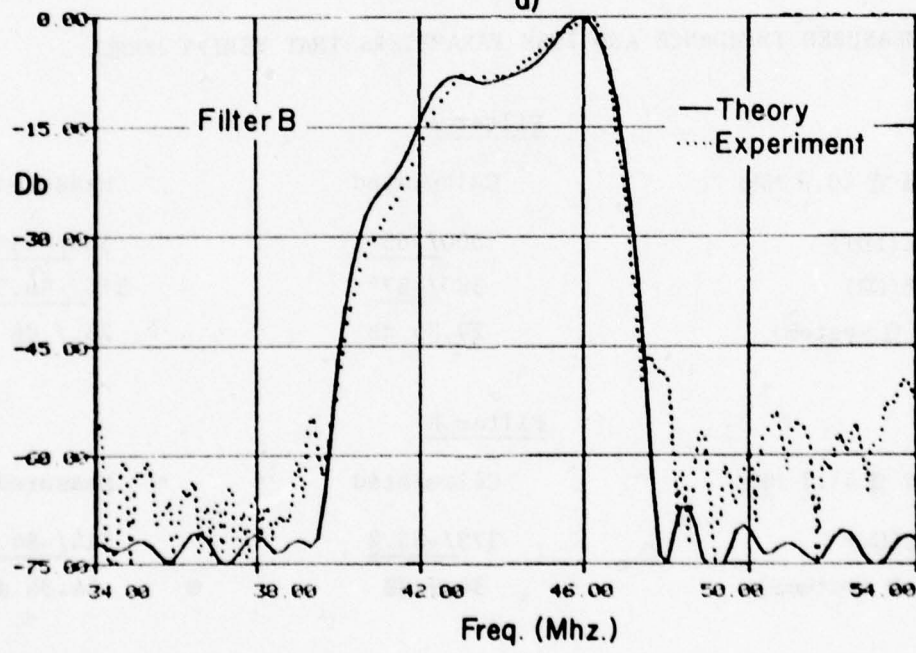
CW TRANSDUCER

wavelength	96 microns
beam width	10 wavelengths
transducer length	54 wavelengths
header capacitance	.81 pf
$\overline{N\alpha_w}$	10.95
$N_{eff}$	6.09
$S' = \overline{\alpha_w^2}/\alpha_w$	.57
RF sputtered dielectric, $t = 4400 \text{ \AA} \pm 5\%$	7059 Corning glass, $Q_{TF} = 20 \pm 10\%$

Table 2. Figure 9a shows the superimposed theoretical and experimental, unmatched filter response in a  $50 \Omega$  system. The passband response is good, however the sidelobe selectivity is limited to approximately -40 dB which is believed due to random fabrication errors and bulk or plate modes. Table 3 lists Filter A impedance and insertion loss data and agreement between theory and experiment is good.



a)



b)

Figure 9. Unmatched frequency responses of Filters A and B.

Filter B consists of two identically weighted CW transducers, whose parameters are given in Table 2. Because the CW transducers have

a uniform beam width, two dynamically weighted transducers can be directly cascaded for greater filter selectivity without the use of a multistrip coupler. Figure 9b shows the superimposed theoretical and experimental unmatched filter response in a  $50 \Omega$  system. The response is extremely non-symmetrical, as predicted, and the sidelobe rejection is approximately 50 dB. Table 3 lists impedances and insertion loss data for Filter B. Agreement between the theory and experiment is very good and a reduction in the thin film loss is expected upon fabrication of higher Q dielectrics for the thin film capacitors.

TABLE 3  
MEASURED IMPEDANCE AND LOSS PARAMETERS THAT VERIFY MODEL

<u>Filter A</u>		
Untuned @ 40.2 MHz	Calculated	Measured
Z(IDT)	$500/-65^\circ$	$535/-65^\circ$
Z(CW)	$380/-87^\circ$	$315/-86.5^\circ$
IL( $50 \Omega$ system)	29.85 dB	28.7 dB

<u>Filter B</u>		
Untuned @ 43.1 MHz	Calculated	Measured
Z(CW)	$373/-85.2$	$314/-84.5$
IL( $50 \Omega$ systems)	34.9 dB	34.36 dB

### G. Conclusion

The CW transducer has been presented as a practical way to achieve tap weight control for SAW filters. The impulse response model is derived, the thin film losses are defined and experimental verification is provided. The technique provides the uniform beam width advantages of the CTWN transducer but substantially reduces the transducer Q. The CW transducer Q is higher than a similar apodized transducer, however, the CW transducer provides more versatile design due to the uniform beam width and control of the effective capacitive coupling coefficient.

## SECTION III

### TAP WEIGHT ENHANCEMENT FOR BROADBAND FILTERS

#### A. Introduction

Considerable work has been devoted to the accurate design of SAW bandpass filters and to the techniques for adjusting the strength of the transducer taps used in these filters. Withdrawal weighting, first introduced by Hartmann [8] is becoming widely accepted as an effective means of controlling the response of narrowband transducers which contain a large number of taps. This approach produces a uniform width acoustic beam and allows two weighted transducers to be cascaded. In addition, a uniform beam is less sensitive to diffraction errors and field fringing at the end of the transducer electrodes, and therefore produces more predictable results. However, filters which require high selectivity, low shape factors, and large fractional bandwidths do not have a sufficient number of taps to make this technique effective. Such filters are generally realized using apodization or some form of attenuators attached to the taps to adjust the transducer response [9, 2]. Both of these techniques have a limited range over which

the tap weights can accurately be adjusted and designs with a large number of small taps are not as accurately implemented as designs with a smaller range of specified tap weights.

This chapter presents a compromise approach in which a series of taps with small strengths are replaced by a single larger tap. This tap enhancement technique is significantly different from the tap deletion described by Hartmann because it does not simply delete the taps to achieve tap weighting but deletes electrodes and alters the strength of the remaining electrodes to maintain the integrity of the design. This technique, called tap enhancement, improves the response of both the capacity weighted [2] and apodized transducers because larger taps are less sensitive to fabrication inaccuracies and field fringing which result in additive taps weight errors. In addition, this elimination of the large number of small taps lowers the electrical Q of capacity weighted transducer [2] and lowers the insertion loss of apodized transducers.

The analysis necessary for implementing the tap enhancement procedure is presented along with an experimental verification on a capacity weighted transducer. The effect of the tap enhancement on the inband ripple, the transition region, the near in selectivity, and the far field selectivity is demonstrated by the comparison of a reference filter which implements an entire set of tap weights and a second filter implementing a tap enhanced version of the original tap weights. Both devices use capacity weighted transducers.

## B. Tap Weight Enhancement Analysis

The tap enhanced design is achieved by substituting a single large tap for a number of smaller taps and adjusting the center frequency, amplitude, delay and phase of the larger tap to those values of the entire set being replaced.

Let  $W_1, W_2, \dots, W_N$  be the strength of a set of  $N$  small taps with delays  $t_1, t_2, \dots, t_N$ . This set of  $N$  taps is to be replaced with a single tap of strength  $W$  and delay  $T$ . Equating the amplitudes and phases at center frequency,  $f_o$ , yields:

$$We^{-j2\pi f_o T} = \sum_{i=1}^N W_i e^{-j2\pi f_o t_i} \quad (23)$$

Equating the group delays at center frequency yields

$$T We^{-j2\pi f_o T} = \sum_{i=1}^N t_i W_i e^{-j2\pi f_o t_i} \quad (24)$$

If the  $N$  taps are equally spaced, at half-wavelength intervals,

$$t_i = i\Delta t$$

where:

$$\Delta t = \frac{1}{2f_o}$$

and equations (23) and (24) are written as:

$$We^{-j\pi K} = \sum_{i=1}^N W_i e^{-j\pi i} \quad (25)$$

$$\sum_{i=1}^N n_i w_i e^{-j\pi i} = K w e^{-j\pi K} \quad (26)$$

where:

$$K = T/\Delta t$$

Since  $i$  is an integer, equation (25) requires  $K$  to be an integer.

Solving equation (25) and (26) for  $K$  yields:

$$K = \frac{\sum_{i=1}^N i w_i e^{-j\pi i}}{\sum_{i=1}^N w_i e^{-j\pi i}} \quad (27)$$

which, in general, is a non-integer value. To overcome this problem, a fraction of the  $N^{th}$  tap is left out of the replacement procedure in a manner so that equation (27) becomes an integer. Let  $m$  be the largest integer smaller than  $K$ . The portion of the  $N^{th}$  tap excluded from the summation is defined as  $\Delta w$  and is related to the integer  $m$  by

$$m = \frac{\sum_{i=1}^N i w_i e^{-j\pi i} - N \Delta w e^{-j\pi N}}{\sum_{i=1}^N w_i e^{-j\pi i} - \Delta w e^{-j\pi N}} \quad (28)$$

Substitution of equation (27) and (28) yields

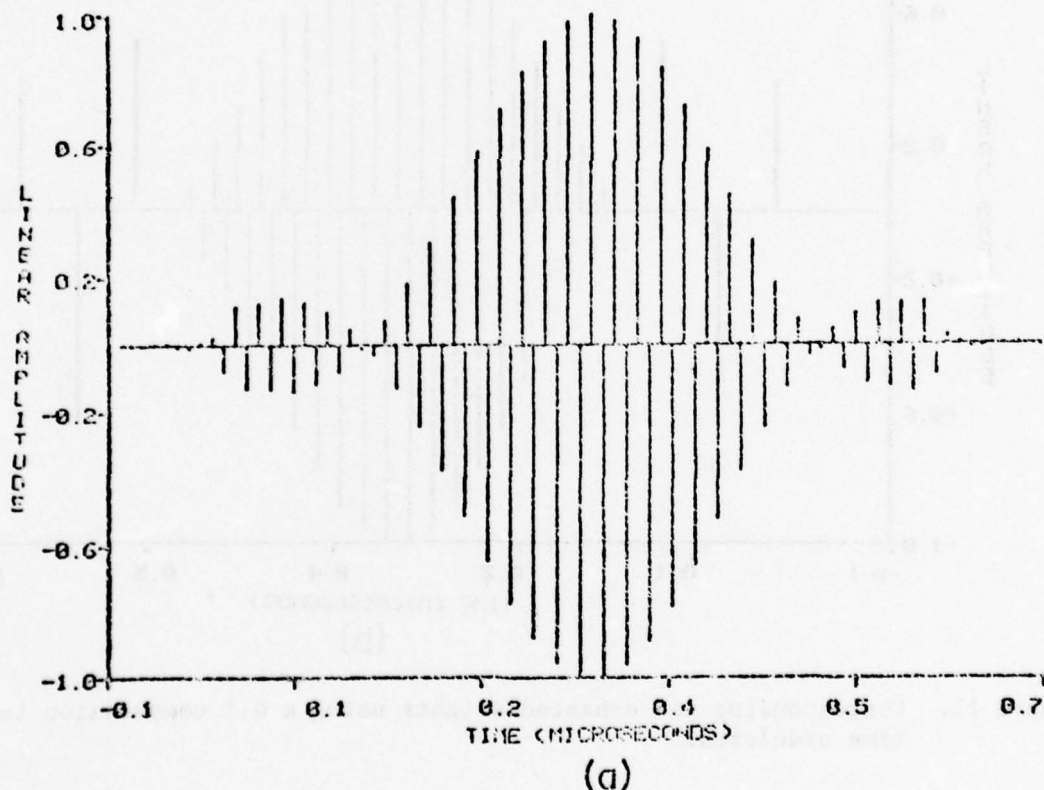
$$\Delta w e^{-j\pi N} = \frac{K-m}{N-m} \sum_{i=1}^N w_i e^{-j\pi i} \quad (29)$$

This artifice enables the replacement of the  $N$  taps of strengths  $w_1, w_2, \dots, w_{N-1}, (w_N - \Delta w)$  with a single tap of strength  $w$ :

$$W = \left( \sum_{i=1}^N W_i \right) - \Delta W \quad (30)$$

such that equation (25) and (26) are both satisfied. The portion of the  $N^{th}$  tap excluded from the summation,  $\Delta W$ , is considered as part of the next set of taps to be replaced and the same procedure is repeated.

Figure 10 shows the set of equally spaced reference tap weights used as an example in comparison to an enhanced set of tap weights where a



(a)

Figure 10. Conventional set of periodically spaced tap weights.

4:1 compression is used in each time sidelobe (Figure 11). Applying the compression to only the sidelobes reduces the nearest neighbor effect errors. Figure 12 is the frequency response of the reference tap weights and

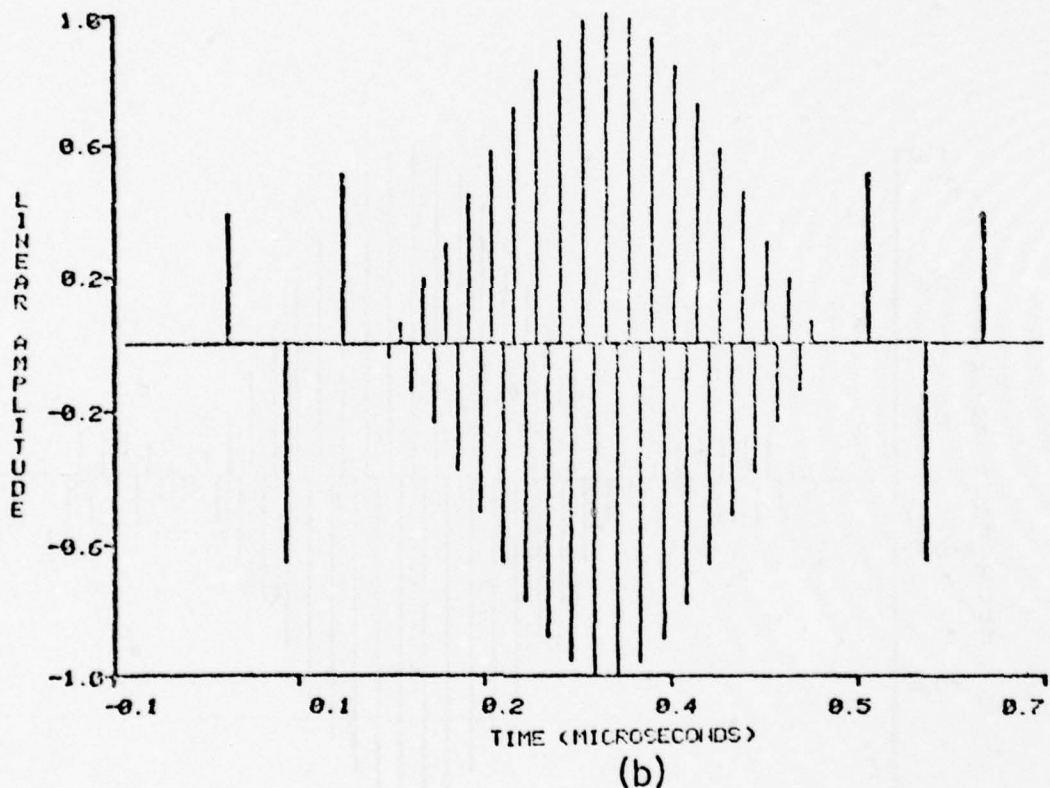


Figure 11. Corresponding tap enhanced weights using a 4:1 compression in the time sidelobes.

Figure 13 is the response of the compressed set of tap weights. The tap enhancement of this example introduces a passband ripple,\* but causes no loss in sidelobe selectivity within 15% of the center frequency. The loss in selectivity far from center frequency is exchanged for a reduction of the total number of taps and an increase in the average magnitude of the tap weights. Since impedance matching of the device to the load is commonly implemented to reduce the filter insertion loss, the loss in far band selectivity is normally regained.

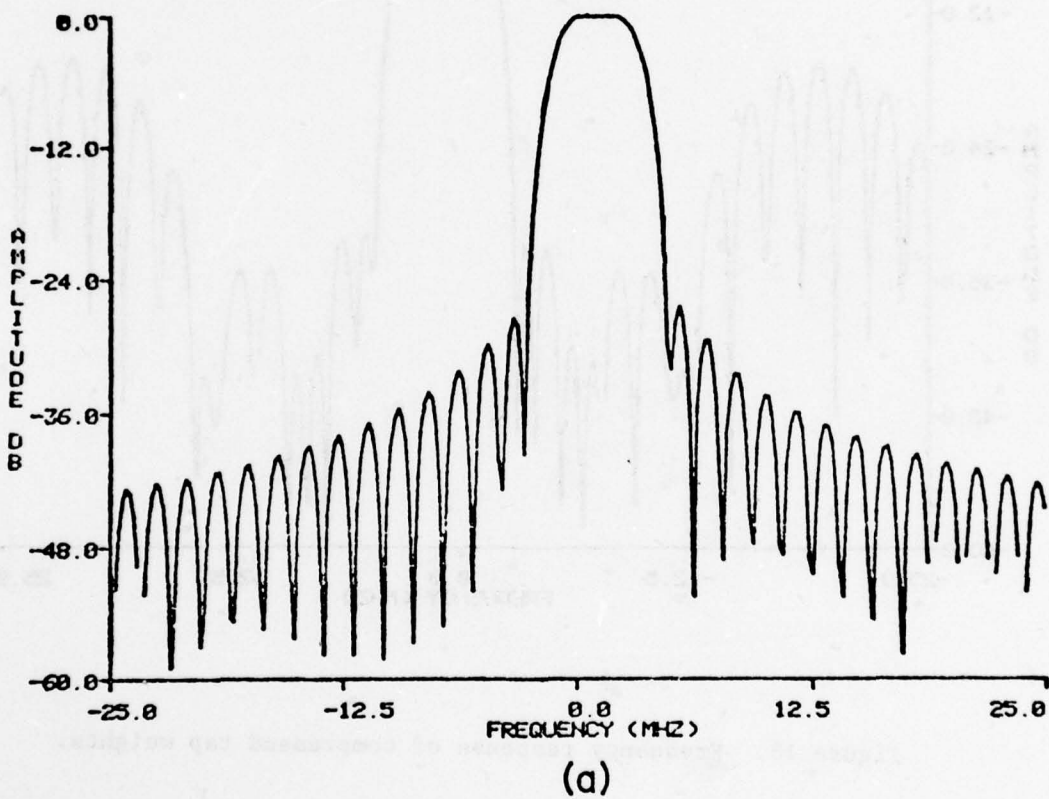


Figure 12. Frequency response of reference tap weights.

---

\*This ripple is not removed because it compensates for matching network rolloff.

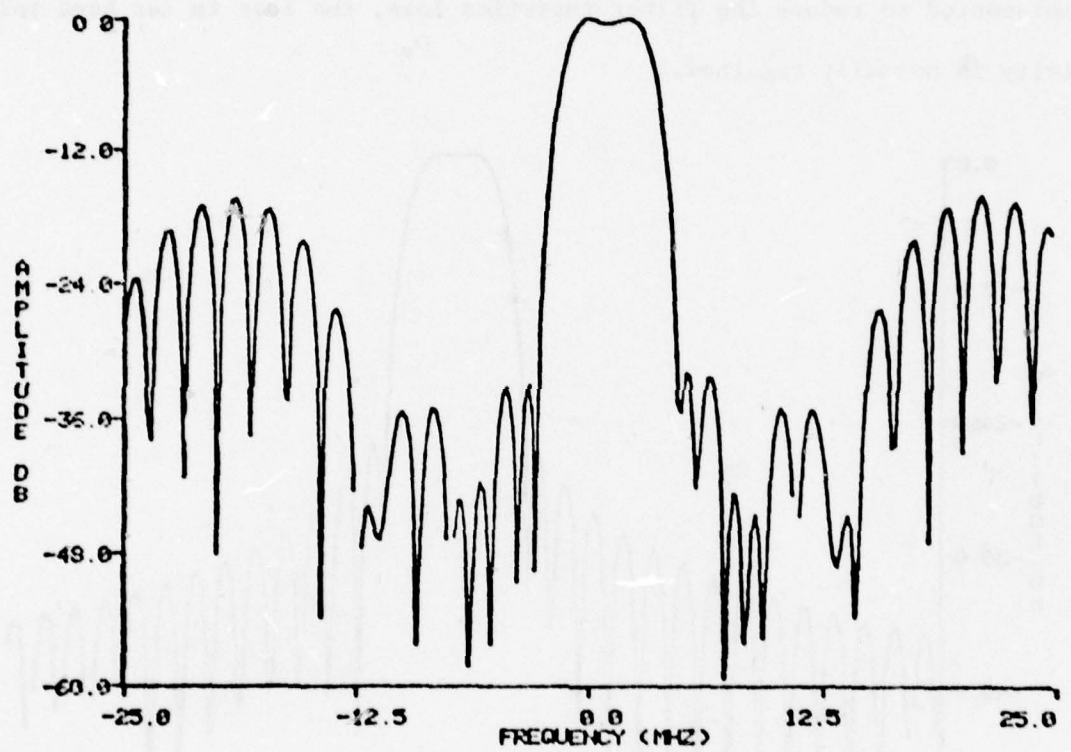


Figure 13. Frequency response of compressed tap weights.

### C. Experiment

Two filters have been fabricated to verify the tap enhancement techniques. Filter A used two cascaded capacity weighted transducers to

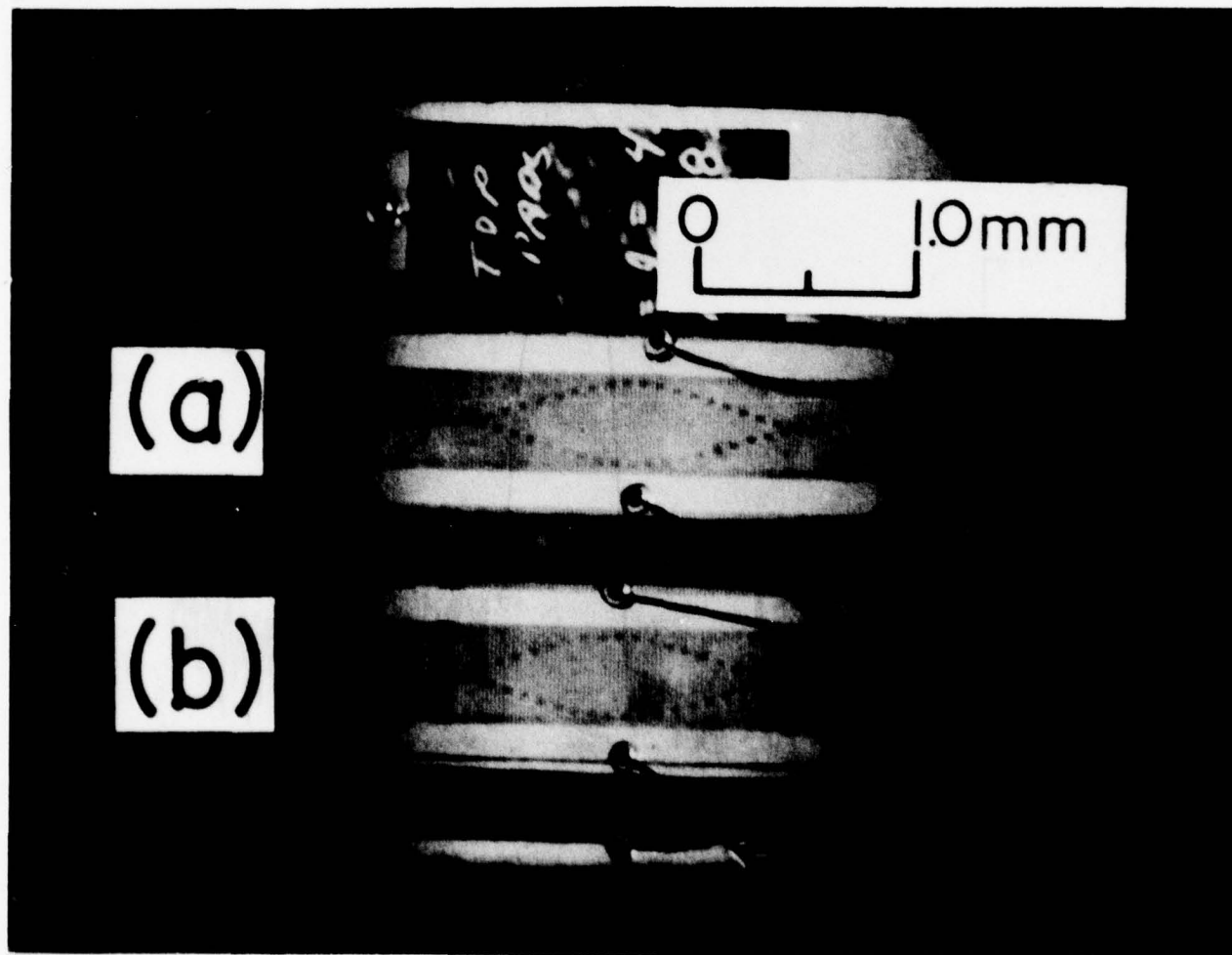


Figure 14. Photograph of actual device.

- a) Filter A using conventional tap weighting.
- b) Filter B using tap enhancement.

implement the reference tap weights and Filter B used the same type transducers to implement the enhanced tap weights as shown in Figure 14. The devices have a center frequency of 50.6 MHz and a 5 wavelength beam width. The dielectric layer is evaporated  $\text{SiO}_x$  having a thickness of 3400 Å and the upper and lower electrodes are of Al having a thickness of approximately

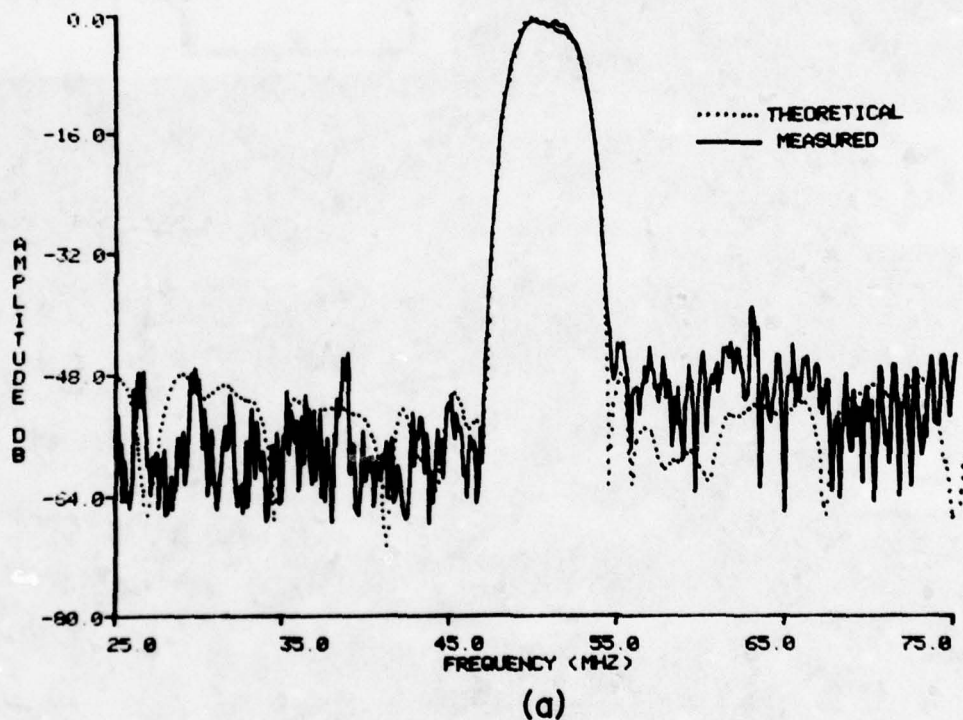
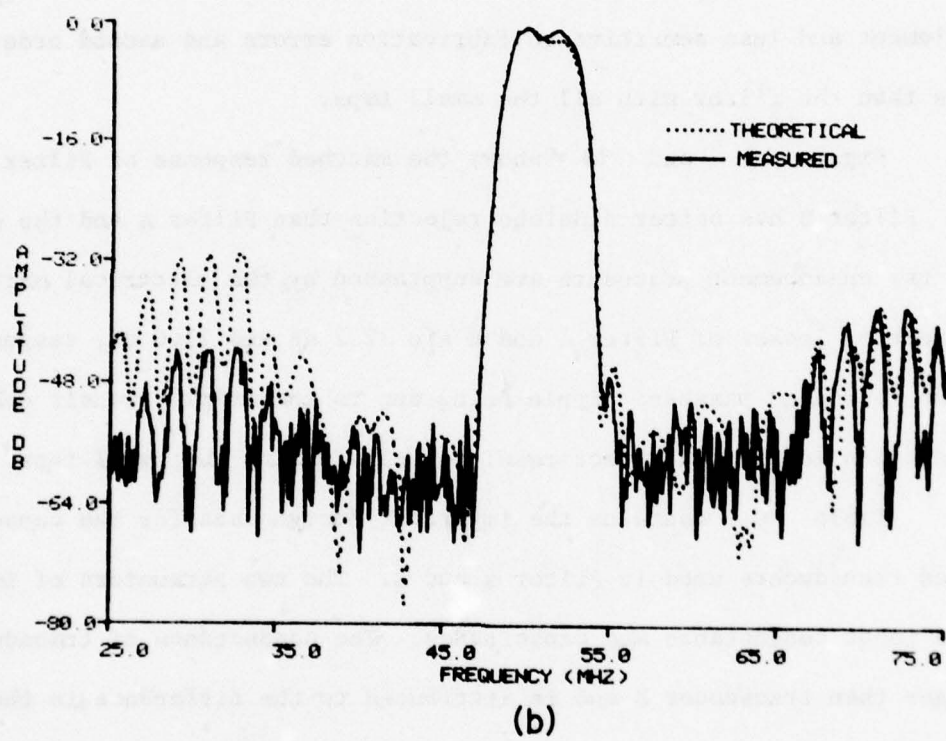


Figure 15. Superimposed unmatched theoretical and measured frequency response for Filter A.



**Figure 16.** Superimposed unmatched theoretical and measured frequency response for Filter B.

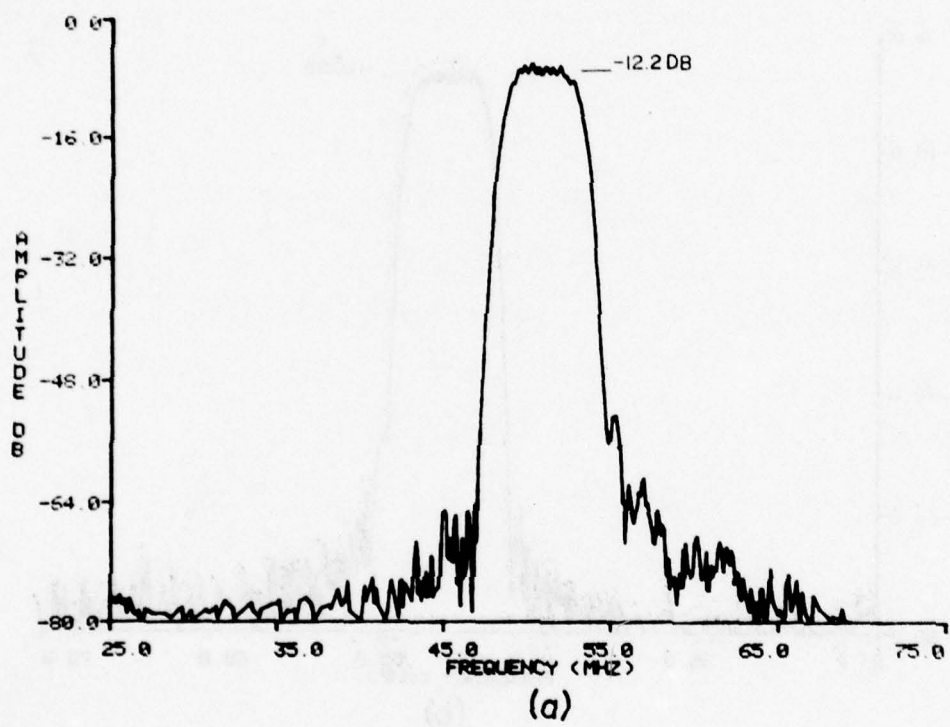
2000 Å. Figure 15 is the superimposed unmatched theoretical<sup>†</sup> and measured frequency responses of Filter A which are in good agreement in the passband with a slightly higher sidelobe level than predicted. Figure 16 is the superimposed unmatched theoretical<sup>†</sup> and measured frequency responses of Filter B which are also in good agreement with slightly less roundoff in the passband than predicted. The passband shape of Filter B is predicted well and the near passband sidelobes are maintained at about -50 dB. The loss of selectivity far from center frequency is predicted. Comparison of Figure 15 and 16 demonstrates that the tap enhanced design is easier to implement and less sensitive to fabrication errors and second order effects than the filter with all the small taps.

Figure 17 and 18 shows the matched response of Filter A and B. Filter B has better sidelobe rejection than Filter A and the effects of the tap enhancement procedure are suppressed by the electrical matching. The insertion losses of Filter A and B are 12.2 dB and 11.0 dB, respectively, with the increased passband ripple being due to the triple transit echo. The reduction in IL is a direct result of eliminating the small taps.

Table 4 contains the important design data for the capacity weighted transducers used in Filter A and B. The two parameters of importance are the input conductance and capacitance. The conductance of transducer A is larger than transducer B and is attributed to the difference in the capacitor losses of the thin film networks, based on insertion loss measurements. The input capacitance of the tap enhanced transducer, B, is approximately 15% less than the reference transducer, A, and is close to the predicted value of 16.7%. This verifies the increase in the transducer insertion-bandwidth product resulting from the elimination of the small taps.

---

<sup>†</sup>The theoretical response reflects the actual tap positions as measured with a surface profiler.



(a)

Figure 17. Matched frequency response for Filter A.

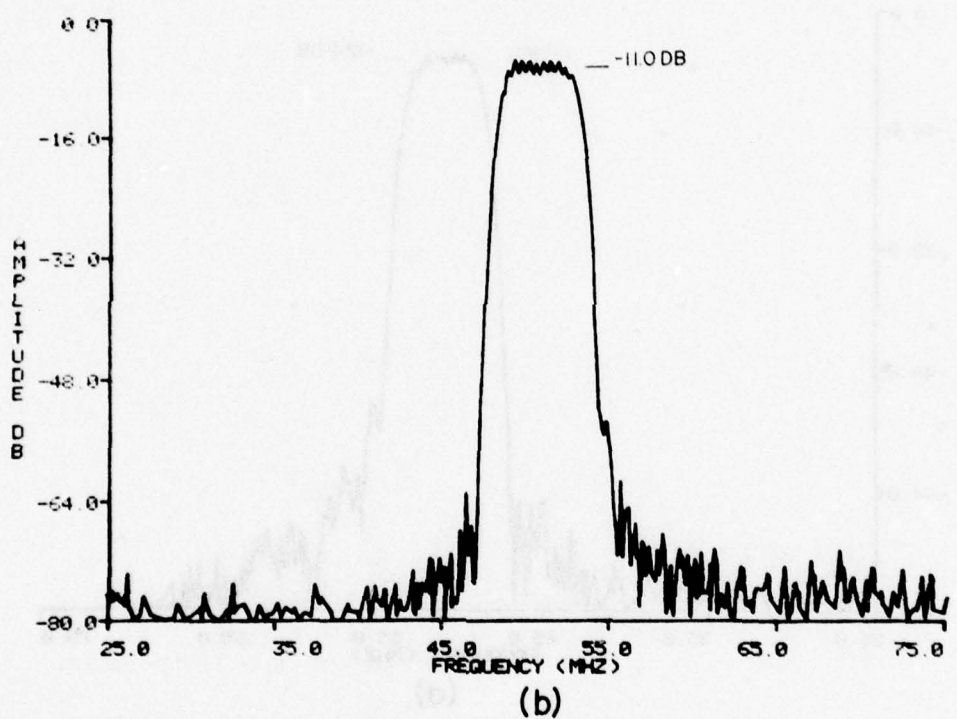


Figure 18. Matched frequency response for Filter B.

TABLE 4  
PARAMETERS FOR TEST TRANSDUCERS

Design Parameters	Transducer A	Transducer B
$f_o$ (MHz)	51.0	51.0
Beam Width ( $\lambda$ 's)	5.0	5.0
$\overline{\alpha_w^2}$	0.22	0.35
$C_s$ (pf)	0.251	0.251
$C_T$ (pf)	0.848	0.848
$\alpha_R$	0.296	0.296
$G_{IN}$	268.37	240.21
$C_{IN}$ (pf)	13.2	11.4

- 
- $\overline{\alpha_w^2}$  - mean squared tap weight  
 $C_s$  - capacitance of lower electrodes for a single tap  
 $C_T$  - capacitance of thin film bridge network for a single tap  
 $\alpha_R$  - ratio of  $C_s$  to  $C_T$

#### D. Conclusion

The theory for the substitution of a single large tap for a series of small taps has been derived. Experimental results for capacity weighted transducers verify the theory. The elimination of small taps increases the transducer insertion loss-bandwidth product and results in better filter selectivity when impedance matching is implemented. This technique works for the general class of bandpass filters, including broadband filters, with low shape factors where withdrawal weighting is not effective. Tap enhancement may also be extended to the apodized transducer for increased tap weight accuracy and reduced diffraction distortions.

### SECTION IV

#### GROUP TYPE CAPACITIVELY WEIGHTED UNIDIRECTIONAL TRANSDUCERS FOR HIGHLY SELECTIVE FILTERS

##### A. Introduction

Surface acoustic wave (SAW) unidirectional transducers (UDT) achieve low loss by eliminating bidirectional generation. The UDT also has the further advantage of greatly suppressing the triple transit (TT) echo associated with bidirectional transducers [10].

It is the purpose of this chapter to describe the group type capacitively weighted unidirectional transducer (CW-UDT). This technique yields the desired unidirectional power flow and triple transit suppression while providing tap weighting of a uniform beam. The CW-UDT enables the design of low shape factor, highly selective, broadband filters where the use of withdrawal weighting is impractical. The theory of capacitive tap weighting [11] and group type unidirectional transducers [12] have been previously described; this chapter discusses the merging of the two concepts and the resulting CW-UDT structure. A filter consisting of two identical CW-UDT's directly in cascade is presented and the filter results are discussed.

### B. Group Type CW-UDT Structure

The group type UDT structure consists of two identical, interleaved ports, labeled I and Q, with quarter wavelength spatial shift between I and Q ports at center frequency. Figure 19 shows the metalization pattern of a non-weighted, group type UDT. When an electrical 90° phase

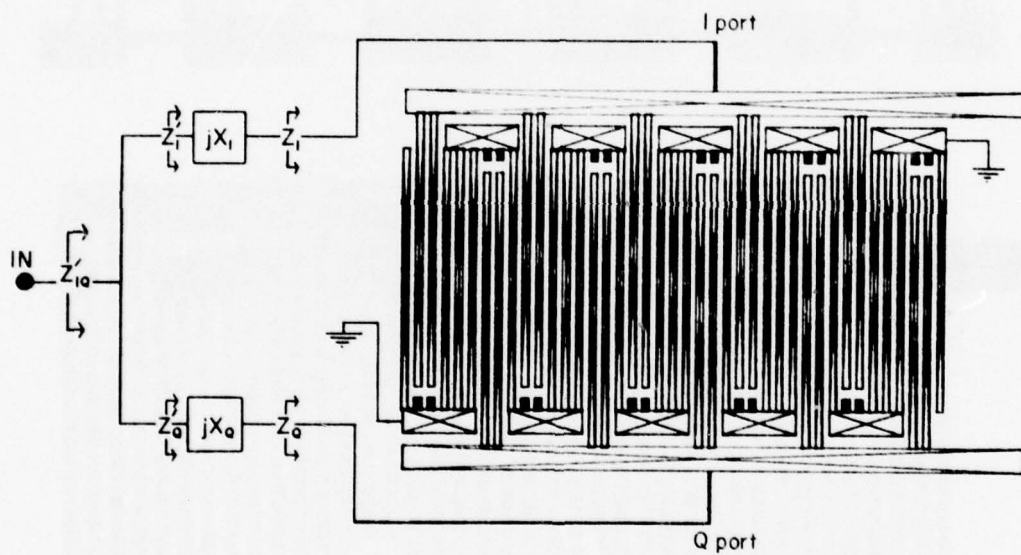
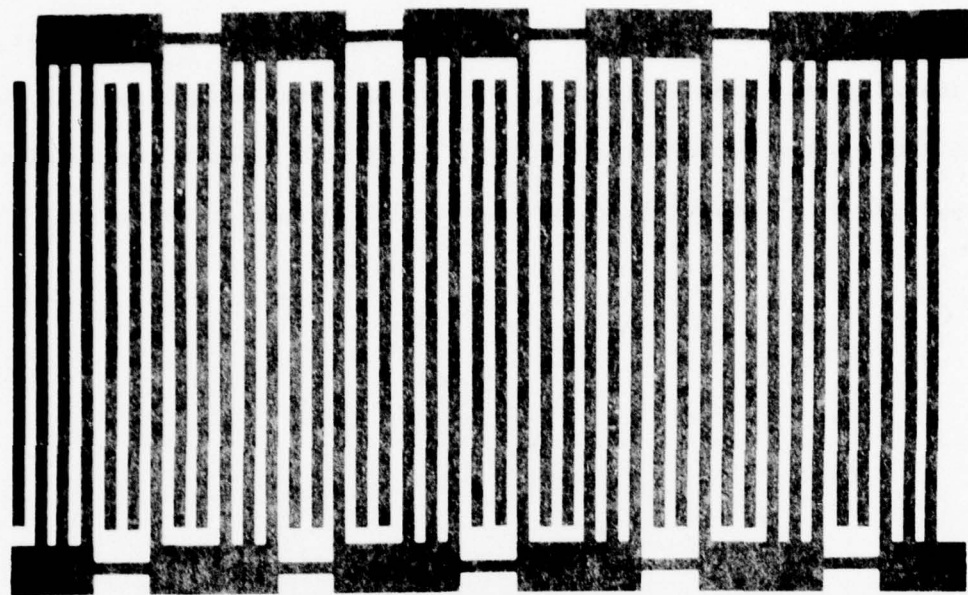


Figure 19. Group type unidirectional transducer.

shift is provided between I and Q ports at center frequency the surface waves add constructively in the forward direction and destructively in the reverse direction providing unidirectional power flow. The structure

(a)



(b)

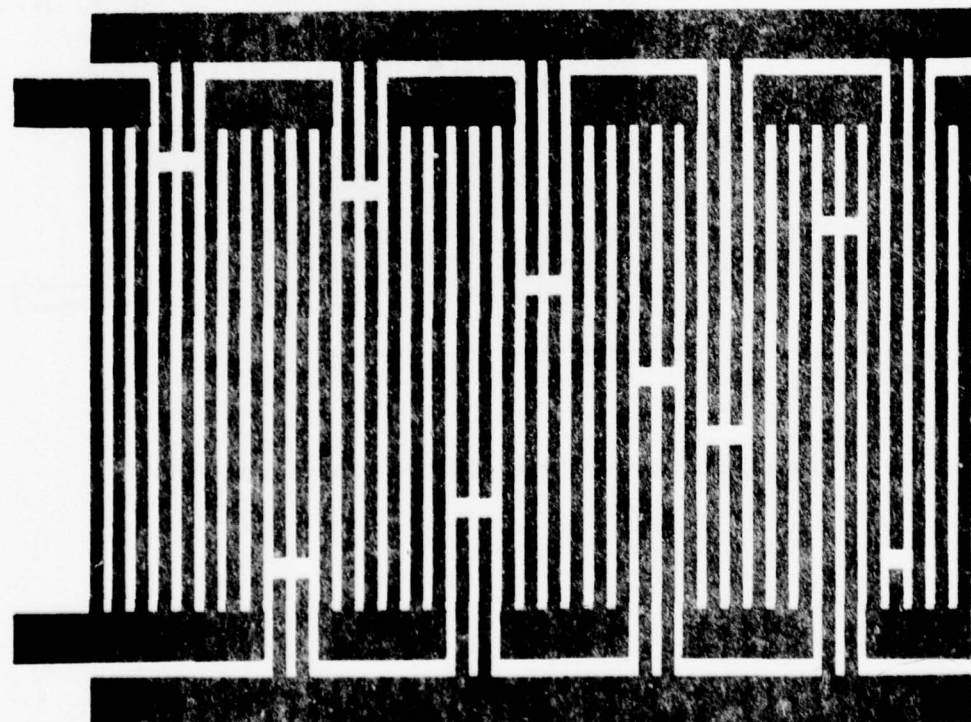


Figure 20. CW-UDT metalization pattern

- a) lower
- b) upper

requires no crossovers and is processed in a single fabrication step, however, there are two important limitations. First, the meandering ground line provides a high resistance path whose magnitude depends on transducer length. This results in resistive loss. The second problem is that breaks or thin spots in the ground line due to fabrication errors may render large portions of the transducer electrodes inoperative, thereby reducing manufacturing yields.

The group type CW-UDT transducer structure is composed of a set of lower electrodes and ground buses deposited directly atop the piezoelectric substrate, a sputtered dielectric layer deposited over the entire substrate, and a set of upper electrodes and buses which are correctly aligned with respect to the lower electrodes. Figure 20a shows a lower electrode pattern for a CW-UDT. The ground buses are connected together on either side of the acoustic beam by a quarter wavelength metal strip to reduce the meandering ground line resistance. Floating electrode pairs are used for the thin film weighting capacitors and are alternately coupled to the I and Q ports. Figure 20b shows the upper electrodes of the coupling capacitors and bonding pads. A perspective of the repetitive structural unit of the CW-UDT is shown in Figure 21. The electrodes connected to the I and Q ports crossing over the lower ground strip are isolated by the dielectric layer. This increases transducer capacitance but decreases device insertion loss. The increase in transducer capacitance is determined by the number of crossovers and the capacitance per crossover. Bonding of the device is accomplished on the upper aluminum pattern, with the capacitive reactance between the upper and lower ground electrodes and pads forming a virtual short.

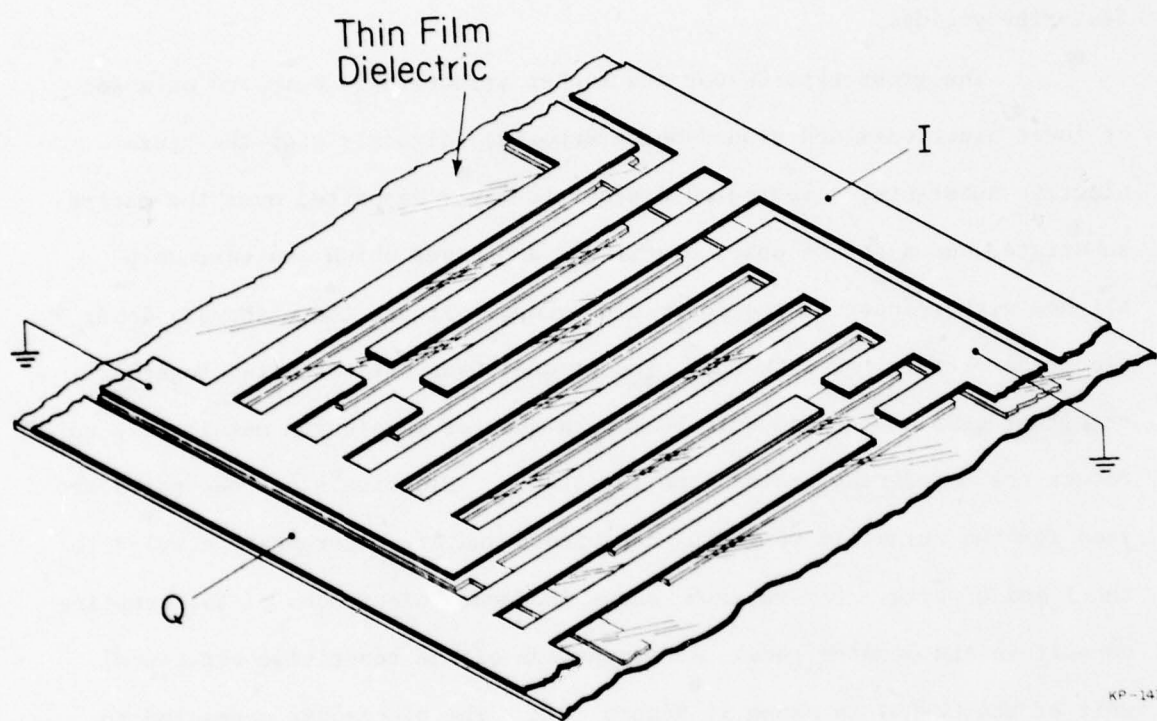


Figure 21. CW-UDT perspective.

### C. Filter Design and Results

The filter response consists of two identically weighted CW-UDT's having 10 wavelength beam widths at a center frequency of 41 MHz. Each transducer has a 10 percent bandwidth and a shapefactor of 3. The important transducer design data is listed in Table 5. Corning 7059 glass is RF sputtered to a thickness of  $3600 \text{ \AA}$  and used as the thin film capacitor dielectric. The sputtering is accomplished in a 1:1 atmosphere of argon and oxygen having a background pressure of  $20 \mu$  and a deposition rate of approximately  $25 \text{ \AA/min.}$  The system provides uniform, pin hole free films.

The transducers are tuned using a two element series tuning scheme (Section V) which yields a pure, real input impedance and provides the required  $90^\circ$  phase shift between ports. The input impedance, with the tuning network in place, is  $65 \Omega$  which is a reasonably close match for testing in a  $50 \Omega$  system. Figure 22a shows the magnitude of the passband ripple being approximately 0.05 dB. The triple transit echo (measured at -47 dB) is accounted for by edge and absorber reflections having approximately the same magnitude. The 6 dB insertion loss passband and adjacent sidelobes (down 60 dB) are shown in Figure 22b. Figure 22c is the broadband filter response. Subharmonics inherent in the transducer design appear as expected. This is a predictable affect which must be considered in the design of a CW-UDT.

Each transducer has approximately 3 dB loss which is primarily due to the thin films composing the transducer structure. The two major mechanisms are the resistive losses of the conductors and the thin film dielectric loss. The dielectric Q is 20 which yields a dielectric loss of approximately 1 dB per transducer. The remaining loss is primarily due to the conductor resistance of the electrodes and pads.

TABLE 5

## CW UDT DATA

center frequency	41 MHz
3 dB bandwidth	4.1 MHz
transducer length	19 wavelengths
acoustic beam width	10 wavelengths
bus bar width	1 wavelength
dielectric	7059 glass - RF sputtered 3600 Å $\pm$ 10%
conductor	aluminum 2000 Å $\pm$ 20%

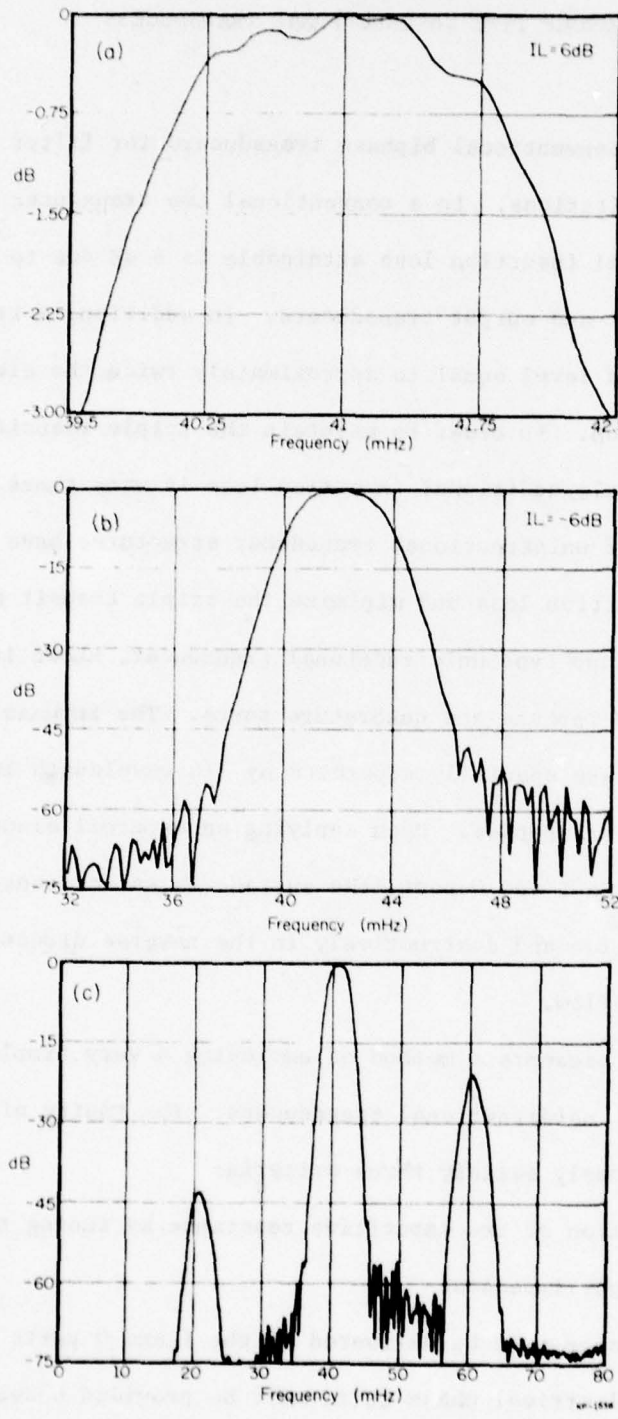


Figure 22. CW-UDT response.

## SECTION V

### TUNING OF GROUP TYPE UNIDIRECTIONAL TRANSDUCERS

#### A. Introduction

The use of conventional biphasic transducers for filter applications have two inherent limitations. In a conventional two transducer configuration, the minimum theoretical insertion loss attainable is 6 dB due to the bidirectionality of the input and output transducers. In addition, a triple transit echo is present with a level equal to approximately twice the electrical mismatch loss plus 6 dB. In order to maintain the triple transit signal below a specified level, additional insertion loss is many times introduced.

A variety of unidirectional transducer structures have been reported to reduce filter insertion loss and minimize the triple transit echo [12].

[13], [3]. The group type unidirectional transducer, shown in Figure 23, uses interleaved inphase and quadrature ports. The inphase (I) and quadrature (Q) ports are spatially separated by 1/4 wavelength and each have identical filter responses. Upon applying an external electrical phase shift between the I and Q port, the surface waves add constructively in the forward direction and destructively in the reverse direction providing unidirectional power flow.

This paper presents a method of employing a very simple tuning scheme for group type unidirectional transducers. The tuning of the transducer must simultaneously satisfy three criteria:

- 1) elimination of the capacitive reactance by tuning to a purely real input impedance
- 2) equal power must be delivered to the I and Q ports
- 3) a 90° electrical phase shift must be provided between the I and Q ports.

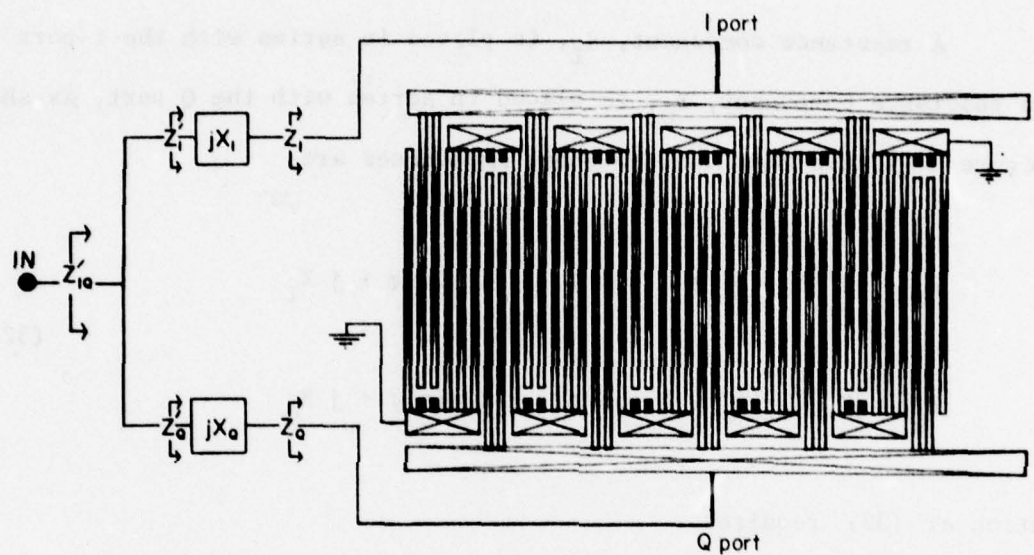


**Figure 23.** Series tuning approach for block type UDT. The tuning elements are represented by the reactances  $jX_I$  and  $jX_Q$  for the I and Q ports, respectively.

The method of tuning presented uses a maximum of two elements and, in particular cases which are described, the use of a single tapped coil or a single inductor will provide the necessary tuning network while satisfying the three conditions listed above.

## B. Network Analysis

For symmetrical filters, the impedance of the I and Q ports is identical and given by

$$z_I = z_Q = |A| \angle -\phi \quad (31)$$

A reactance component,  $X_I$ , is placed in series with the I port and a reactance component,  $X_Q$ , is placed in series with the Q port, as shown in Figure 23, such that the new input impedances are

$$z'_I = |A'| \angle +45^\circ = A \cos \phi - j A \sin \phi + j X_I \quad (32)$$

$$z'_Q = |z'| \angle -45^\circ = A \cos \phi - j Z \sin \phi + j X_Q$$

Solution of (32) requires

$$X_I = A(\cos \phi + \sin \phi) \quad (33)$$

$$X_Q = A(\sin \phi - \cos \phi)$$

and substitution of (33) into (32) yields

$$|A'| = |\sqrt{2} A \cos \phi| \quad (34)$$

The sum of the reactances  $X_I$  and  $X_Q$  is

$$X_I + X_Q = 2A \sin \phi \quad (35)$$

which is equal to the sum of the capacitive reactances of both the I and Q ports. The generator sees the impedances  $Z'_I$  and  $Z'_Q$  in parallel yielding

$$Z'_{IQ} = \frac{Z'_I Z'_Q}{Z'_I + Z'_Q} = |A \cos \phi| \angle 0^\circ \quad (36)$$

which is a purely real impedance.

It is also possible to obtain the same results using a parallel tuning configuration shown in Figure 24. Following a similar procedure

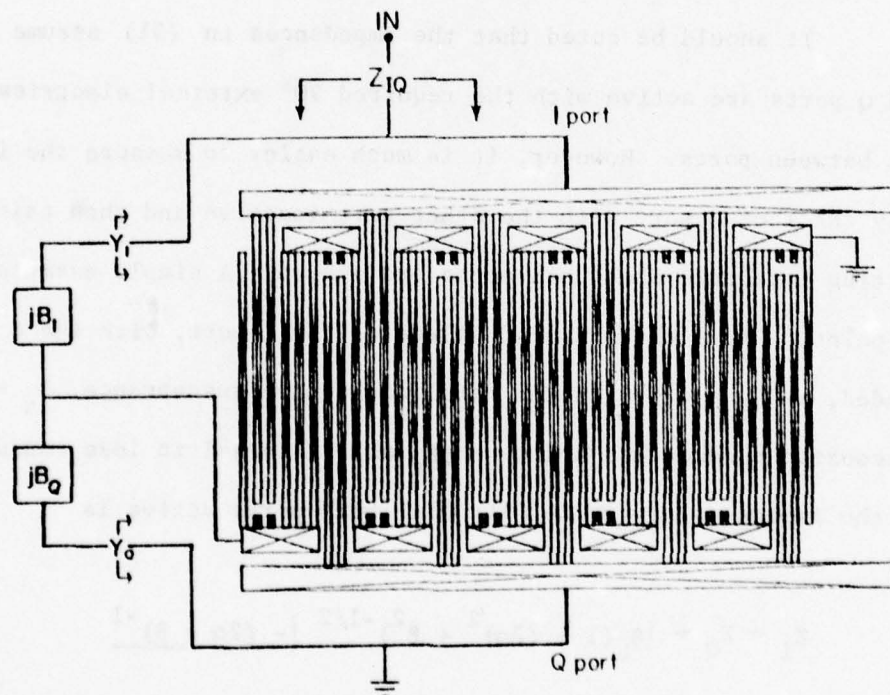


Figure 24. Parallel tuning approach for block type UDT. The tuning elements are represented by the susceptances  $jB_I$  and  $jB_Q$  for the I and Q ports, respectively.

as previously described, it is straightforward to show that the input impedance seen by a generator for parallel tuning is

$$Z'_{IQ} = \left| \frac{A}{2 \cos \phi} \right| \angle 0^\circ \quad (37)$$

For either tuning configuration, the same voltage is applied to the I and Q ports and the magnitude of the impedances are identical, therefore the power delivered to each port is the same. The necessary  $90^\circ$  phase shift between the current in the I and Q ports is provided by the reactive components thereby satisfying the requirements for unidirectional power flow when driving the two ports in parallel with a given generator.

It should be noted that the impedances in (31) assume both the I and Q ports are active with the required  $90^\circ$  external electrical phase shift between ports. However, it is much easier to measure the impedance of only the I or Q port with the other port inactive and then calculate the resulting impedance when both ports are active. A simple example clarifies this point. Given the measured values of the I port, with the Q port grounded, as  $B_C = \omega_0 C_{IN}$  as the total capacitive susceptance,  $G_a = \alpha B_C$  as the acoustic conductance and  $G_p = \beta B_C$  as the parasitic loss conductance, then the impedance given in (31) with both ports active is

$$Z_I = Z_Q = \left| B_C (1 + (2\alpha)^2 + \beta^2)^{-1/2} \right| \angle - (2\alpha + \beta)^{-1} \quad (38)$$

The results in (40) simply state the capacitive susceptance and parasitic conductances add while the acoustic conductance doubles at each port due to the acoustic and electrical interactions of the I and Q ports. It is extremely important to include this interaction when calculating the input impedance  $Z'_{IQ}$ .

The transducer input impedance is dependent upon the percent bandwidth, shape factor, beam width, particular device structure and parasitic conductance and capacitance. The following example assumes no parasitics but these can be easily included when they are determined. It is instructive to examine the simple case of a non-weighted UDT at center frequency since this provides a concise and simple analysis.

For a non-weighted transducer at center frequency the input conductance is

$$G_a = 8k^2 f_o C_s N^2$$

where  $k^2$  is the piezoelectric coupling coefficient,  $f_o$  is the center frequency,  $N$  is the number of finger pair and  $C_s$  the finger pair capacitance which is a function of the substrate material and transducer beam width. With both the I and Q ports active, the impedance in (31) is

$$A = 2[Nf_o C_s \sqrt{(2\pi)^2 + (8k^2 N)^2}]^{-1} \quad (39)$$

$$\phi = \tan^{-1} \left[ \frac{2\pi f_o N C_s}{8k^2 f_o C_s N^2} \right] = \tan^{-1} \left[ \frac{\pi}{4k^2 N} \right]$$

where the factor of 2 preceding the bracketed term in the magnitude arises from splitting the transducer into I and Q ports. Letting  $x = \frac{4k^2}{\pi} N$ , (37) is rewritten as

$$A = 2[N\omega_o C_s \sqrt{1 + x^2}]^{-1} \quad (40)$$

$$\phi = \tan^{-1}[x^{-1}]$$

Three cases quickly lend insight into series tuning the unidirectional transducer and similar cases can be obtained for parallel tuning.

Case 1. For  $x \ll 1$ , then  $\phi \ll 45^\circ$ ,  $A \approx 2/N\omega_0 C_s$  and the tuning elements are  $X_I = \omega_0 L_I$  and  $X_Q = \omega_0 L_Q$ .

This corresponds to large percent bandwidth filters with few fingers which require inductors for both tuning elements. Tuning can be achieved by using two separate inductors or using a single tapped coil where the ratio of the inductances obtained from (33) are

$$\frac{L_Q}{L_I} = \frac{\sin \phi - \cos \phi}{\sin \phi + \cos \phi} \quad (41)$$

As the phase approaches  $90^\circ$ , the two inductors are nearly of equal size which allows nearly center tapping of a single coil and as the phase approaches  $45^\circ$  the inductor  $L_Q$  approaches 0.

Case 2. For  $x = 1$ , then  $\phi = 45^\circ$ ,  $A = \frac{\sqrt{2}}{N\omega_0 C_s}$  and the tuning elements are  $X_I = \omega_0 L_I$  and  $X_Q = 0$ . This is a unique condition where  $N = \pi/4k^2$  and only a single element is needed where  $\omega_0 L_T = \sqrt{2} A$ .

Case 3. For  $x \gg 1$ , then  $\phi \gg 45^\circ$ ,  $A \approx \frac{2}{xN\omega_0 C_s}$  and the tuning elements are  $X_I = \omega_0 L_I$  and  $X_Q = (\omega_0 C_Q)^{-1}$ . This corresponds to narrow band filters with many fingers. The capacitor,  $C_Q$ , can be either external or a thin film capacitor utilizing unused substrate area outside the propagation path. If the capacitor is fabricated on the substrate, only a single external tuning coil is needed to satisfy all the criteria.

### C. Experimental Results

To experimentally verify the above analysis, a filter was fabricated using an interdigital unidirectional transducer (ID-UDT) in cascade with a capacitively weighted unidirectional transducer (CW-UDT) each having 10 wavelength beam width. Capacitive weighting of one transducer was used since it provides dynamic tap weighting for filter selectivity while maintaining a uniform beam width [3], [14]. The device is designed, bonded and packaged symmetrically about the center of the beam to obtain nearly identical parasitic effects on the I and Q ports of each transducer. Testing of the filter was accomplished in a  $50 \Omega$  system. Both transducers used the series tuning approach since the impedances obtained were very close to  $50 \Omega$  and identical results were obtained using either two inductors or a single tapped coil. The transducers were tuned to simultaneously obtain the highest signal level with minimum passband ripple and measurement of the input impedances always yielded a purely real value as predicted. The calculated impedance  $Z'_{IQ}$  for the ID-UDT is  $41 \Omega$  and the measured value is  $43 \Omega$  and the calculated impedance  $Z'_{IQ}$  for the CW-UDT is  $48 \Omega$  and the measured value is  $58 \Omega$ . The difference in the calculated and measured impedance of the CW-UDT is due to the estimation of the thin film loss conductance based on insertion loss measurements.

The filter response, shown in Figure 25 has 6.3 dB insertion loss, the bulk of which is due to thin film losses, 45 dB sidelobe selectivity and approximately .1 dB passband ripple. This corresponds to a triple transit echo suppression of approximately -44 dB as verified in the impulse response of Figure 26.

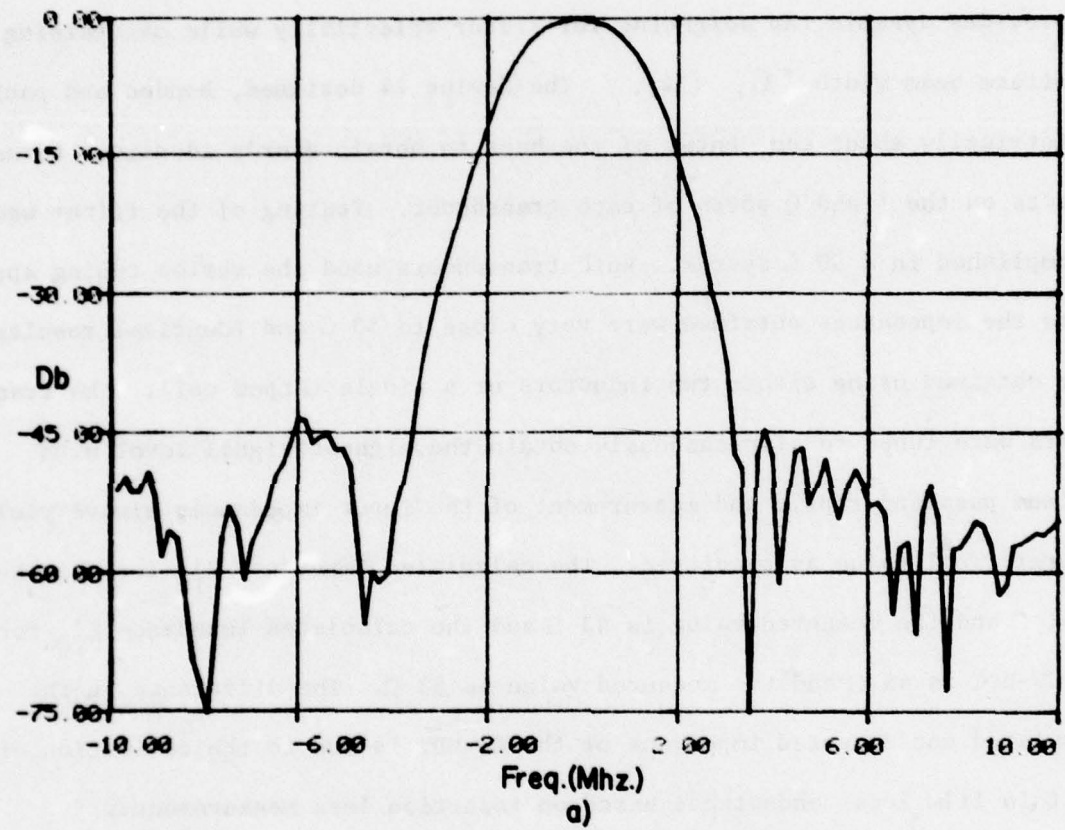


Figure 25. Filter frequency response measured relative to a 41 MHz center frequency and 6.3 dB insertion loss.

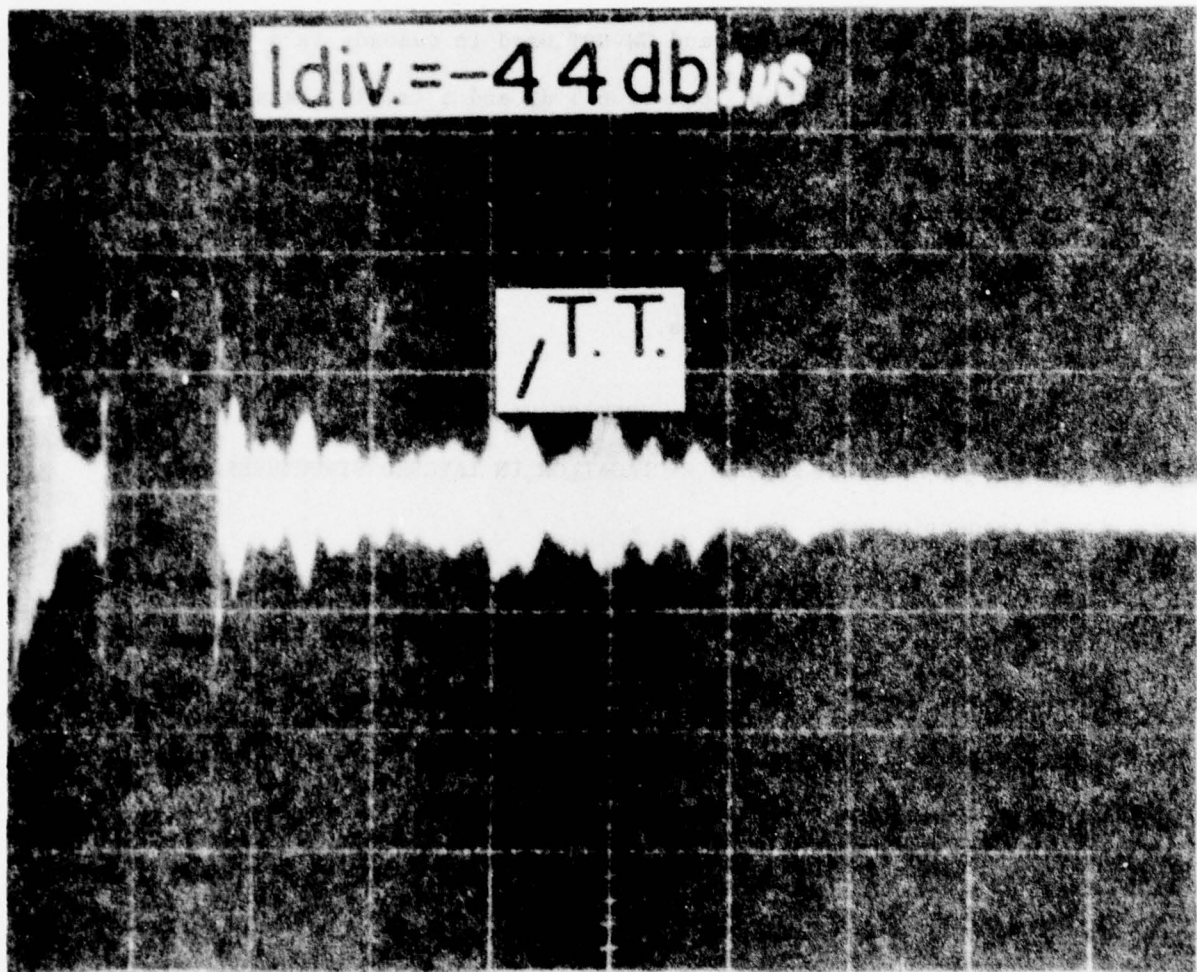


Figure 26. Impulse response of filter with the triple transit 44 dB below the main signal.

#### D. Conclusions

The theory for a simple tuning network for group type unidirectional transducers which provide a 90° electrical phase shift between inphase and quadrature ports, equal power to both ports and yields a purely real input impedance to a load has been derived. The tuning network has been verified for an ID UDT and CW UDT used in cascade in a single filter which yielded an insertion loss of 6.3 dB and a triple transit echo suppression of -44 dB. This simple tuning scheme will make group type unidirectional transducers very attractive for filter applications requiring low loss and greatly reduced triple transit echos which are unachievable using bidirectional transducers.

## SECTION VI

### ANALYSIS OF SAW PROPAGATION IN LAYERED STRUCTURES

#### A. Introduction

Surface wave solutions in piezoelectric crystals are usually obtained using an iterative search procedure for the velocity such that the electrical and mechanical boundary conditions are satisfied [15]. This procedure is rather difficult especially in layered structures where boundary conditions have to be satisfied at several interfaces [16].

This chapter describes a simple non-iterative method of obtaining solutions for surface waves in piezoelectric crystals using an orthonormal series to express field distributions. This method was applied earlier to acoustic waves in wedges [17, 18, 19, 20, 21]. The advantages of this method are:

- (1) It is simple to program and the solution is non-iterative. To find the velocity and field distribution for surface waves for

a given crystal orientation typically requires the diagonalization of  $18 \times 18$  matrix which takes only a few seconds on a computer.

- (2) The boundary conditions are incorporated into the field equations and automatically accounted for. This makes it convenient to account for complex boundary conditions such as those encountered in layered structures. Anisotropic piezoelectric layers can be taken into account. Second-order effects such as mass-loading are accurately accounted for and exact field distributions are obtained.
- (3) The field distributions are obtained as linear combinations of orthonormal functions making it convenient to perform further manipulations to obtain stress distributions, power flow, mode impedance, etc.

In section B the method of solution is described for surface waves along a free surface with an electrical open-circuit boundary condition. The velocity and field distributions are obtained for YZ LiNbO<sub>3</sub>. Using this solution the power flow and mode impedance are calculated and compared with perturbation theory results. The modifications required in the formulation to account for other kinds of electrical boundary conditions are then discussed.

Section D describes a formulation of the technique for layered structures. It is then applied to obtain the surface wave dispersion curves for a YZ LiTaO<sub>3</sub> substrate with a SiO<sub>2</sub> layer on the surface. The results are compared with those published earlier.

### B. Surface Waves on a Free Surface with an Electrical Open Circuit

The coordinate axes  $x_1, x_2, x_3$  are chosen so that the  $x_1$  axis is in the direction of propagation and the  $x_2$ -axis is perpendicular to the surface (Figure 27). The wave is assumed uniform along the  $x_3$ -direction.

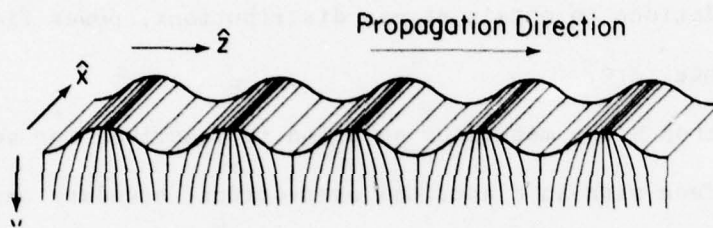


Figure 27. Surface waves.

Let  $u_1, u_2, u_3$  represent the components of particle displacement along  $x_1, x_2, x_3$  respectively and  $\phi$  represent the electric potential.  $T$  and  $D$  are the stress and electrical displacement.

The field equations are

$$\frac{\partial T_{ac}}{\partial x_c} = \rho \frac{\partial^2 u_a}{\partial t^2} \quad (42a)$$

$$\frac{\partial D_c}{\partial x_c} = 0 \quad (42b)$$

The indices a,c take on the values 1,2,3. Summation over repeated subscripts is implied throughout this paper. T and D are related to the field quantities u and  $\phi$  through the constitution relations

$$T_{ac} = (C_{acbd} \frac{\partial u_b}{\partial x_d} + e_{dac} \frac{\partial \phi}{\partial x_d}) \theta(x_2) \quad (43a)$$

where (1) the indices a,b,c,d take on the values 1,2,3

(2)  $\theta$  represents the unit step function

(3) C and e are the stiffness and piezoelectric tensors.

The unit step function in equation (43a) incorporates the stress-free boundary condition for the free surface. When this is substituted into equation (42a) it leads to delta functions,  $\delta(x_2)$  multiplying the normal stress components thus ensuring that the normal stress is zero at  $x_2 = 0$ .

For the present, an open-circuit electrical boundary condition is assumed so that the normal D-field is zero at the surface. This is taken into account in a similar manner with a step-function

$$D_c = (e_{cbd} \frac{\partial u_b}{\partial x_d} - \epsilon_{cd} \frac{\partial \phi}{\partial x_d}) \theta(x_2) \quad (43b)$$

where  $\epsilon$  is the permittivity tensor. The  $\theta$ -function gives rise to a term

$\delta(x_2)D_2$  in equation (42b) thus ensuring that  $D_2 = 0$  at  $x_2 = 0$  [24].

Methods for incorporating other electrical boundary conditions are discussed at the end of this section.

Combining equations (42) and (43) and assuming  $\exp(-i\omega t)$  time dependence

$$\rho \omega^2 u_a = A_{ab} u_b + B_a \phi \quad (44a)$$

$$0 = G_b u_b + F \phi \quad (44b)$$

where  $\rho$  = mass density and  $A_{ab}$ ,  $B_a$ ,  $G_b$  and  $F$  are operators defined by,

$$A_{ab} = -C_{acbd} X_{cd} \quad (45a)$$

$$B_a = -e_{dac} X_{cd} \quad (45b)$$

$$G_b = e_{cbd} X_{cd} \quad (45c)$$

$$F = -e_{cd} X_{cd} \quad (45d)$$

$$X_{cd} = \frac{\partial}{\partial x_c} \{ \theta(x_2) \frac{\partial}{\partial x_d} \} \quad (46a)$$

Dimensionless coordinates  $q_1, q_2, q_3$  are introduced for convenience

$$q_\alpha = k \cdot x_\alpha \quad \alpha = 1, 2, 3$$

where  $k$  is the magnitude of the wave-vector in the  $x_1$  direction. The operator  $X_{cd}$  (equation (46a)) is written as

$$X_{cd} = k^2 \frac{\partial}{\partial q_c} \{ \theta(q_2) \frac{\partial}{\partial q_d} \} = k^2 Q_{cd} \quad (46b)$$

The field quantities are expanded in a series of orthonormal functions in  $q_2$ :

$$u_a = \sum_{m=0}^{\infty} p_m^a |m(q_2)\rangle e^{iq_1} \quad (47a)$$

$$\phi = \sum_{m=0}^{\infty} r_m |m(q_2)\rangle e^{iq_1} \quad (47b)$$

where

$$|m(q_2)\rangle = e^{-q_2/2} P_m(q_2)/m!$$

and  $P_m$  represents the  $m^{\text{th}}$  Laquerre polynomial. The functions  $|m\rangle$  form a complete orthonormal set over  $(0, \infty)$  and are thus suitable for expressing distributions in a half-space. In practice, the infinite summations in equations (47a) and (47b) are truncated at some number  $N$ .  $N=5$  is usually adequate. The presence of the exponential factor is particularly convenient for the decaying field distributions encountered in surface waves. Only a few terms in the infinite series are required and the solution converges rapidly.

Using equations (47a) and (47b) in equations (44a) and (44b), multiplying by  $|j\rangle^*$  and integrating over  $q_2$  from 0 to  $\infty$ ,

$$\rho \frac{\omega^2}{k^2} p_j^a = p_j^a b p_m^b + Q_j^a m r_m \quad (48a)$$

$$0 = R_j b p_m^b + S_j m r_m \quad (48b)$$

where  $p_{jm}^{ab} = - C_{acbd} M_{cd}(j, m)$  (49a)

$$Q_m^a = - e_{dac} M_{cd}(j, m) \quad (49b)$$

$$R_{jm}^b = \epsilon_{cbd} M_{cd}(j,m) \quad (49c)$$

$$S_{jm} = -\epsilon_{cd} M_{cd}(j,m) \quad (49d)$$

and  $M_{cd}(j,m) = \int_0^\infty dq_2 |j\rangle^* Q_{cd}|m\rangle = \langle j|Q_{cd}|m\rangle$  (49e)

Equations (45) and (46) and the orthonormality of the polynomials has been used.  $M_{cd}(j,m)$  is evaluated in the Appendix.

Equations (48a) and (48b) are matrix equations in the expansion coefficients  $p$  and  $r$ ; the equations are combined to yield

$$p \frac{\omega^2}{k^2} \cdot p = (P - QS^{-1}R) \cdot p \quad (50a)$$

$$r = S^{-1}Rp \quad (50b)$$

where  $p$  and  $r$  are column vectors with components  $p_m^a$  and  $r_m$ . The eigenvalues of  $(P - QS^{-1}R)$  yield the value of  $\rho\omega^2/k^2$  and hence the surface wave velocity ( $= \omega^2/k^2$ ). The eigenvectors yield the field distributions.

The summations in equations (47a) and (47b) are truncated at some number  $N$ . The order of the matrix in equation (50a) is then  $3(N+1)$ . The solution is assumed to converge when the eigenvalue does not change appreciably as  $N$  is increased. It is found that  $N=5$  is usually sufficient.

This method was used to obtain surface wave solutions in YZ LiNbO<sub>3</sub>. The velocity obtained with  $N=3$  is 3492.1 m/sec and with  $N=7$  is 3489.7 m/sec showing acceptable convergence. This agrees well with the published velocity of 3487.7 m/sec.

The field distributions are obtained as linear combinations of orthonormal functions from equations (47a) and (47b) the coefficients  $p_m^a$  and  $r_m$  being obtained from the eigenvectors in equation (50). In Figure 28,  $u_1, u_2$  and  $\phi$  are shown as a function of depth;  $u_3$  is identically zero.

The stress and electric displacement are obtained by using equations (43a) and (43b).

$$T_{ac} = \sum_{m=0}^N K [C_{acbd} \frac{\partial}{\partial q_d} p_m^b |m\rangle e_{dac} \frac{\partial}{\partial q_d} r_m |m\rangle] \quad (51a)$$

$$D_c = \sum_{m=0}^N K [e_{cbcd} \frac{\partial}{\partial q_d} p_m^b |m\rangle - e_{cd} \frac{\partial}{\partial q_d} r_m |m\rangle] \quad (51b)$$

The power flow per unit area in the  $x_1$ -direction is written as

$$P_1 = \frac{i\omega}{2} [u_a^* \cdot T_{a1} + \phi D_1^*] \quad (52)$$

Using the expressions for  $u$ ,  $\phi$ ,  $T$  and  $D$  in equation (52) and integrating over  $x_2$  from 0 to  $\infty$

$$P_1 = P_M + P_{ME} + P_E$$

where

$$P_M = -\frac{i\omega}{2} [C_{acbd} p_j^{a*} p_m^b \langle j | \frac{\partial}{\partial q_d} |m\rangle] \quad (53a)$$

$$P_{ME} = -\frac{i\omega}{2} [(e_{dac} + e_{cad}) p_j^{a*} r_m \langle j | \frac{\partial}{\partial q_d} |m\rangle] \quad (53b)$$

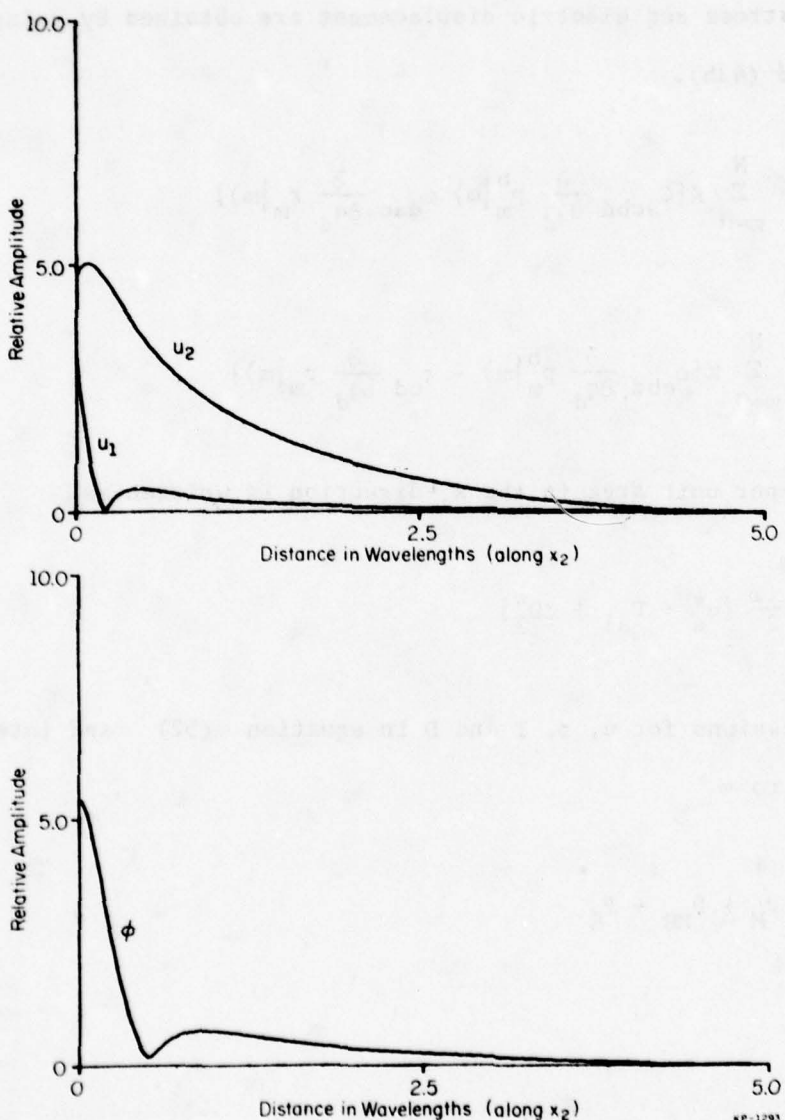


**Figure 28.** Plot of field distributions with depth.  
 a)  $U_1$  (compressional displacement) and  $U_2$  (shear displacement).  
 b)  $\phi$  (electric potential).

$$P_E = \frac{i\omega}{2} [\epsilon_{cd} r_j^* r_m \langle j | \frac{\partial}{\partial q_d} | m \rangle] \quad (53c)$$

The indices a,b,c,d are summed over 1,2,3 while indices j,m are summed from 0 to N,  $P_M$  is the mechanical power,  $P_{ME}$  is the electromechanical power and  $P_E$  is the electrical power.

Knowing the coefficients p and r,  $P_M$ ,  $P_{ME}$  and  $P_E$  are calculated from equations (53a), (53b), and (53c). This was done for the surface wave in YZ LiNbO<sub>3</sub> giving

$$u_1(x_2=0) = (3.07 + j 1.09) \text{ m.}$$

$$u_2(x_2=0) = (-1.63 + j 4.5) \text{ m.}$$

$$\phi(x_2=0) = (-2.47 - j 1.11) \times 10^{10} \text{ V.}$$

$$P_M = 621.4 \times 10^{10} \text{ uW/m.}$$

$$P_{ME} = 48.6 \times 10^{10} \text{ uW/m.}$$

$$P_E = 22.1 \times 10^{10} \text{ uW/m.}$$

The mode impedance Z [25] is obtained

$$Z = \frac{|\phi(x_2=0)|^2}{2(P_M + P_{ME} + P_E)} = \frac{5.3 \times 10^7}{\omega} \Omega \cdot \text{m.}$$

This agrees well with the value computed from perturbation theory

$$Z = \frac{1}{\omega(\epsilon_p + \epsilon_0)} \cdot \frac{\Delta V}{V} = \frac{5.5 \times 10^7}{\omega} \Omega \cdot \text{m.}$$

### C. Surface Waves on Conductive Surfaces

In the last section, a step function was used in the constitutive relation (equation (43b)) to ensure that  $D_2=0$  at the surface. Other electrical boundary conditions can be incorporated in a similar manner.

A common boundary condition is the short circuit case where the tangential electrical field  $E_1$  is zero at the surface. This is incorporated by adding a term  $\delta(X_2)E_1$  to the field equations. The matrix elements are easily evaluated using the relations in the Appendix. Another approach is to expand the electric potential as

$$\phi = \sum_{m=0}^N r_m q_2 |m\rangle e^{iq_1 l}.$$

This ensures that  $\phi$  is zero at  $q_2=0$ . The matrix elements are obtained easily by noting that

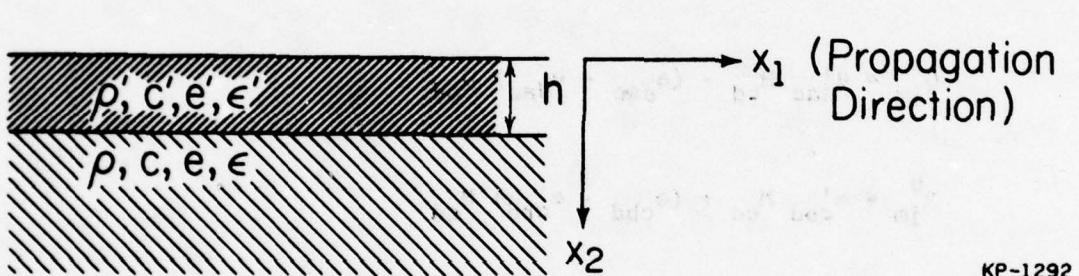
$$q_2 |m\rangle = - (m+1) \cdot |m+1\rangle + (2m+1) |m\rangle - m |m-1\rangle \quad (54)$$

Using either method the velocity and field distributions are obtained for a shorted surface which agrees well with published results.

We believe that finite conductivity films can also be taken into account similarly; however, the details have not been worked out.

#### D. Surface Waves in Layered Structures

In this section the problem is discussed for a single layer of thickness  $h$  with material constants  $\rho'$ ,  $C'$ ,  $e'$  and  $\epsilon'$  over a substrate with constants  $\rho$ ,  $C$ ,  $e$  and  $\epsilon$  (Figure 29). An electrical open circuit is assumed at the surface



KP-1292

Figure 29. Layered structure with  $\text{SiO}_2$  over  $\text{LiTaO}_3$ .

The layer is taken into account by writing the stiffness coefficient as

$$C\theta(q_2 - kh) + C'(\theta(q_2) - \theta(q_2 - kh))$$

in the constitutive relation.  $e$  and  $\epsilon$  are also written similarly. The mass-density is written similarly in the field equation.

With these modifications equations (48a) and (48b) become

$$\begin{aligned}
 & (\rho - \rho') \frac{\omega^2}{k^2} \langle j | \theta(q_2 - kh) | i \rangle p_i^a + \rho' \frac{\omega^2}{k^2} \cdot p_j^a \\
 & = P_{jm}^{ab} p_m^b + Q_{jm}^a r_m
 \end{aligned} \tag{55a}$$

$$0 = R_{jm}^b p_m^b + S_{jm} r_m \tag{55b}$$

where  $P_{jm}^{ab} = C'_{acbd} M_{cd} - (C_{acbd} - C'_{acbd}) H_{cd}$

$$Q_{jm}^a = e'_{dac} M_{cd} - (e_{dac} - e'_{dac}) H_{cd}$$

$$R_{jm}^b = e'_{cbd} M_{cd} + (e_{cbd} - e'_{cbd}) H_{cd}$$

$$S_{jm} = \epsilon'_c M_{cd} - (\epsilon_{cd} - \epsilon'_c) H_{cd}$$

and  $H_{cd} = \langle j | \frac{\partial}{\partial q_c} \theta(q_2 - kh) \frac{\partial}{\partial q_d} | m \rangle$

Equation (55a) is rewritten as

$$\rho' \frac{\omega^2}{k^2} p_j^a = \{P_{jm}^{ab} - (\rho - \rho') \frac{\omega^2}{k^2} \langle j | \theta(q_2 - kh) | m \rangle\} p_m^b + Q_{jm}^a r_m \tag{55c}$$

Equations (55b) and (55c) are now solved in a manner similar to Section VI-B. The only difference is the presence of a term containing  $\omega^2/k^2$  on the right hand side. A simple iteration is required to converge on the correct velocity.

This method was applied to an  $\text{SiO}_2$  layer on a  $\text{LiTaO}_3$  substrate.

The result is shown in Figure 30 and compared against results published earlier [26].

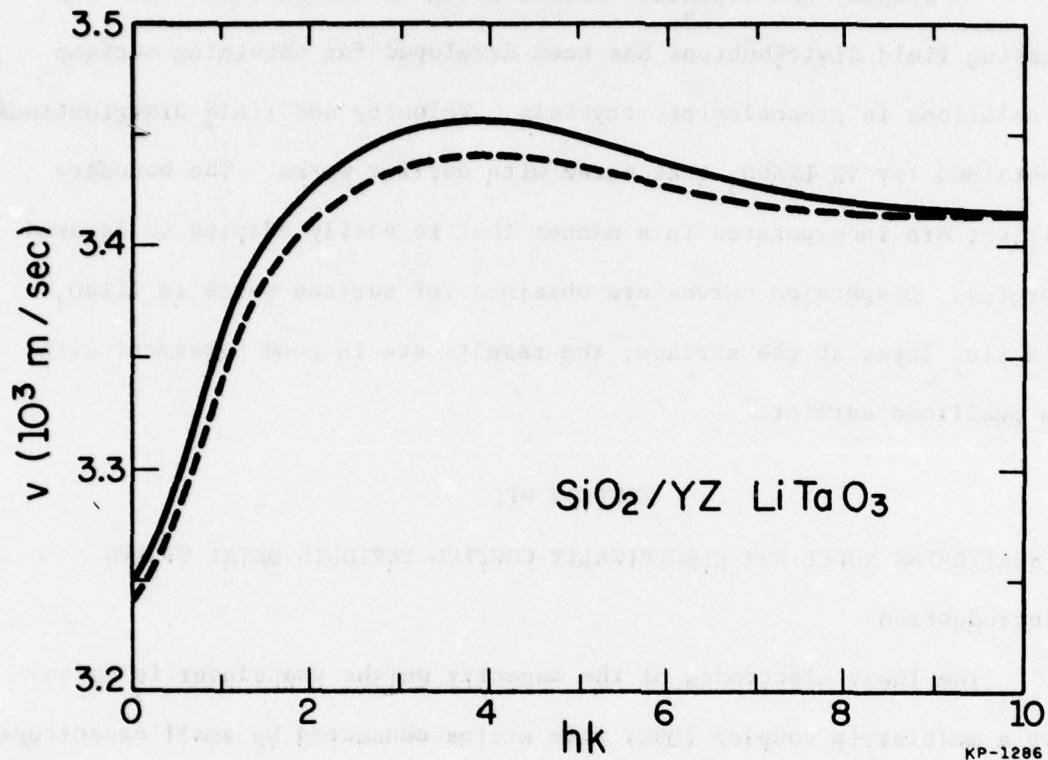


Figure 30. Variation of velocity with film thickness.

Present theory

----- Reference 26

This technique may be extended to include multi-layers and finite thickness plates.

### E. Conclusions

A simple, non-iterative method using an orthonormal basis for expressing field distributions has been developed for obtaining surface wave solutions in piezoelectric crystals. Velocity and field distributions are obtained for YZ LiNbO<sub>3</sub> that agree with earlier works. The boundary conditions are incorporated in a manner that is easily adapted to layered structures. Dispersion curves are obtained for surface waves in LiTaO<sub>3</sub> with a SiO<sub>2</sub> layer at the surface; the results are in good agreement with those published earlier.

## SECTION VII

### SCATTERING MODEL FOR ELECTRICALLY COUPLED PERIODIC METAL STRIPS

#### A. Introduction

The lower electrodes of the capacity weight transducer is essentially a multistrip coupler (MSC) with strips connected by small capacitors to the buss bars. The MSC is usually analyzed using the Mason model [27] or in terms of the normal modes of the coupler [28, 29, 30, 31] but neither approach is conveniently expanded to account for the coupling capacitors. This chapter describes a simple physical model that views the coupling as a process of regeneration by each strip in succession. Each strip of the MSC samples the potential of the incoming acoustic wave and applies it to all the tracks giving rise to regenerated waves whose amplitudes are calculated from a simple IDT equivalent circuit [32]. This yields the transmission matrix of a single strip relating the output and input wave amplitudes in different tracks. The overall characteristics of the coupler are obtained by cascading the transmission matrices of successive strips.

The advantages of this approach are:

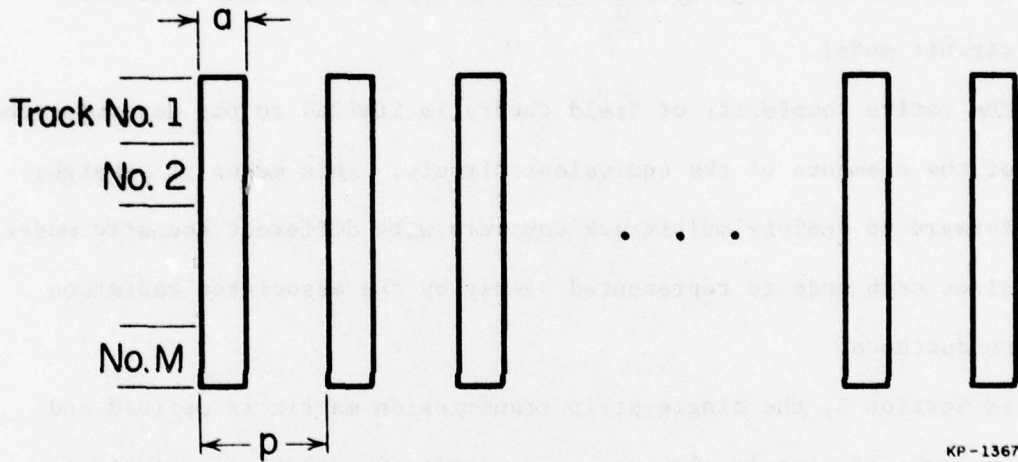
- (1) The analysis is on a strip by strip basis. This makes it possible to obtain numerical solutions for non-periodic couplers with slowly varying pitch, electrode length or metallization ratio.
- (2) The model is based on the well-known IDT equivalent circuit lending additional physical insight. The effects of external load, strip resistance losses, negative resistance (as in strip-coupled amplifiers) and coupling capacitors are easily incorporated into the circuit model.
- (3) The entire complexity of field theory is limited to the determination of the elements of the equivalent circuit. This makes it straightforward to analyze multitrack couplers with different acoustic modes, since each mode is represented simply by the associated radiation conductance.

In Section B, the single strip transmission matrix is defined and evaluated in terms of circuit elements. In Section C analytical solutions are obtained for some common periodic couplers using this approach. Numerical solution for a non-periodic strip-coupled UDT is obtained in Section D which is in agreement with previous experimental results [31].

## B. Theoretical Formulation

### 1. Transmission Matrix

Since the MSC (Figure 31) is a linear system the amplitudes of the incoming and outgoing acoustic waves in different tracks of a single

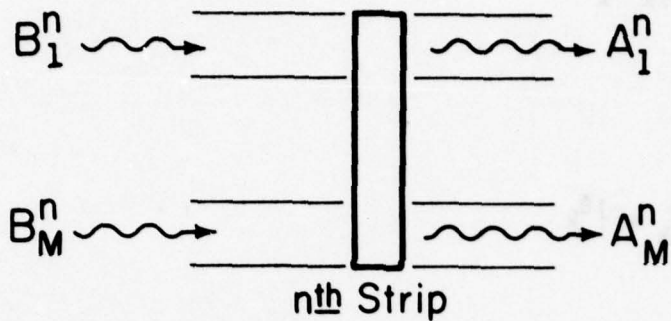


KP-1367

Figure 31. A multistrip coupler with  $M$  tracks.

strip (Figure 32) are related by a transmission matrix  $b_{ik}^n$  (for the  $n^{\text{th}}$  strip):

$$A_i^n = \sum_k b_{ik}^n B_k^n \quad (56a)$$



KP-1568

Figure 32. Incoming and outgoing waves in M tracks of the n<sup>th</sup> strip.

where  $B_k^n$  = amplitude of acoustic wave incident on the n<sup>th</sup> strip in track k.

$A_i^n$  = amplitude of acoustic wave emerging from the n<sup>th</sup> strip in track i.

Backward waves are neglected in this formulation so that it is valid only outside the stop band.  $B_i^n$  is related to  $A_i^{n-1}$  by a simple phase factor:

$$B_i^n = e^{-j\theta_i} A_i^{n-1} \quad (56b)$$

where,  $\theta_i = k_i p_i$

$k_i$  = wave vector in track i

$p_i$  = distance between the (n-1)<sup>th</sup> and n<sup>th</sup> strips in track i

Combining (56a) and (56b),

$$A_i^n = \sum_k a_{ik}^n A_k^{n-1} \quad (57a)$$

where,

$$a_{ik}^n = b_{ik}^n e^{-j\theta_k}$$

In matrix form,

$$\{A^n\} = [a^n] \{A^{n-1}\} \quad (57b)$$

It follows that,

$$\begin{aligned} \{A^N\} &= [a^N] [a^{N-1}] \dots [a^1] \{A^0\} \text{ (for } N \text{ strips)} \\ &= [a]^N \{A^0\} \end{aligned} \quad (57c)$$

if the strips are uniform so that  $[a^N] = [a^{N-1}] = \dots [a^1] = [a]$ . Equation (57a) is a set of difference equations that can be solved to yield analytical solutions for  $\{A_n\}$ . Equation (57c) is used for a numerical evaluation of  $\{A_N\}$  with a given set of initial amplitudes  $\{A_0\}$ .

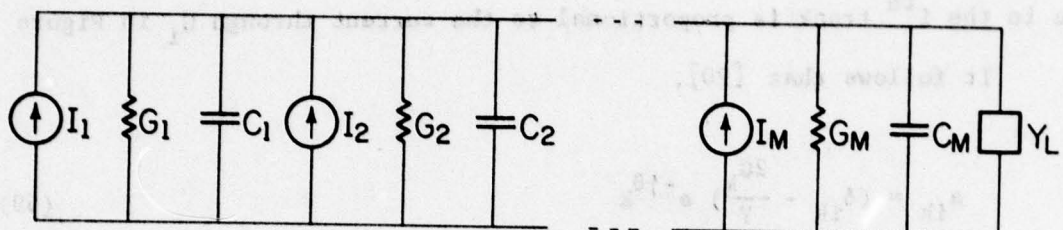
## 2. Evaluation of Matrix Elements

The matrix elements  $a_{ik}$  will now be related to IDT circuit elements.

Each track of a single strip has an equivalent circuit with the radiation conductance  $G_m$  in parallel with the capacitance  $C_m$  (for the  $m^{\text{th}}$  track).

Since all tracks in a strip have the same voltage, the equivalent circuit

for different tracks are connected in parallel (Figure 33).  $Y_L$  represent any external load connected to the strip.



KP-1374

Figure 33. Equivalent circuit for one strip with  $M$  tracks.  $Y_L$  is an external load (strip resistance neglected).

The current generator  $I_m$  is defined as the current generated in the strip when excited by an incoming acoustic wave in the  $m^{\text{th}}$  track with the strips shorted together. This current is proportional to the radiation conductance of the  $m^{\text{th}}$  track. The effective amplitude of the acoustic wave  $A_m$  is defined as the ratio of the short circuit current to the radiation conductance:

$$A_m = I_m / G_m \quad (58a)$$

The power in the wave  $P_m$  is,

$$P_m = A_m^2 G_m / 2 \quad (58b)$$

From equation (57a) it follows that  $a_{ik}^n$  is the emerging wave in the  $i^{th}$  track when only the  $k^{th}$  track is excited. The emergent wave is the superposition of the incident wave and the regenerated wave. The regenerated wave in the  $i^{th}$  track is proportional to the current through  $G_i$  in Figure 33. It follows that [20],

$$a_{ik} = (\delta_{ik} - \frac{2G_k}{Y}) e^{-j\theta_k} \quad (59)$$

where,

$$Y = Y_L + j\omega C + G$$

$$C = \sum_{m=1}^M C_m \quad (\text{for } M \text{ tracks})$$

$$G = \sum_{m=1}^M G_m$$

and,

$$\delta_{ik} = \begin{cases} 1 & , i = k \\ 0 & , i \neq k \end{cases}$$

(The superscript  $n$  indicating the strip number is dropped for convenience.)

The term  $\delta_{ik}$  represents the contribution from the incident wave while the second term is the forward regenerated wave. The factor of 2 in the regenerated wave arises because outside the stopband the backward waves

cancel providing a unidirectional regenerated wave in the forward direction.

It is easily seen that power is conserved in this evaluation of scattering parameters.

Equations (57) and (59) provide a complete description of the MSC in terms of circuit elements. This model may be used for different acoustic modes once the associated radiation conductance is evaluated. We will now specialize to surface wave tracks, and in the next section it will be shown that the solution of equation (57a) yields results in agreement with those derived earlier.

By a superposition of solutions it may be shown that the appropriate  $G_m$  and  $C_m$  (for a single strip with end effects neglected) are those of an array of strips in which all strips other than the one in consideration are grounded. The conductance and capacitance of such a structure are the same as those of a single electrode in an IDT array.

Thus, for surface wave tracks we obtain from equation 13 of Reference 33,

$$\gamma = \frac{G_m}{\omega C_m} = \frac{K^2}{2} \frac{\sin ms}{P_{-s} (\cos \Delta) P_s (-\cos \Delta)} \quad (60)$$

where,

$$s = p/\lambda$$

$$\Delta = a/p$$

K is the electromechanical coupling coefficient

and  $P_v$  is the Legendre function of order v

Verhouding tussen de ene en de andere capaciteit in een geïsoleerde schijf

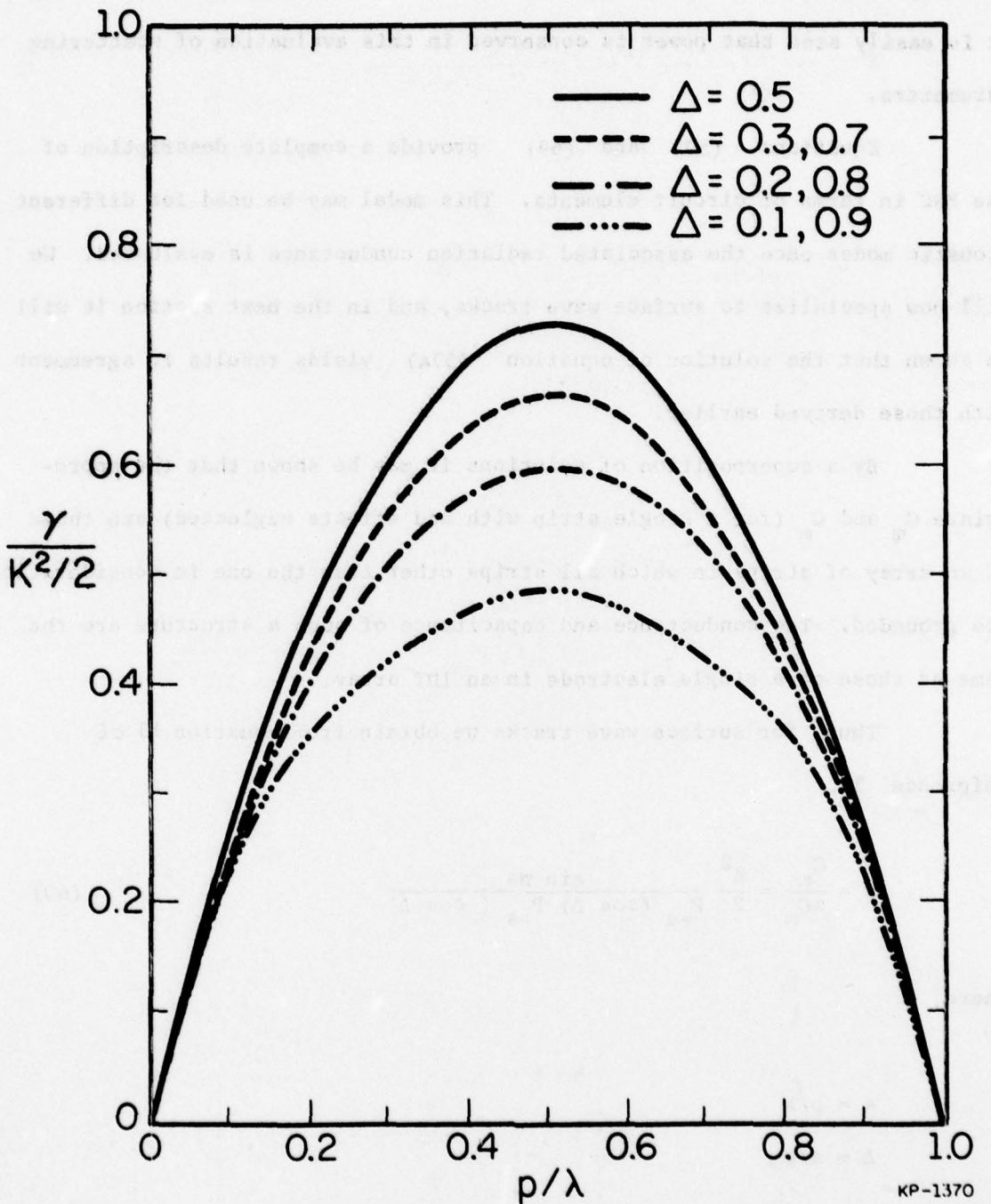


Figure 34. Ratio of single strip conductance to capacitance (normalized to the coupling coefficient) as a function of strip period with the metallization ratio as a parameter.

The capacitance is given by,

$$C_m = L_m (\epsilon_0 + \epsilon_p) \sin \pi s \frac{P_{-s} (\cos \Delta)}{P_{-s} (-\cos \Delta)}$$

where

$L_m$  = width of  $m^{\text{th}}$  track

and  $\epsilon_p$  = substrate permittivity

Figure 34 gives a plot of  $\frac{\gamma}{K/2}$  (equation (60)) as a function of  $s$  with  $\Delta$  as a parameter.

### 3. Strip Resistance Losses

The effect of strip resistance is included in this formulation by including series resistance elements in the equivalent circuit (Figure 33)

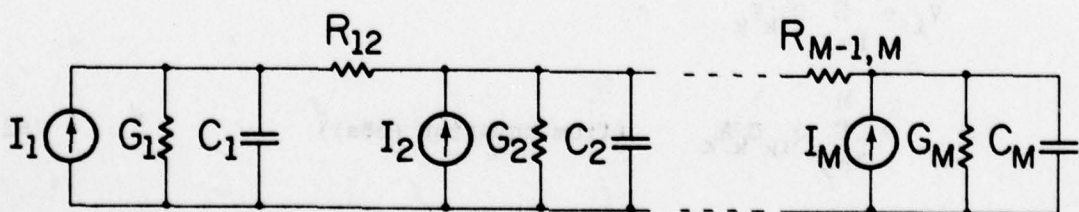


Figure 35. Equivalent circuit for one strip with strip resistance included.

as shown in Figure 35.  $R_{m,m+1}$  represents the resistance along a strip from the center of the  $m^{\text{th}}$  track to the center of  $(m+1)^{\text{th}}$  track.

$$R_{m,m+1} = \frac{R_{\square}}{2} \left( \frac{l_m}{a_m} + \frac{l_{m+1}}{a_{m+1}} \right) \quad (61)$$

where,

$l_m$  is the width of the  $m^{\text{th}}$  track

and

$a_m$  is the strip width in the  $m^{\text{th}}$  track

$R_{\square}$  is the sheet resistance of the strip

This model for strip resistance is discussed in Reference 31.

The coefficients  $a_{ik}$  of the transmission matrix are obtained from the equivalent circuit of Figure 35 by solving for the node voltages  $V_1, \dots, V_M$  in terms of the current generators.

$$V_i = \sum_{k=1}^M Q_{ik} I_k$$

$$= \sum_{k=1}^M Q_{ik} G_k A_k \quad (\text{from equation (58a)}) \quad (62)$$

where  $Q_{ik}$  (a function of the resistances  $R$ , the conductances,  $G$ , and the capacitances,  $C$ ) is obtained from the node equations. The regenerated wave in the  $i^{\text{th}}$  track is proportional to  $V_i$  so that the transmission matrix is

$$a_{ik} = (\delta_{ik} - Q_{ik} G_k) e^{-j\theta_i} \quad (63)$$

It is difficult to obtain a general analytic expression for  $Q_{ik}$ ; however, a straightforward numerical calculation is required to evaluate it for a given problem.

#### 4. Normal Modes of the Coupler

The normal modes of the coupler are easily determined from the present model. A normal mode retains its shape as it is transmitted through the coupler. Thus the eigenvectors of the transmission matrix [a] provide the normal mode distributions and the eigenvalues represent the corresponding propagation constants.

This method makes it straightforward to obtain the normal modes of a coupler with many tracks involving different acoustic modes. For non-periodic couplers, the overall transmission matrix is obtained by cascading the transmission matrices of individual strips. The normal modes are then described by the eigenvalues and eigenvectors of the overall transmission matrix.

### C. Special Cases with Analytical Solutions

In this section analytical solutions are obtained by solving equation (57a) for certain special cases and shown to agree with the standard results.

#### 1. Two Track Surface Wave Coupler

For two tracks only, equation (57a) yields a set of two difference equations:

$$A_1^n = a_{11}^n A_1^{n-1} + a_{12}^n A_2^{n-1} \quad (64a)$$

$$A_2^n = a_{21}^n A_1^{n-1} + a_{22}^n A_2^{n-1} \quad (64b)$$

where  $a_{11}^n$ ,  $a_{12}^n$ ,  $a_{21}^n$ ,  $a_{22}^n$  are given by equation (59) for the  $n^{\text{th}}$  strip.

Assuming an incident wave of unit amplitude in track 1 only ( $A_1^0 = 1$ ,  $A_2^0 = 0$ ), the solution to equation (64) is obtained as,

$$A_1^N = \frac{q^N (q-a_{22}) + r^N (a_{22}-r)}{q-r} \quad (65a)$$

$$A_2^N = a_{21} \cdot \frac{q^N - r^N}{q-r} \quad (65b)$$

where  $q$  and  $r$  are given by,

$$q + r = a_{11} + a_{22} \quad (66a)$$

$$qr = a_{11}a_{22} - a_{12}a_{21} \quad (66b)$$

The strips are assumed uniform so that the superscript  $n$  on the  $a_{ik}$ 's has been dropped.

Equations (65a) and (65b) are rewritten as,

$$A_1^N = \frac{2\alpha_2\gamma + (2\alpha_1\gamma - \varphi)e^{jN(2\gamma - \varphi)}}{2\gamma - \varphi} e^{-jN\theta} \quad (67a)$$

$$A_2^N = -2\alpha_1\gamma \frac{1 - e^{jN(2\gamma - \varphi)}}{2\gamma - \varphi} e^{-jN\theta} \quad (67b)$$

where

$$\alpha_1 = \frac{G_1}{G}$$

$$\gamma = \frac{G}{\omega C}$$

$$\varphi = k(p_1 - p_2)$$

$$\theta = k(p_1 + p_2)$$

Two assumptions are made in the derivation - that  $\gamma \ll 1$  and  $\varphi \ll 1$ . The external load  $Y_L$  is assumed zero.

Using equations (67a) and (67b) solutions for specific cases are obtained and compared with earlier results.

#### a. Identical Tracks

In this case,  $\varphi = 0$  and  $\alpha_1 = \alpha_2 = .5$ . Thus, equations (67a) and (67b) reduce to,

$$A_1^N = \frac{1}{2} [1 + e^{j2N\gamma}] e^{-jN\theta}$$

$$A_2^N = -\frac{1}{2} [1 - e^{j2N\gamma}] e^{-jN\theta}$$

Complete power transfer is obtained when  $A_1^N = 0$  and  $A_2^N = 1$ . The number of strips required is given by,

$$N_T = \frac{\pi}{2Y}$$

This agrees with the result in Reference 28.

#### b. Unequal Tracks with Identical Periods

Here  $\phi = 0$  but  $\alpha_1 \neq \alpha_2$ . The solutions are written as,

$$A_1^N = (\alpha_2 + \alpha_1 e^{j2NY}) e^{-jN\theta}$$

$$A_2^N = -\alpha_1 (1 - e^{j2NY}) e^{-jN\theta}$$

In this case complete transfer is not possible. The minimum value of  $A_1^N$  is  $\alpha_2 - \alpha_1$  and the corresponding value of  $A_2^N$  is  $-2\alpha_1$ . The maximum fractional power transferred is given by,

$$F_T = 1 - (\alpha_2 - \alpha_1)^2$$

$$= \frac{4\ell_1\ell_2}{(\ell_1 + \ell_2)^2}$$

where  $\ell_1$  and  $\ell_2$  are the widths of the tracks. This agrees with Reference 27.

#### c. Unequal Tracks with Different Periods

From equation (67a) it is apparent that complete power transfer is possible if,

AD-A060 395

ILLINOIS UNIV AT URBANA-CHAMPAIGN COORDINATED SCIENCE LAB  
SURFACE ACOUSTIC WAVE TRANSDUCER STUDY. (U)  
MAY 78 B J HUNSINGER

F/G 17/1

F33615-75-C-1291

NL

UNCLASSIFIED

AFAL-TR-78-60

2 of 2  
AD  
A060 395



END  
DATE  
FILED  
1-79  
DDC

$$2\alpha_2 Y = 2\alpha_1 Y - \varphi$$

$$\text{i.e., } \varphi = 2(\alpha_1 - \alpha_2)Y$$

This yields,

$$\frac{P_1}{P_2} = \frac{\ell_2 + \ell_1 (1 + \frac{2Y}{kp})}{\ell_1 + \ell_2 (1 + \frac{2Y}{kp})}$$

$$\text{where } p = \frac{1}{2} (P_1 + P_2).$$

This agrees with the result in Reference 28.

## 2. Strip Coupled Surface Wave Amplifier

Reference 30 describes a surface wave amplifier with the surface wave coupled to a semiconductor with drifting carriers by an MSC. This system is treated in the present formulation as a single track coupler with an external load  $Y_L$ . When the carrier drift velocity exceeds the acoustic wave velocity,  $\text{Re}(Y_L)$  is negative providing amplification.

Since the coupler has only one track, equations (57c) and (59b) yield,

$$A^N = (1 - \frac{2G}{Y})^N e^{-jN\theta} \cdot A^0$$

$$\text{where, } Y = (G + G_S) + j\omega(C + C_S)$$

$G_S$  and  $C_S$  being the conductance and capacitance of the semiconductor as seen from the strip.

The gain in dB is then given by,

$$\text{Gain} = -8.68 N \frac{\frac{2G_S G}{S}}{\omega^2 (C+C_S)^2} \quad (68)$$

where the assumption that  $(G+G_S)/\omega(C+C_S) \ll 1$  has been made.

Using the  $G_S$  and  $C_S$  as derived in Reference 30 and  $G$  and  $C$  as defined in this chapter, equation (68) is shown to be equivalent to equation (61) of Reference 30.

### 3. Normal Modes of the Two Track Coupler

It is well-known that a coupler with two identical tracks has symmetric and antisymmetric modes which have a phase-shift with respect to each other. This also follows simply from the discussion of Section B-3.

A coupler with two identical tracks has the transmission matrix

$$[a] = \begin{bmatrix} 1 - \frac{G}{y} & -\frac{G}{y} \\ -\frac{G}{y} & 1 - \frac{G}{y} \end{bmatrix}$$

The eigenvectors of  $[a]$  are  $\begin{pmatrix} 1 \\ 1 \end{pmatrix}$  and  $\begin{pmatrix} 1 \\ -1 \end{pmatrix}$  with eigenvalues  $e^{i2Y}$  and 1 where  $\gamma = G/\omega C \ll 1$ . Thus the normal modes are symmetric and antisymmetric with respect to the center and have a relative phase shift of  $2Y$  per section.

The number of strips needed for complete power transfer from one track to another is thus given by,

$$N_T = \pi/2\gamma$$

in agreement with the result in the previous section.

#### 4. Strip Resistance Losses for Two Track Coupler

The attenuation coefficient due to strip resistance in a coupler with two identical tracks has been calculated in Reference 27. The same result follows from the equivalent circuit (Figure 35) using the formulation of Section B-4.

For a two-track coupler a simple analysis of the equivalent circuit yields

$$\begin{aligned}
 a_{11} &= 1 - \frac{2G_1}{Y_1} \cdot \frac{R + \frac{1}{Y_2}}{R + \frac{1}{Y_1} + \frac{1}{Y_2}} \\
 a_{12} &= \frac{-2G_1}{Y_2} \cdot \frac{\frac{1}{Y_1}}{R + \frac{1}{Y_1} + \frac{1}{Y_2}} \\
 a_{21} &= \frac{-2G_2}{Y_1} \cdot \frac{\frac{1}{Y_2}}{R + \frac{1}{Y_1} + \frac{1}{Y_2}} \\
 a_{22} &= 1 - \frac{2G_2}{Y_2} \cdot \frac{R + \frac{1}{Y_1}}{R + \frac{1}{Y_1} + \frac{1}{Y_2}}
 \end{aligned} \tag{69}$$

where  $Y_i = G_i + j\omega C_i$

$$R = R_{12}$$

For identical tracks, the eigenvalues for the symmetric and anti-symmetric modes are obtained as  $e^{i2\gamma}$  and  $e^{-\gamma\omega CR}$ . As expected, the symmetric mode does not suffer attenuation while the antisymmetric mode is attenuated;

and the attenuation coefficient per coupler length for the antisymmetric mode is,

$$\alpha = \gamma w_{CR} \cdot \frac{\pi}{2\gamma} = \pi^2 f_{CR} \quad (70)$$

This agrees with Reference 27. (The factor of 2 in Reference 27 is missing here, because C refers to the total capacitance of both tracks.)

#### D. Numerical Analysis

One of the main advantages of this strip-by-strip analysis is in the modeling of non-periodic couplers. This requires a numerical evaluation of equation (57c):

$$\{A^N\} = [a^N] [a^{N-1}] - - - - [a^1] \{A^0\} \quad (71)$$

For a given input  $\{A^0\}$ , the output  $\{A^N\}$  after N strips are evaluated numerically by straightforward matrix multiplication. Various periodic couplers have been analyzed using this approach yielding results in agreement with Reference 31.

The UDT structure in Figure 36 is an example of a non-uniform coupler [31] that is modeled in a straightforward manner using the present approach. The semi-circular portion provides a capacitive loading that varies from strip to strip. It also generates waves causing losses.

In the conventional analysis the semi-circular region is approximated by a capacitive load that is assumed constant for all the strips; and the generation in this region is neglected [31]. This theory predicts an infinite forward to reverse ratio and zero conversion loss. In practice the forward to reverse ratio of 22 dB and a loss of 2.5 dB (Figure 37) was reported in Reference 31.

Using the present formulation an accurate model for this complex structure is obtained. The semicircular region is divided into twenty tracks, each track having a radiation conductance determined from the

coupling coefficient in the radial direction. Also, the changing velocity in different directions is taken into account in evaluating  $\theta_i$  (equation 56b). The length of the semicircular region and hence the capacitance

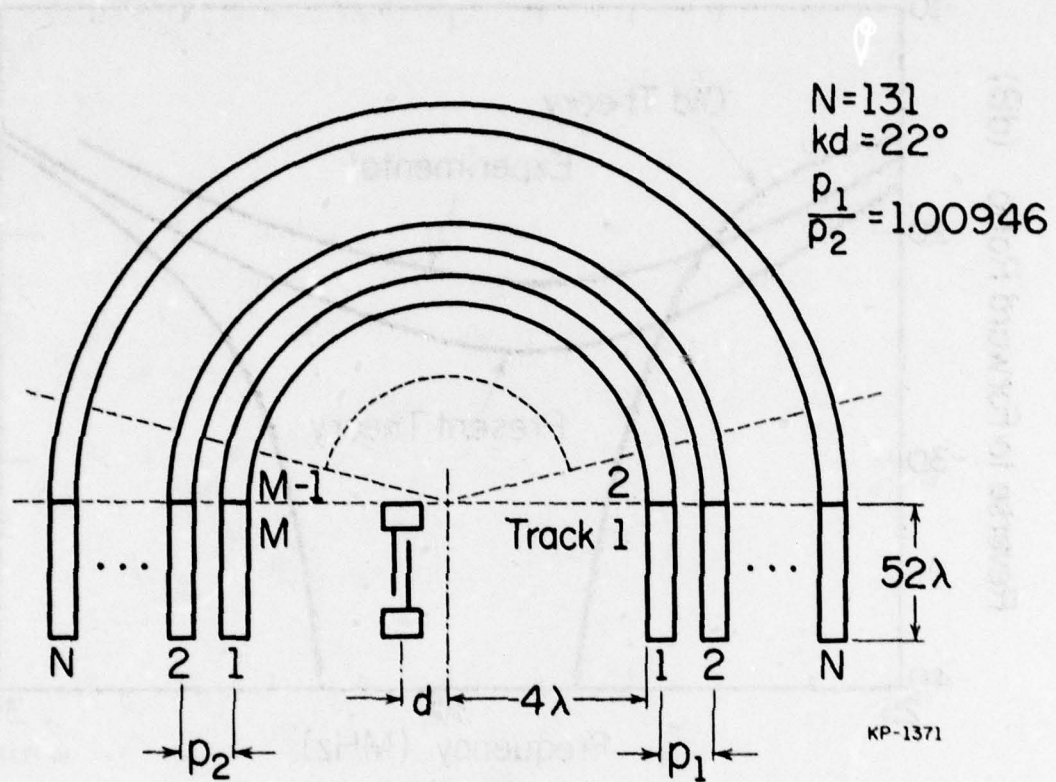
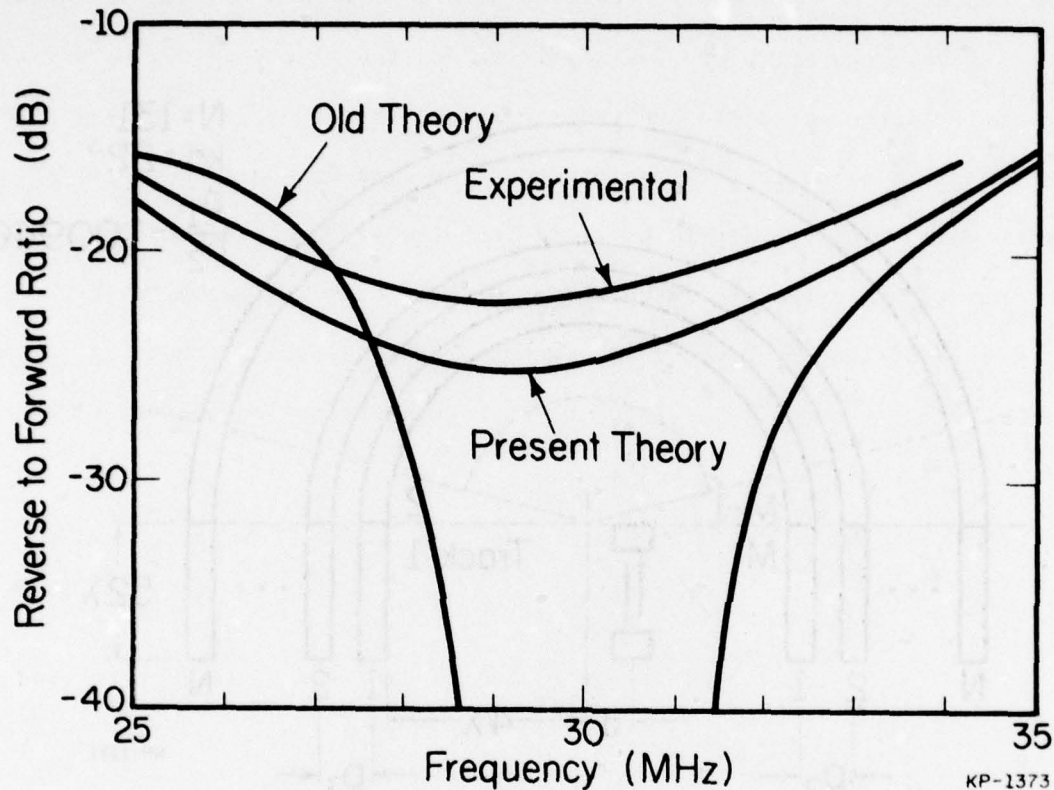


Figure 36. A strip-coupled UDT.

and conductance increase for the outer strips. This is accounted for in the evaluation of  $[a^n]$  in equation (71).

Using this model the reverse to forward ratio is obtained as shown in Figure 37. This is seen to be in close agreement with the experimental result. The analysis shows that 1 dB of the 2.5 dB measured loss is attributed to SAWs generated in the semicircular region.



**Figure 37.** Reverse to forward ratio versus frequency for a strip coupled UDT.

The exact value of the loss and minimum reverse-to-forward ratio are found to be quite sensitive to the wave velocities in the various tracks. This makes it difficult to design the structure without empirical adjustments; this has also been observed experimentally.

This analysis shows the feasibility of using the present approach in the treatment of very complicated coupler structures that are not amenable to analysis by conventional techniques.

### E. Conclusions

A strip by strip analysis of multistrip couplers is formulated using the well-known equivalent circuit for an interdigital transducer. The approach is shown to yield the correct results for some common coupler configurations. The strip-coupled amplifier and the effect of strip-resistance on coupler performance are analyzed as simple extensions of the same model. This approach makes it straightforward to analyze non-uniform couplers that are not amenable to analysis by usual techniques. A strip-coupled UDT is analyzed to yield results in agreement with experimental results which have not been explained by previous theories. This theory is directly applicable to the analysis capacity weighted electrodes operating in uniform beams.

## SECTION VIII

### HARMONIC ANALYSIS OF SAW TRANSDUCERS

#### A. Introduction

An experimental analysis technique has been devised which produces the time domain excitation function of an isolated IDT. The time domain excitation function is defined as the instantaneous surface acoustic wave amplitude displacement distribution resulting from a voltage impulse applied to the transducer. Works of Engan [34], Hartmann and Secrest [35], Smith and Pedler [6], Bahr and Lee [36], and Szabo et al. [37] have presented theoretical descriptions of the SAW electric fields produced by the IDT.

This chapter describes a technique for measuring the SAW amplitudes produced by these driving source fields. The time domain excitation function is found by measuring the transducer frequency domain voltage transfer ratio in a low impedance system and transforming it to produce the time domain SAW amplitude distribution resulting from the driving source fields.

## B. Sampled Time Domain Calculations

The frequency domain transfer ratio is measured for the distinct purpose of being transformed to the time domain. The frequencies at which the transfer functions are measured must be sufficiently close together to account for the longest time delay component in the impulse response. The sampling theorem assures that no errors arise in the transform if the frequency measurements are taken at a spacing of

$$\Delta f \leq \frac{1}{T_{\max}} \quad (72)$$

where  $T_{\max}$  is maximum time range of the impulse response (Figure 38).

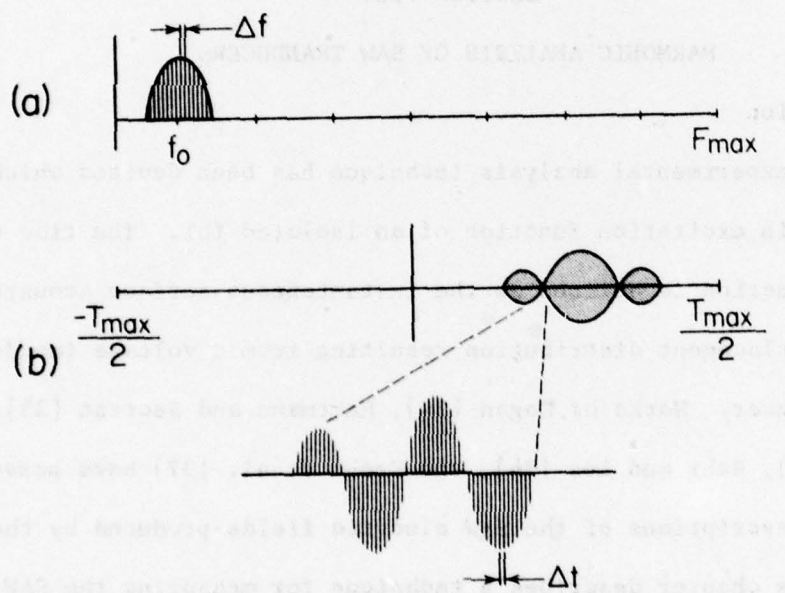


**Figure 38. Time frequency relationship**

- a) Frequency domain sampling
- b) Time domain sampling, increased time resolution

The digital Fourier transform is circular and

$$h(t)_{\text{calc}} = \sum_{i=1}^{\infty} h(t+T_{\max} \cdot i)_{\text{act}} \quad (73)$$

where  $\frac{-T_{\max}}{2} \leq t \leq \frac{T_{\max}}{2}$

produces an overlay of all time where  $h(t)_{\text{calc}}$  is the calculated impulse response and  $h(t)_{\text{act}}$  is the actual impulse response. If  $T_{\max}$  is chosen greater than the longest actual time delay component,  $h(t)_{\text{calc}}$  uniquely describes the entire impulse response without time domain aliasing.

The maximum frequency measured ( $F_{\max}$ ) establishes the separation between the samples ( $\Delta t$ ).

$$\Delta t = 1/F_{\max} \quad (74)$$

The total number of required measurement points is:

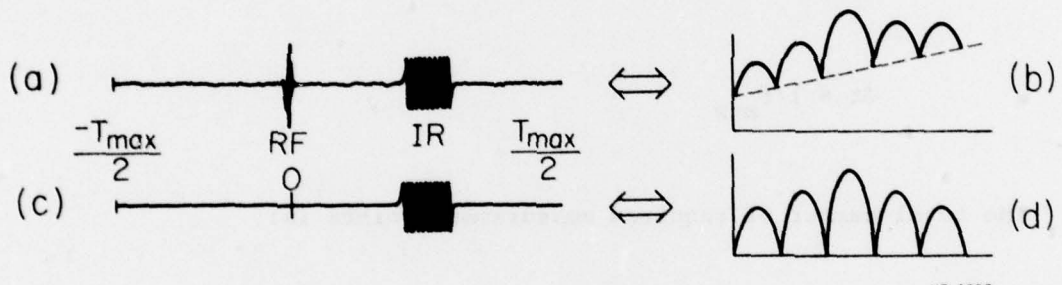
$$N = \frac{T_{\max}}{\Delta t} = \frac{F_{\max}}{\Delta f} = T_{\max} \cdot F_{\max} \quad (75)$$

### C. Segregation of Time Limited Responses

SAW delay line impulse responses like that shown in Figure 39a are made up of multiple time-limited signals that occupy individual non-overlying time regions. The direct RF coupling [ $h_{RF}(t)$ ] and the delay line impulse response, [ $h_{IR}(t)$ ] make up the complete transform of the measured transfer function  $H(\omega)$  shown in Figure 39b.

$$H(\omega) = \mathcal{F}[h_{RF}(t) + h_{IR}(t)] \quad (76)$$

The complete delay line impulse response is calculated by taking the inverse transform of the measured frequency response. The SAW impulse response is



KP-1290

Figure 39. Segregation of time limited responses

- a) Original time domain
- b) Original frequency domain
- c) SAW time components
- d) SAW frequency response

segregated by suppressing all time regions of the impulse response except for the transducer direct impulse response (Figure 39c). Transforming

back to the frequency domain produces the isolated SAW mode transfer function shown in Figure 39d. The number ( $N'$ ) of points used in this calculation is reduced to

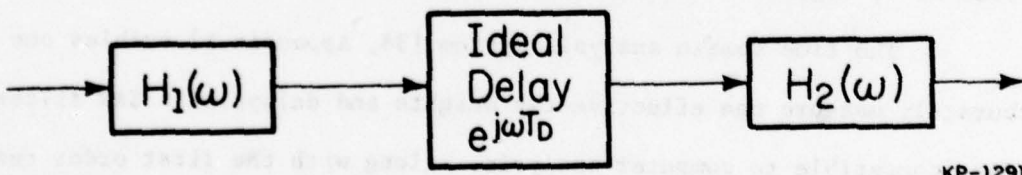
$$N' = F_{\max} \cdot T'_{\max} \quad (77)$$

where  $F_{\max}$  defines the original frequency range and  $T'_{\max}$  is the time duration of the non-suppressed impulse response.

Surface acoustic wave devices consist of two transducers operating in cascade (Figure 40). If the propagation is non-dispersive and diffraction free the transfer functions of individual transducers multiplied together produce the delay line transfer function

$$H(\omega) = H_1(\omega) \cdot H_2(\omega) \cdot e^{j\omega T_D} \quad (78)$$

where  $H_1(\omega)$  is the transfer function of the input transducer,  $H_2(\omega)$  is the transfer function of the output transducer, and  $T_D$  is the time delay. The delay is removed by taking the phase slope out of the measured frequency data.



KP-1291

Figure 40. Transfer function representation of SAW device.

The response of transducer #2 may be written as:

$$H_2(\omega) = \frac{H(\omega)}{H_1(\omega)} \quad (79)$$

To solve equation (79)  $H_1(\omega)$  must be known. In general neither  $H_1(\omega)$  nor  $H_2(\omega)$  is experimentally known, but for the case where the transducers are identical and unapodized, equation (79) reduces to the auto-deconvolution

$$H_2(\omega) = \sqrt{H(\omega)} \quad (80)$$

In the process of auto-convolution the frequency phase function is doubled and phase values of  $\pi$  become  $2\pi = 0$  and therefore cannot be recovered by the inverse process of auto-deconvolution. Additional phase information must be added for the auto-deconvolution to produce a unique single transducer response. [See Appendix A.]

#### D. Experimental Results

The device selected for harmonic analysis has two 15 wavelength aperture six double electrode transducers separated by approximately 100 wavelengths. These aluminum fingers are deposited on a 20 mil thick  $\text{LiNbO}_3$  substrate and have a stripe to space ratio .388. The back surface has been grooved at 45 degrees to scatter deep bulk waves.

The time domain analysis system [38, Appendix B] enables one to accurately measure the effective tap weights and delays of a SAW filter in a form compatible to computer analysis. Along with the first order response the tap weight and delay data takes into account all higher order transducers responses such as regenerations, reflections, diffraction and bulk modes.

The original frequency domain data (Figure 4la) has a considerable RF

coupling contribution (Figure 41b). The SAW mode is isolated by the suppression of all non-SAW time components (Figure 42a).

Assuming that the processes of generation and detection are identical, separation of the two identical unapodized transducer responses is performed by auto-deconvolution (equation 80). The previously mentioned phase ambiguity is removed by the introduction of a  $\pi$  phase shift where anticipated from the phase of a calculated single transducer harmonic response. This response is not the transform of a theoretical impulse response. In that case the magnitude of each harmonic would be equal, giving an inaccurate representation. Rather, the frequency response used for phase crossover determination is created by the addition of four  $\text{sinc}(\omega)$  functions centered at each harmonic and magnitude weighted by the experimental magnitude [ $H_2(\omega)$ ] at that harmonic (Figure 43). The phase of this composite response is subtracted from the phase of  $H(\omega)$  leaving the phase function of a single transducer. Relative phase offsets between harmonics are adjusted to the theoretical values determined by Hartmann and Secrest (Reference 35, Figure 39). Further work to resolve these phase ambiguities is required for the general case where the transducers are not identical and the relative weights of each transducer's harmonic response is not individually known.

Before Fourier transforming, the time resolution is expanded by appending zeroes to the frequency domain data. The result is the measured excitation function for a six double electrode unapodized IDT (Figure 44).

The impulse response of two double electrodes at the center of the transducer (Figure 45a,b) is compared with the theoretical time response predicted by Hartmann and Secrest (Figure 45b) and the time response predicted by Smith and Pedler (Figure 45c). Both theoretical responses are

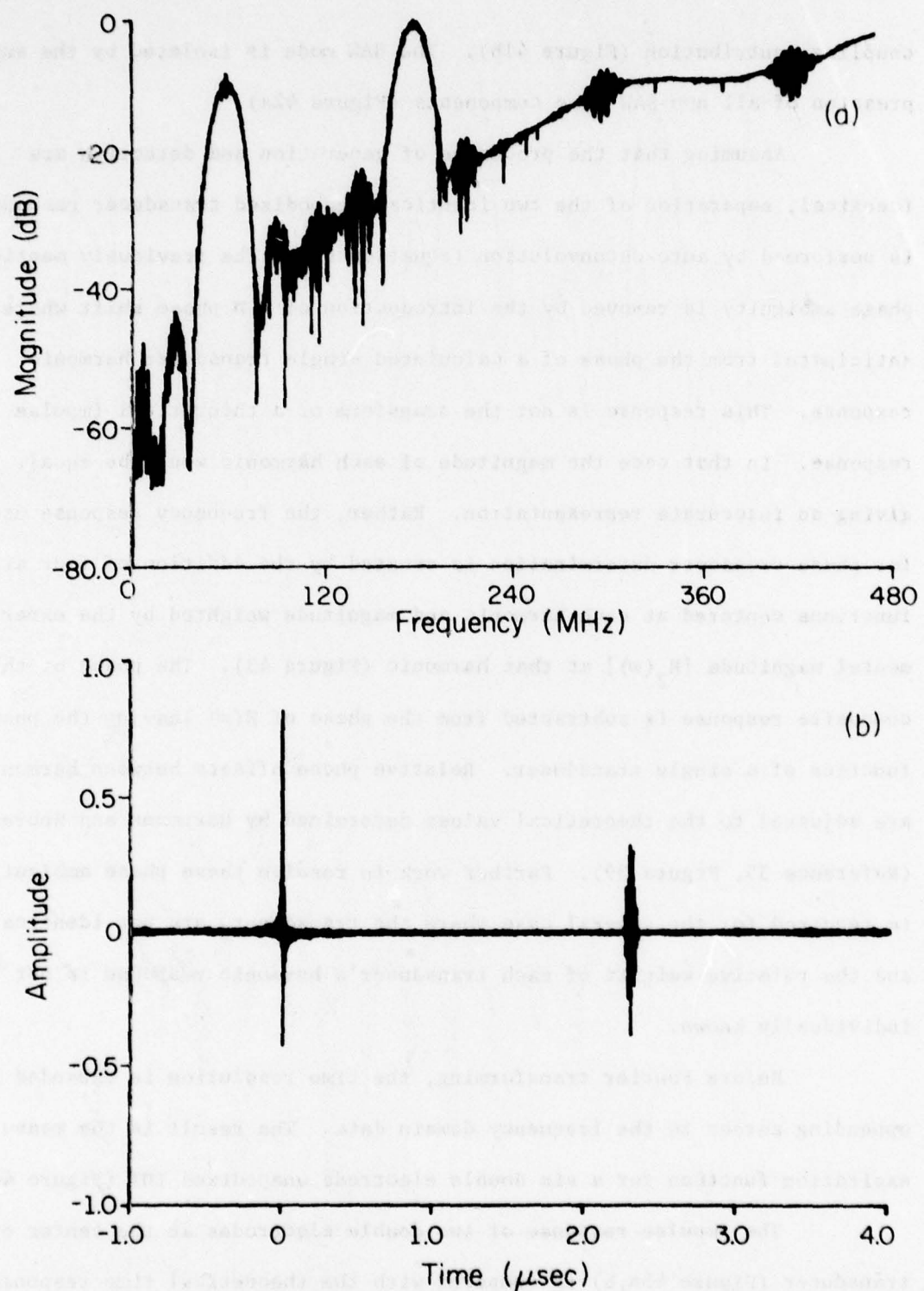


**Figure 41. Original measured harmonic data**  
**a) Frequency domain with RF coupling**  
**b) Impulse response**

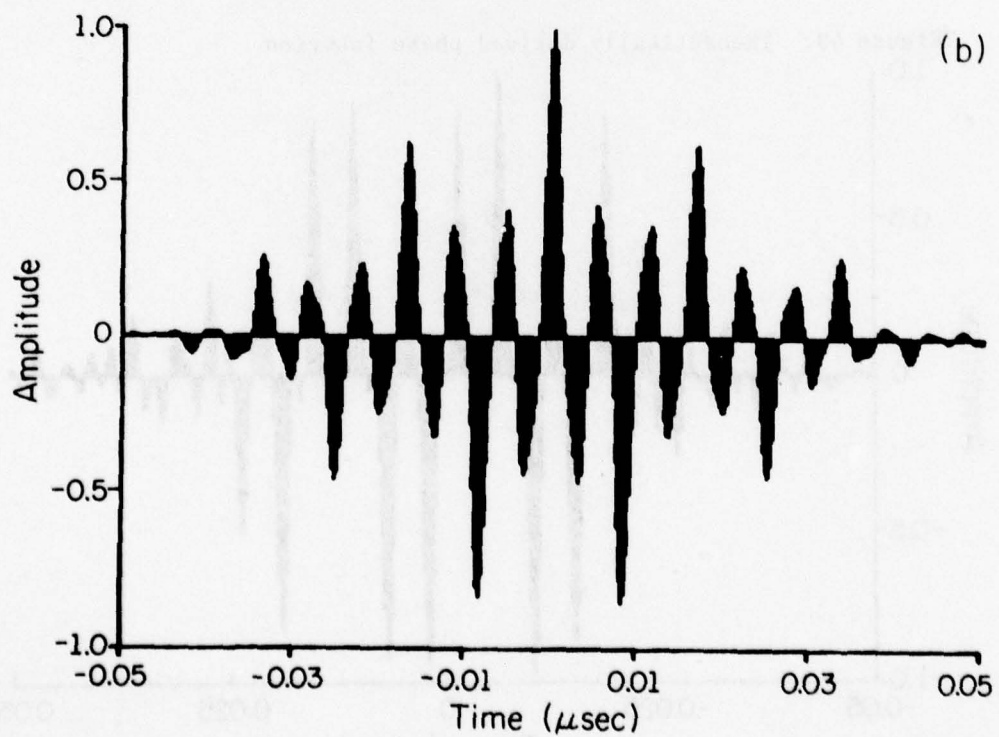
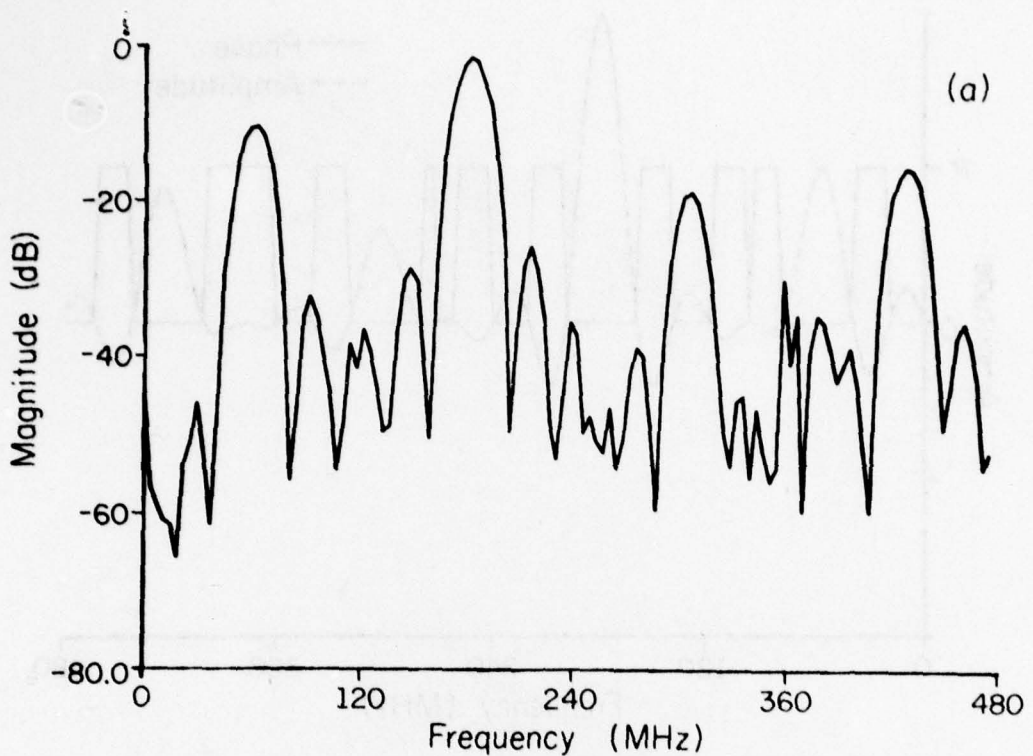


Figure 42. a) Frequency response after deletion of all non-SAW time components  
b) Expanded impulse response at  $t=0$

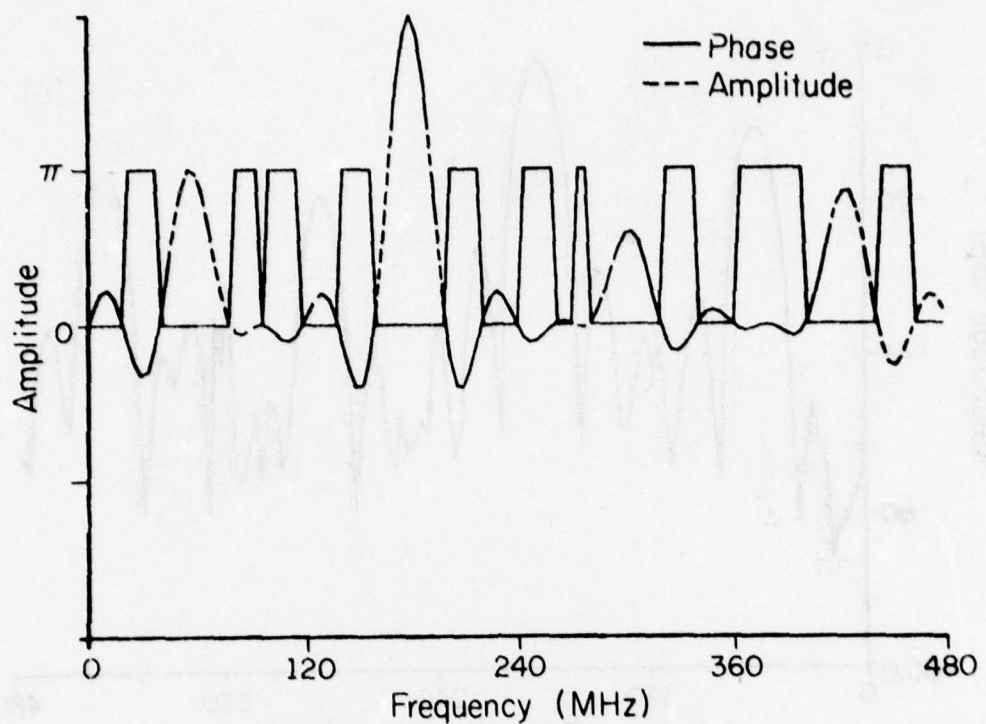


Figure 43. Theoretically derived phase function

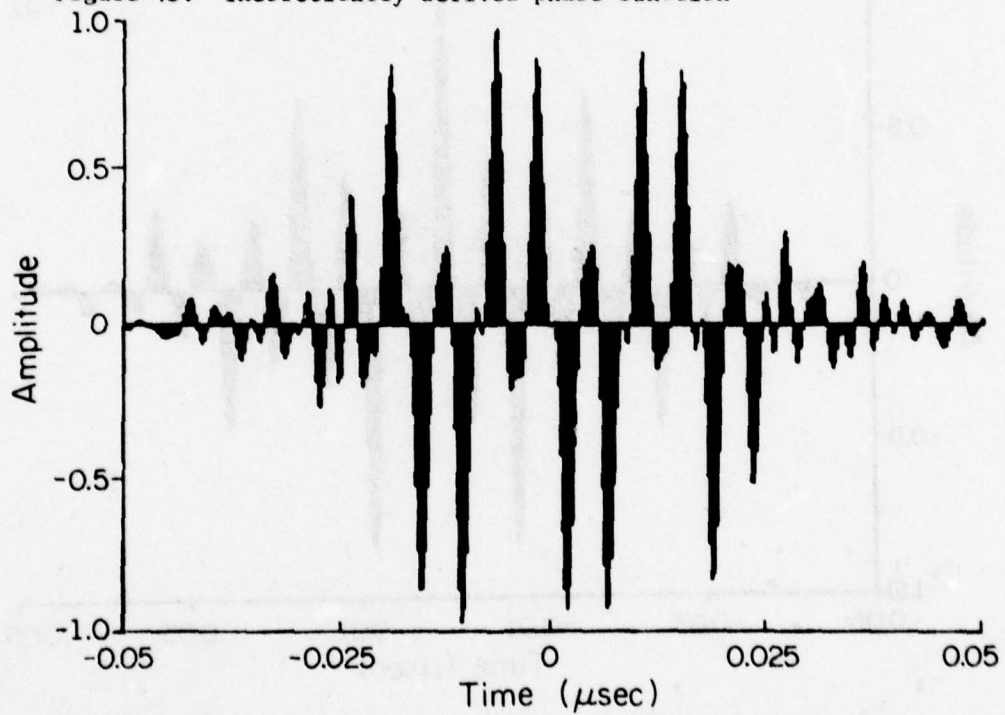
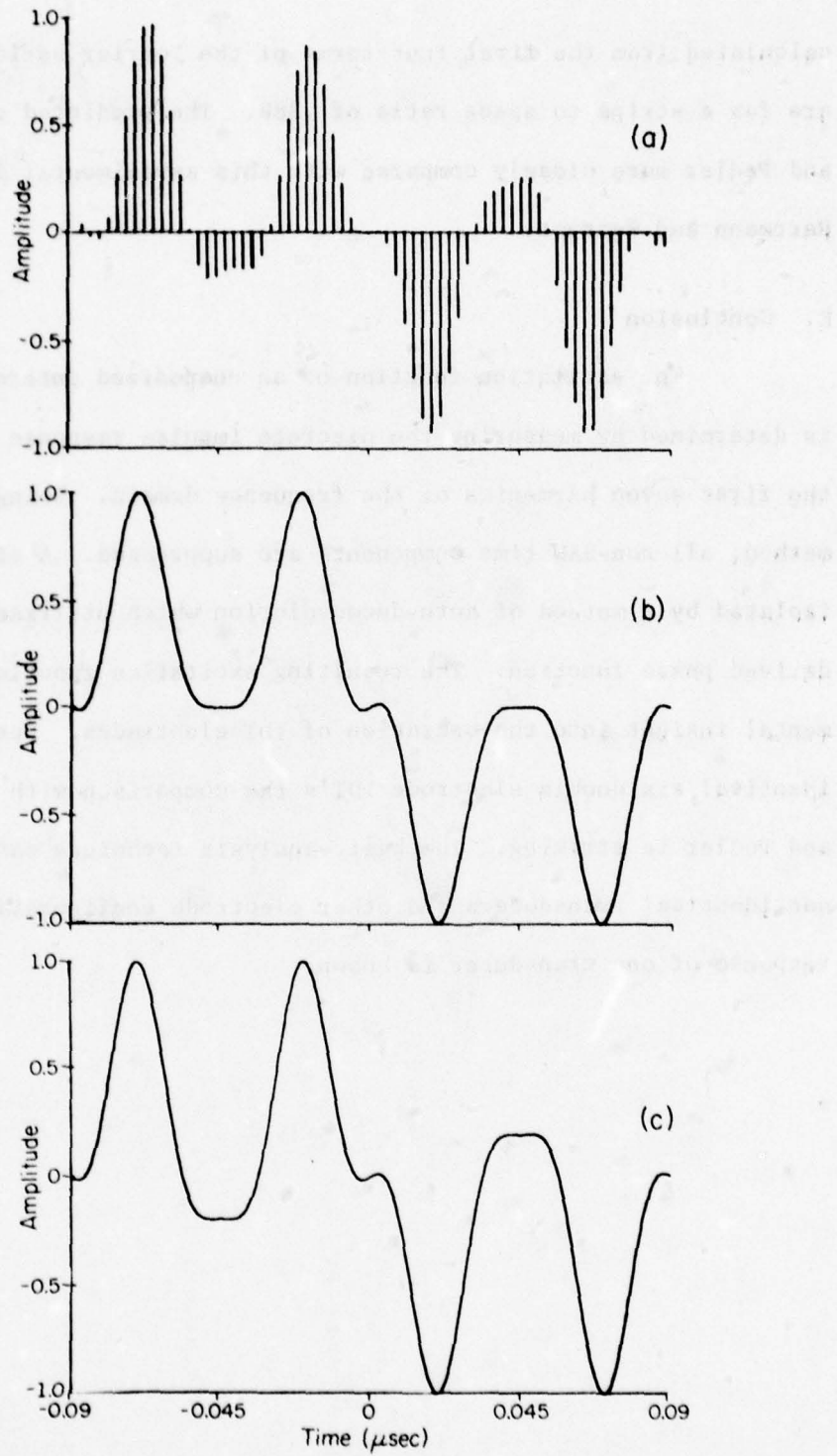


Figure 44. Experimentally calculated excitation function



**Figure 45. Comparison with four term Fourier series expansion**  
**a) Excitation function of two double electrodes**  
**b) Hartmann and Secrest**  
**c) Smith and Pedler**

calculated from the first four terms of the Fourier series expansion and are for a stripe to space ratio of .388. The predicted response of Smith and Pedler more closely compares with this experimental data than that of Hartmann and Secrest.

#### E. Conclusion

The excitation function of an unapodized interdigital transducer is determined by measuring the discrete impulse response taking into account the first seven harmonics of the frequency domain. Using a time segregation method, all non-SAW time components are suppressed. A single transducer is isolated by a method of auto-deconvolution which utilizes a theoretically derived phase function. The resulting excitation function provides experimental insight into the operation of IDT electrodes. For the case of two identical six double electrode IDT's the comparison with the theory of Smith and Pedler is striking. The basic analysis technique can be expanded to non-identical transducers and other electrode configurations once the phase response of one transducer is known.

## SECTION IX

### A GENERALIZED TRANSDUCER MODEL

#### A. Introduction

An important problem in surface wave technology is to determine the response of an interdigital transducer at fundamental and harmonic frequencies taking the effects of neighboring electrodes into account. The impulse response model assumes the electrodes to be point sources and provides the "array factor" by a simple Fourier transformation of the tap weights. This model is simple and useful but does not account for interactions with neighboring electrodes and does not provide information about the relative strengths of the harmonics.

An accurate characterization of the transducer is obtained by solving for the charge distribution under each electrode individually from field theory [41,42,43,44] taking neighboring electrode effects into account; this charge is then treated as a distributed source for the surface wave. A significant step in this direction is the work of Smith and Pedler [41] where the charge distribution on an electrode is tabulated as a set of polynomial coefficients for all possible combinations of neighboring electrode voltages of 0 and 1. In the general case when the voltages vary in analog manner this method is unwieldy and it is necessary to start from field theory for every new voltage sequence. The simplicity of the impulse response model is lost in this approach.

In a perfectly periodic array the charge distribution on each electrode is identical. The transducer response is then written as the product of the array factor from the impulse response model and the element factor which is the Fourier transform of the charge distribution on one electrode. In general, however, the charge distribution on each electrode is different because of neighboring electrode effects and a simple separation

of the transducer response into an element factor and an array factor is not possible.

This chapter shows that if the strips have uniform width and spacing throughout the array (without any missing electrodes) then the transducer response can be written as a product of an element factor and an array factor if the element factor is suitably defined. The sequence of voltages on the strips is completely arbitrary.

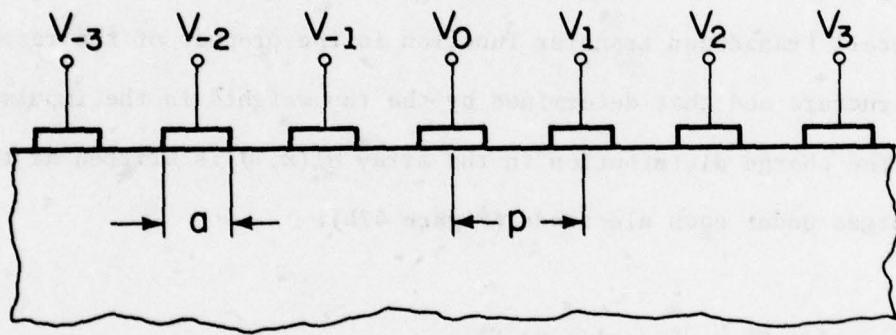
This formulation simplifies transducer design because the effect of neighboring electrodes on the transducer operation is equalized by dividing the specified response by the element factor when determining the tap weights.

This yields a considerable simplification, both conceptual and numerical, for transducers with electrodes that have arbitrary voltages but have uniform spacing and metallization ratio without any missing electrodes (Figure 46). This includes many practical weighting schemes such as withdrawal weighting with shorted electrodes, capacity weighting [45] and multiphase unidirectional transducers. Apodized transducers with shorted dummy electrodes are divided up into channels and treated as a number of uniform periodic transducers connected in parallel, each channel having a different voltage sequence. This approach, however, neglects the effect of the breaks in the fingers and the consequent transverse end effects.

In Section B, the capacitance and radiation conductance of different types of transducers are related to the "tap weights", providing an extension of the impulse response model that is valid at the harmonics and takes neighboring electrode effects into account. In Section C, the theory is applied to some special cases and shown to agree with published results.

## B. Theory

A periodic array of electrodes (Figure 46) is considered with a constant metallization ratio  $\eta = a/p$ , a fixed period  $p$  and an arbitrary sequence of voltages. In a direct coupled transducer the strips are connected directly to either of two busbars while in the capacity-coupled transducer each electrode is connected through a capacitive voltage divider. An apodized transducer is conceptually divided up into channels and considered as a number of direct coupled unapodized transducers connected electrically in parallel. It is the purpose of this section to develop a generalized expression for the capacitance and radiation conductance of the array in terms of the voltage connection sequence for each of these different types of transducers.



KP-1528

Figure 46. Periodic array transducer

In Part 1 of this section the Basic Charge Distribution Function (BCDF) of the array is defined and evaluated using the tables in Reference

[46]. This function is characteristic of the array and depends only on the metallization ratio  $\eta$ ; the period  $p$  only scales the function. In Part 2 it is shown that the charge distribution in the array for any voltage sequence is the convolution product of the BCDF and the voltage sequence. The Fourier transform of the BCDF thus plays the role of an "element factor" which is determined once and for all for different values of  $\eta$ . It is used with the impulse response model to provide the complete transducer response for any arbitrary voltage sequence. In Part 3, the charge distribution in the array is used to derive the conductance and capacitance for each of the three types of transducers described above.

### 1. Basic Charge Distribution Function

A periodic array with a metallization ratio  $\eta$  is considered with all the strips grounded except for the central one which is at a potential of 1V (Figure 47a). This is defined as a single tap structure, because the overall transducer transfer function is the product of the response of this structure and that determined by the tap weights in the impulse response mode. The charge distribution in the array  $\sigma'_G(x, \eta)$  is written as the sum of the charges under each electrode (Figure 47b):

$$\sigma'_G(x, \eta) = \sum_{n=-\infty}^{\infty} \sigma'_n(x-np, \eta) \quad (81a)$$

where  $\sigma'_n(x, \eta)$  is the charge distribution under the  $n^{\text{th}}$  electrode from the center.  $\sigma'_G(x, \eta)$  is referred to as the Basic Charge Distribution Function (BCDF).

The Fourier transform of equation (80a) yields the relation

$$\bar{\sigma}'_G(k, \eta) = \sum_{n=-\infty}^{\infty} \bar{\sigma}'_n(k, \eta) e^{-jkn p} \quad (81b)$$

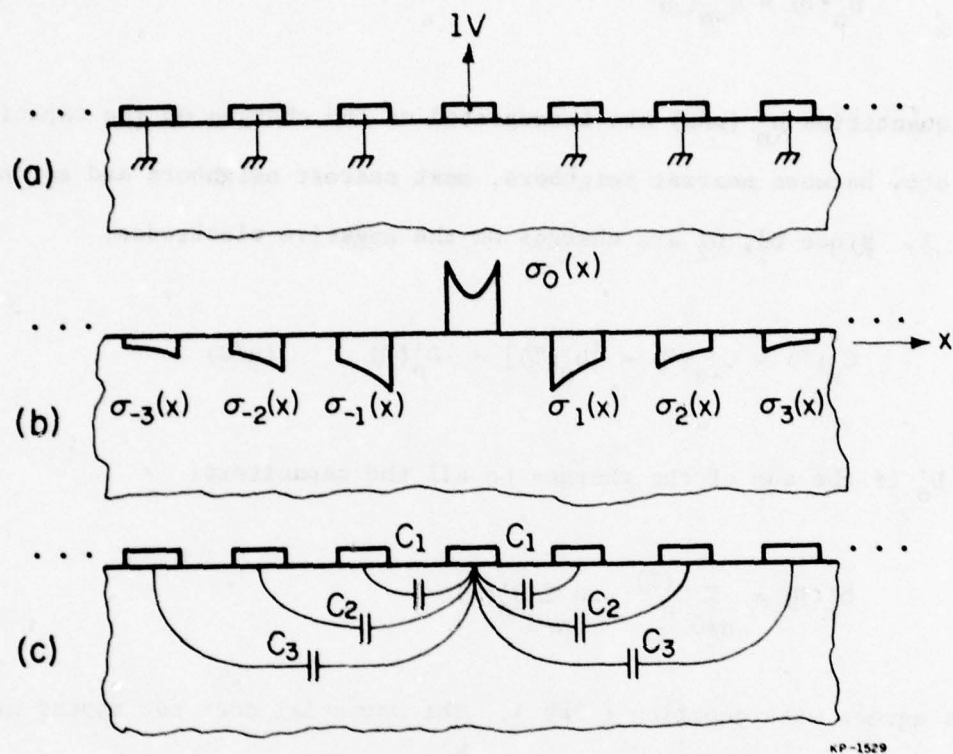


**Figure 47.** Basic Charge Distribution Function in a single tap structure.

where the bar denotes the Fourier transform of the corresponding spatial functions. The total charge under the  $n^{\text{th}}$  electrode is given by,

$$D'_n(\tau) = \bar{\sigma}'_n(k=0, \tau) \quad (82a)$$

Since the total charge under all the electrodes must be zero,

$$\sum_{n=-\infty}^{\infty} D'_n(\tau) = \bar{\sigma}'_G(k=0, \tau) = 0 \quad (82b)$$

Also from the symmetry of the array

$$D'_n(\tau) = D'_{-n}(\tau) \quad (82c)$$

The quantities  $D'_n$  ( $n \neq 0$ ) are interpreted as the charges on the capacitors  $C_1$ ,  $C_2$ , etc. between nearest neighbors, next nearest neighbors and so on (Figure 47c). Since  $D'_1$ ,  $D'_2$  are charges on the negative electrodes,

$$C_n(\tau) = C_{-n}(\tau) = |D'_n(\tau)| = -D'_n(\tau) \quad (n \neq 0) \quad (82d)$$

and  $D'_0$  is the sum of the charges on all the capacitors:

$$D'_0(\tau) = \sum_{n \neq 0} C_n(\tau) = - \sum_{n \neq 0} D'_n(\tau)$$

This agrees with equation (82b). The potential does not appear explicitly in equation (82d) since it is assumed to be 1V.

Theoretically the summation in equation (81b) extends from  $-\infty$  to  $+\infty$ . However, electrodes beyond the next nearest neighbor have negligible effect [41]. So  $\sigma'_n$  is assumed to be zero for  $|n| > 2$ :

$$\bar{\sigma}'_G(k, \tau) = \sum_{n=-2}^2 \bar{\sigma}'_n(k, \tau) e^{-jkn\tau} \quad (83)$$

The equations derived in this chapter are, however, perfectly general and can be extended to take more terms in the summation into account.

The functions  $\bar{\sigma}'_n(k, \tau)$  are determined using the appropriate tables in Reference[41]. Using equation (83),  $\bar{\sigma}'_G(k, \tau)$  is evaluated for different values of the metallization ratio  $\tau$ .  $D'_0(\tau)$ ,  $D'_1(\tau)$  and  $D'_2(\tau)$  are determined from equation (82a).

Figure 48 shows the normalized charges  $\bar{\sigma}_G(k, \eta)$ ,  $D_1(\eta)$ ,  $D_2(\eta)$ :

$$\bar{\sigma}_G(k, \eta) = \frac{\bar{\sigma}_G'(k, \eta)}{\bar{\sigma}_G'(k=k_0, \eta=0.5)} \quad (84a)$$

$$D_n(\eta) = \frac{D_n'(\eta)}{-2D_1'(\eta=0.5)} \quad (84b)$$

where  $k_0$  is the surface wave wavenumber at which the strip period is half a wavelength. The corresponding frequency is called the synchronous frequency and denoted by  $f_0$ :

$$k_0 = \pi/p$$

$$f_0 = \frac{v_s}{2p}$$

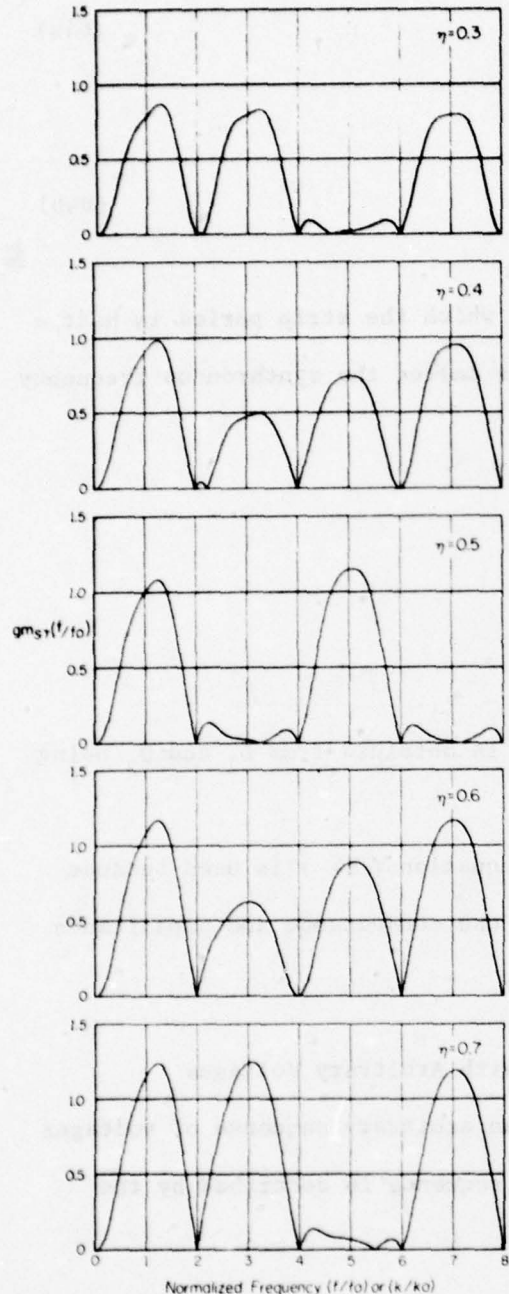
where  $v_s$  is the surface wave velocity.  $D_0$  is obtained from  $D_1$  and  $D_2$  using equation (82b).

The particular normalization in equation (84) is used because it yields simple recognizable constants in the conductance and capacitance expressions.

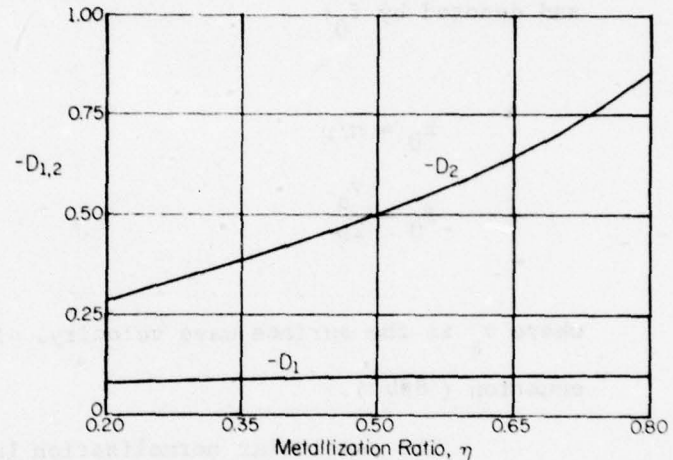
## 2. Charge Distribution in Periodic Array with Arbitrary Voltages

A spatially periodic array with an arbitrary sequence of voltages is considered (Figure 49a). The voltage sequence is described by the voltage function  $V(x)$ :

$$V(x) = \sum_{n=-\infty}^{\infty} V_n \delta(x-np)$$



(a)

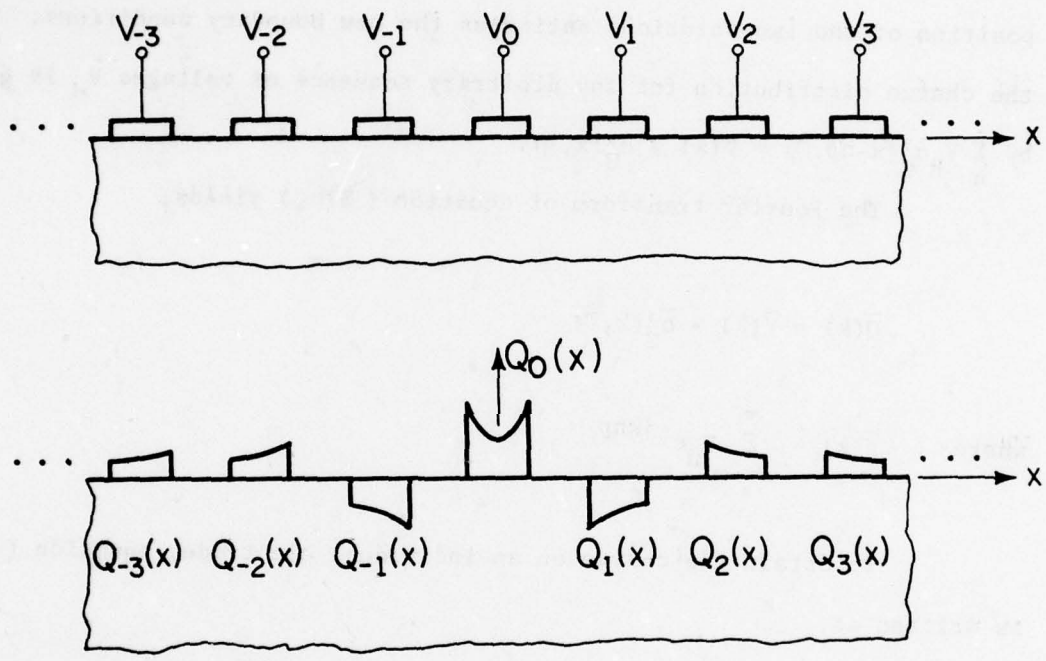


(b)

Figure 48. Element factor parameters  
 a) element factor response  
 b) element factor D function

where  $V_n$  is the voltage on the  $n^{\text{th}}$  electrode. The charge distribution in the array  $Q(x)$  is written as a sum of the charges under each electrode (Figure 49b):

$$Q(x) = \sum_{n=-\infty}^{\infty} Q_n(x-np) \quad (86)$$



KP-1530

Figure 49. Charge distribution in a periodic array with arbitrary voltage sequences

It is shown from an application of the superposition principle that  $Q(x)$  is the convolution product of the voltage function and the BCDF:

$$Q(x) = V(x) * \sigma'_G(x, \eta) \quad (87a)$$

This can be seen as follows. Consider the voltage sequence shown in Figure 50a . The charge distribution for this sequence is  $V_0 \sigma'_G(x, \tau)$ . Similarly for the voltage sequence in Figure 50b , the charge distribution is  $V_1 \sigma'_G(x-p, \tau)$ . Now, for the sequence in Figure 50c the charge distribution is the superposition of the two previous distributions, i.e.,  $V_0 \sigma'_G(x, \tau) + V_1 \sigma'_G(x-p, \tau)$ . This is because the field equations are linear and superposition of the two solutions satisfies the new boundary conditions. Thus the charge distribution for any arbitrary sequence of voltages  $V_n$  is given by  $\sum_n V_n \sigma'_G(x-np, \tau) = V(x) * \sigma'_G(x, \tau)$ .

The Fourier transform of equation ( 87b ) yields,

$$\bar{Q}(k) = \bar{V}(k) * \bar{\sigma}'_G(k, \tau) \quad (87b)$$

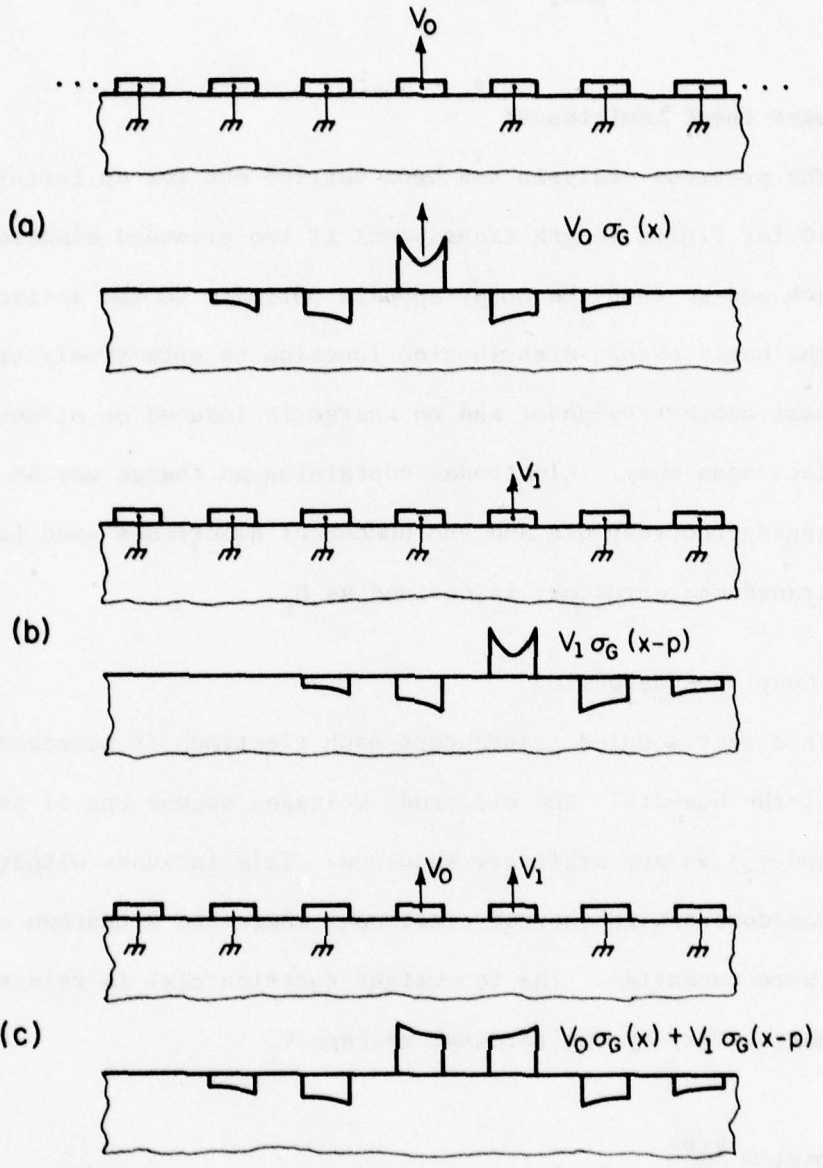
where  $\bar{V}(k) = \sum_{n=-\infty}^{\infty} V_n e^{-jkn}$

To obtain the charge on an individual electrode, equation ( 57a ) is written as,

$$\begin{aligned} Q(x) &= \sum_{n=-\infty}^{\infty} V_n \delta(x-np) * \sum_{n=-2}^2 \sigma'_n(x-np, \tau) \\ &= \sum_{n=-\infty}^{\infty} * \sum_{m=-2}^2 V_{n-m} \sigma'_{m-n}(x-np, \tau) \end{aligned} \quad (88)$$

The summation over  $m$  runs only from -2 to +2 because  $\sigma_m$  is assumed zero for  $|m| > 2$  as discussed in Part 1 of this section. Comparing equations ( 88 ) and ( 86 ),

$$Q_n(x) = \sum_{m=-2}^2 V_{n-m} \sigma'_{m-n}(x, \tau) \quad (89)$$



KP-1531

Figure 50. Charge distribution in a periodic array as a superposition of basic charge distribution functions

The total charge on the  $n^{\text{th}}$  electrode is thus givey by,

$$q_n = \bar{Q}_n(k=0) = \sum_{m=-2}^2 V_{n-m} D_m'(\tau) \quad (90)$$

### 3. Transducer Input Admittances

The previous analysis has been carried out for an infinite array but is valid for finite length transducers if two grounded electrodes are added at each end so that the array appears periodic to the active electrodes.

The basic charge distribution function is effectively truncated after the next nearest neighbor and no charge is induced on elements farther than two electrodes away. Electrodes containing no charge may be removed without changing the response and the number of electrodes used in the truncated transducer structure is defined as  $N_E$ .

#### a. Direct Coupled, Unapodized

In direct-coupled transducers each electrode is connected directly to either of the busbars. The electrode voltages assume one of two possible values (0 and  $V_T$ ) in any arbitrary sequence. This includes withdrawal weighted transducers with shorted electrodes where the withdrawn electrodes are set at zero potential. The tap weight function  $\alpha(x)$  is related to the voltage function  $V(x)$  by the terminal voltage  $V_T$

$$\begin{aligned} \alpha(x) &= \frac{V(x)}{V_T} \\ &= \sum_{n=1}^{N_E} \frac{V_N}{V_T} \delta(x-np) \end{aligned} \quad (91a)$$

The Fourier transform of  $\alpha(x)$  is denoted by  $\bar{\alpha}(k)$ .

$$\begin{aligned}\bar{\alpha}(k) &= \sum_{n=1}^{N_E} \frac{v_n}{v_T} e^{-jknp} \\ &= \sum_{n=1}^{N_E} \alpha_n e^{-jknp}\end{aligned}\quad (91b)$$

The radiation conductance is proportional to the squared magnitude of  $\bar{Q}(k)$  at the surface wave wavenumber. From equation (87b),

$$\begin{aligned}G_a(f) &= G_s \cdot |\bar{\sigma}_G(k, \eta)|^2 \cdot \frac{|\bar{v}(k)|^2}{v_T^2} \\ &= G_s \cdot |\bar{\sigma}_G(k, \eta)|^2 \cdot |\bar{\alpha}(k)|^2\end{aligned}\quad (92a)$$

where, (1)  $k = 2\pi f/v_s$ ,  
 (2)  $v_s$  is the surface-wave velocity,  
 and (3)  $G_s$  is a constant.

The constant  $G_s$  is shown to be the synchronous frequency radiation conductance per electrode pair of interdigital array with alternating polarities and with  $\eta = .5$ :

$$G_s = 8K^2 f_o C_s \quad (92b)$$

where, (1)  $K^2$  is the electromechanical coupling constant  
 and (2)  $C_s$  is the capacitance of a pair of electrodes in the inter-digital array with alternating polarities and with  $\eta = .5$ .

$$C_s = (\epsilon_p + \epsilon_o) \cdot W \quad (92c)$$

where  $\epsilon_p$  is the effective substrate permittivity,  $\epsilon_0$  is the vacuum permittivity and  $W$  is the transducer width.

In equation ( 92a ),  $\bar{\alpha}(k)$ , which is the Fourier transform of the tap weights, represents the array factor of the impulse response model while  $\bar{\sigma}_G(k,\eta)$  plays the role of the element factor.

The total positive charge on the electrodes is written as,

$$Q_P = \sum_{n=1}^{N_E} \frac{V_n}{V_T} \cdot q_n \quad (93)$$

The summation in equation ( 93 ) automatically ignores the negative charges on the grounded electrodes. From equations ( 90 ) and ( 93 ), the capacitance of the array is obtained:

$$\begin{aligned} C &= \frac{Q_P}{V_T} \\ &= C_s \cdot \sum_{m=-2}^2 D_m(\eta) \sum_{n=1}^{N_E} \frac{V_n \cdot V_{n-m}}{V_T^2} \\ &= C_s \sum_{m=-2}^2 D_m(\eta) \sum_{n=1}^{N_E} \alpha_n \cdot \alpha_{n-m} \end{aligned} \quad (94)$$

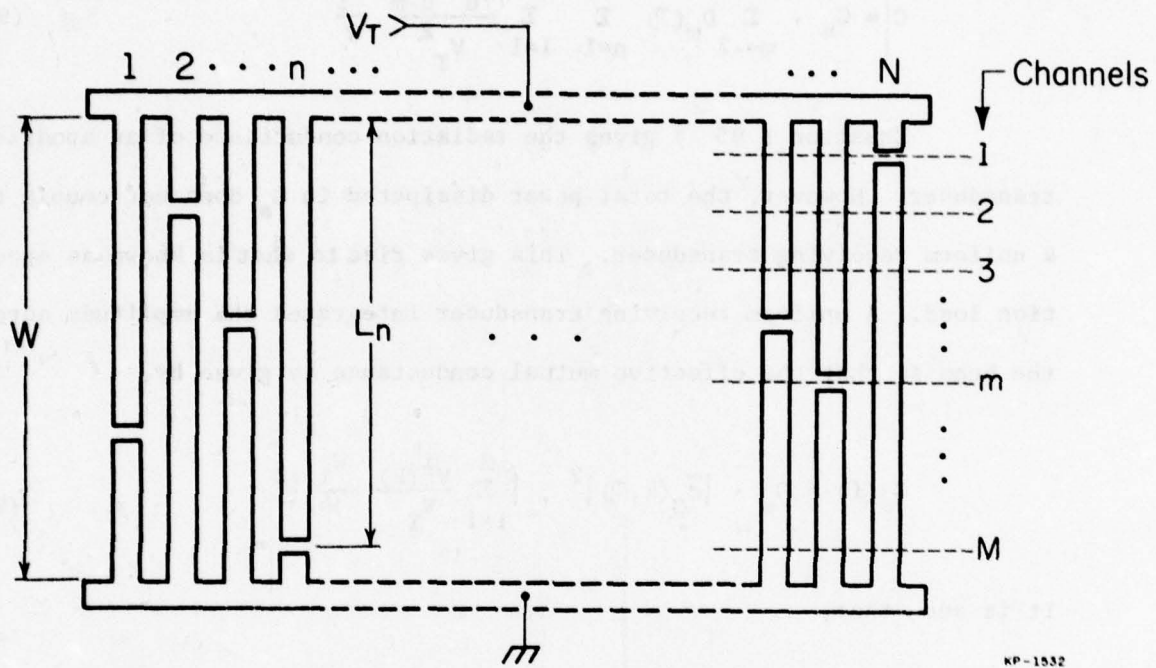
The constant  $C_s$  appears in equation ( 94 ) because the  $D_n$ 's are normalized.

#### b. Direct Coupled, Apodized

In an apodized transducer with shorted dummy electrodes the tap weight of the  $n^{\text{th}}$  electrode,  $\alpha_n$  is defined as the length of the electrode connected to the busbar with potential  $V_T$ , divided by the width of the transducer (Figure 51 ).

$$\alpha_n = \frac{L_n}{W}$$

(95a)



KP-1532

Figure 51. Apodized transducer with shorted dummy electrodes

The tap weight function  $\alpha(x)$  is defined as,

$$\alpha(x) = \sum_{n=1}^{N_E} \alpha_n \delta(x-np) \quad (95b)$$

The apodized transducer is divided up into  $M$  channels and considered as  $M$  direct coupled transducers in parallel. The total beam is divided into enough channels so that each electrode ends at the edge of a channel. Each channel has a different voltage sequence which is indicated by a superscript. Equations (92a) and (94) are modified to include the summation over the different channels:

$$G_a(f) = G_s \cdot |\bar{\sigma}_G(k, \eta)|^2 \cdot \sum_{i=1}^M \frac{|V^i(k)|^2}{V_T^2} \frac{W_i}{W} \quad (96a)$$

$$C = C_s \cdot \sum_{m=-2}^2 D_m(\eta) \sum_{n=1}^{N_E} \sum_{i=1}^M \frac{V_n^i V_{n-m}^i}{V_T^2} \frac{W_i}{W} \quad (96b)$$

Equation ( 95 ) gives the radiation conductance of an apodized transducer. However, the total power dissipated in  $G_a$  does not couple to a uniform receiving transducer. This gives rise to what is known as apodization loss. A uniform receiving transducer integrates the amplitude across the beam so that the effective mutual conductance is given by,

$$G_m(f) = G_s \cdot |\bar{\sigma}_G(k, \eta)|^2 \cdot \left| \sum_{i=1}^M \frac{V^i(k)}{V_T} \frac{W_i}{W} \right|^2 \quad (97a)$$

It is seen that,

$$\sum_{i=1}^M \frac{V^i(x)}{V_T} = \frac{W_i}{W} = \alpha(x)$$

It follows that,

$$\sum_{i=1}^M \frac{V^i(k)}{V_T} = \frac{W_i}{W} = \bar{\alpha}(k)$$

Equation ( 97a ) is thus written as,

$$G_m(f) = G_s \cdot |\bar{\sigma}_G(k, \eta)|^2 \cdot |\bar{\alpha}(k)|^2 \quad (97b)$$

Once again the array factor and the element factor are evident.

The apodization loss is given by,

$$\text{Apodization Loss} = 10 \log \frac{G_m(f)}{G_a(f)}$$
$$= 10 \log \frac{\left| \sum_{i=1}^M \bar{v}^i(k) \right|^2}{\sum_{i=1}^M |\bar{v}^i(k)|^2} \quad (98)$$

The expressions 14, 15 and 16 give the radiation conductance, the mutual conductance, the apodization loss and the capacitance for any arbitrary sequence of tap weights. Equation ( 97b ) shows that the mutual conductance is equal to that derived from the impulse response model multiplied by the single tap response  $|\bar{\sigma}_G(k, \eta)|^2$  for the appropriate metallization ratio,  $\eta$ . If the tap weights alternate in polarity with a slowly varying apodization, then (neglecting  $D_2$  and  $D_{-2}$ ) equation ( 96b ) reduces to the usual result for the capacitance of apodized transducers.

These expressions are also valid in the more general case of over sampling [ 46 ] where several adjacent electrodes have the same polarity. It is quite surprising that even in this case the transfer function is proportional to the Fourier transform of the tap weights defined by equation ( 95 ).

This analysis neglects the excitation in the gaps, the transverse end effects, and diffraction; however, all nearest neighbor interactions are accounted for as long as two grounded electrodes are attached to each end of the transducer. The analysis is also valid for harmonic operation.

This significantly simplifies filter syntheses in that the nearest neighbor interactions are compensated for automatically in a one step

deconvolution of the specified response by the single tap filter function. After the deconvolution, the design procedure proceeds directly as in the case of the impulse response model using the deconvolved specified response as the reference.

### c. Capacity-Coupled, Unapodized

In a capacity-coupled transducer each electrode is connected to the busbars through a capacitive voltage divider consisting of capacitors  $C_{An}$  and  $C_{Bn}$  at the  $n^{\text{th}}$  electrode such that (Figure 52a) [ 45 ]

$$C_{An} + C_{Bn} = C_T = \text{constant} \quad (99a)$$

$$\frac{C_{An}}{C_T} = \alpha_n \quad (99b)$$

where  $\alpha_n$  is the tap-weight of the  $n^{\text{th}}$  electrode.

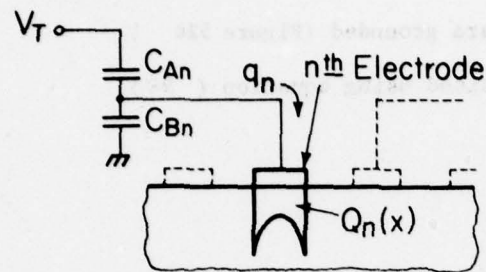
The capacitive network is replaced by its Thevenin equivalent to yield the circuit of Figure 52b . The problem is to determine the voltages  $V_n$  on the electrodes from the tap weights  $\alpha_n$ . It follows from the principle of superposition (using an argument similar to that used in Section B-2 to derive equation ( 87a ) that,

$$V(x) = (\alpha(x) * \phi(x)) * V_T \quad (100)$$

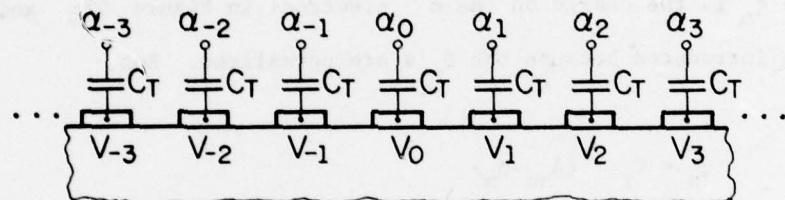
where, (1)  $V(x) = \sum_n V_n \delta(x-np)$

$$\alpha(x) = \sum_n \alpha_n \delta(n-p)$$

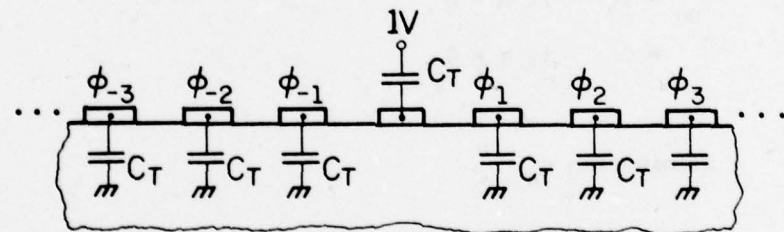
$$\phi(x) = \sum_n \phi_n \delta(x-np)$$



(a) Single Electrode and Coupling Network



(b) Thevenin's Equivalent



(c) Single Tap Voltage Distribution

KP-1535

**Figure 52. Capacity weighted transducer**  
 a) single electrode and coupling network  
 b) Thevenin's equivalent  
 c) single tap voltage distribution

$V(x)$  is the electrode voltage function while  $\alpha(x)$  is the tap-weight function.

(2)  $\phi_n$  is the sequence of voltages that appears on the electrodes when  $IV$  is applied to the central electrode and the other electrodes are grounded (Figure 52c )

The  $\phi_n$ 's are obtained using equation ( 90 ):

$$q_n = C_s \sum_m \phi_{n-m} D_m$$

$$= C_s \sum_m \phi_m D_{n-m}$$

where  $q_n$  is the charge on the  $n^{\text{th}}$  electrode in Figure 52c and the factor  $C_s$  is introduced because the  $D_n$ 's are normalized. But,

$$q_n = C_T \cdot (\delta_{no} - \phi_n)$$

$$\begin{aligned} \text{where, } \delta_{no} &= 1 && \text{if } n = 0 \\ &= 0 && \text{if } n \neq 0 \end{aligned}$$

Eliminating  $q_n$ ,

$$\sum_m (D_{n-m}(\pi) \frac{C_s}{C_T} + \delta_{nm}) \phi_m = \delta_{no} \quad (101)$$

Equation ( 101 ) represents a matrix equation that is solved for a given  $C_T$  to yield the  $\phi_n$ 's and hence the function  $\phi(x)$  in equation ( 100 ). Depending on the ratio  $C_s/C_T$ ,  $\phi_n$  is truncated at some value of  $|n|$ .

Equations ( 100 ) and ( 87a ) are combined to yield the charge distribution in the capacity coupled transducer:

$$Q(x) = \sigma'_G(x, T) * \phi(x) * \alpha(x) * V_T \quad (102)$$

From the Fourier transform of equation ( 102 ) the radiation conductance is written as,

$$G_a(f) = G_s \cdot |\bar{\sigma}_G(k, T)|^2 \cdot |\bar{\phi}(k)|^2 \cdot |\bar{\alpha}(k)|^2 \quad (103)$$

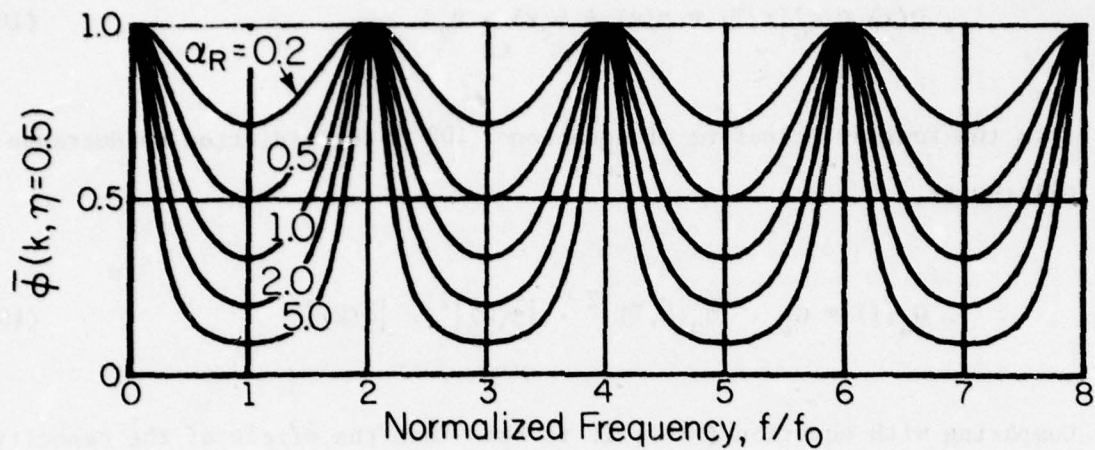
Comparing with equation ( 91 ) it is seen that the effect of the capacitive coupling is to multiply the element factor  $\bar{\sigma}_G(k)$  by  $\bar{\phi}(k)$  in the expression for conductance. The capacitive coupling spectral response  $\bar{\sigma}_G(k)$  has been plotted for typical values of  $\alpha_r$  with the metalization ratio equal to 0.5 in Figure 53 . It will be noted that if  $C_T$  is infinitely large corresponding to the direct-coupled case,  $\phi(x) = \delta(x)$  so that  $\bar{\phi}(k) = 1$  and equation ( 102 ) reduces to equation ( 91 ).

To obtain the charge on an individual electrode equation ( 101 ) is written as,

$$Q(x) = \sum_{n=-2}^{+2} \sigma'_n(x-np, T) * \sum_{n=-\infty}^{\infty} \phi_n \delta(x-np) * \sum_{n=1}^{N_E} \alpha_n \delta(x-np)$$

$$= \sum_{n=1}^{N_E} \sum_{m=-2}^{2} \alpha_{n-m} \sum_{i=-2}^{+2} \phi_{m-i} \sigma'_i(x-np, T)$$

clearly the charge distribution on the  $n^{\text{th}}$  electrode is,



KP-1534

Figure 53. Spectral response due to capacitive couplers

$$Q_n(x) = \sum_{m=-2}^2 \alpha_{n-m} \sum_{i=-2}^{+2} \phi_{m-i} \sigma'_i(x, \eta)$$

The total charge on the  $n^{\text{th}}$  electrode is, therefore,

$$q_n = \sum_{m=-2}^2 \alpha_{n-m} \sum_{i=-2}^{+2} \phi_{m-i} D'_i(\eta)$$

Comparing with equation ( 90 ), it is seen that the effect of capacitive coupling is to replace  $D_m$  with  $\sum_i \phi_{m-i} D_i$  in the expression for the total charge on an individual electrode.

To obtain the capacitance it is necessary to find the total charge drawn from the positive busbar. This is obtained from Figure 52a as,

$$Q_p = \sum_n \{ C_T \alpha_n (1 - \alpha_n) + \alpha_n q_n \}$$

The capacitance is thus written as,

$$C = C_T \sum_{n=1}^{N_E} \alpha_n (1 - \alpha_n) + C_s \cdot \left( \sum_{n=1}^{N_E} \sum_{m=-2}^2 \alpha_n \alpha_{n-m} \sum_i \phi_{m-i} D_i(\tau) \right) \quad (104)$$

The equations ( 103 ) and ( 104 ) express the radiation conductance and capacitance for any arbitrary tap weight sequence. It is seen that conductance equals that determined by the impulse response model multiplied by the single tap response  $|\bar{\phi}(k, \tau)|^2 \cdot |\bar{\sigma}_a(k, \tau)|^2$ . The general capacitance expression also reduces to the result in Reference 45 in the special case of alternating polarity taps with slowly varying strengths.

These expressions are also valid in the more general case of oversampling where several adjacent electrodes have the same polarity. The response is still directly related to the Fourier transform of the tap weights. This was found experimentally [ 46 ].

This analysis neglects diffraction and transverse end affects which represents only a minor degradation because the beam width is constant. All nearest neighbor interactions including loading of the coupling capacitors by adjacent taps are taken into account.

Filter synthesis again is simplified in that all nearest neighbor effects are compensated for by a deconvolution of the specified response by the single tap filter function when specifying tap weights. This analysis is valid for all harmonics.

### C. Evaluation of Special Cases

In this section the conductance and capacitance of three types of direct-coupled transducer structures are evaluated and shown to agree with published results.

First, the conductance at fundamental center frequency and the capacitance are evaluated for the three types of electrode connections shown in Figure 54. The radiation conductance is then evaluated at the harmonics and compared with experimental result. Each transducer is assumed to be N electrical periods long. Two additional grounded electrodes are added at each end. This makes the array look perfectly periodic to the active electrodes and the theory is exactly valid.

#### 1. Two Electrodes per Period (Figure 54a)

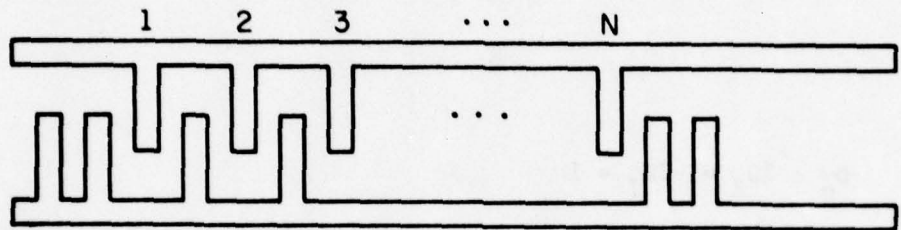
In a single electrode transducer (two electrodes per period) the fundamental center frequency,  $f_c$  is equal to the synchronous frequency  $f_o$ . The radiation conductance at  $f_c$  is given by,

$$\begin{aligned} G_a(f_c) &= G_s(f_o) \cdot |\bar{\sigma}_G(k=k_o, T=0.5)|^2 \cdot |\bar{V}(k=k_o)|^2 \\ &= G_s(f_o) \cdot N^2 \end{aligned} \quad (105)$$

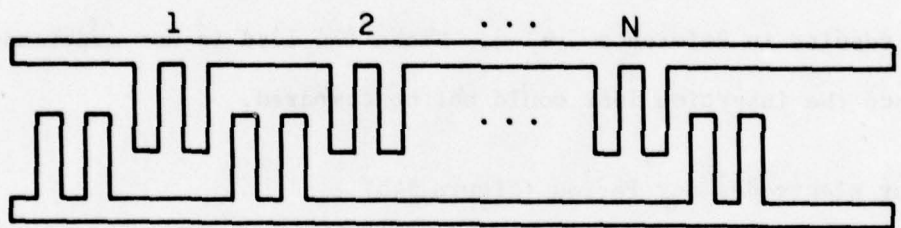
Using equation ( 92b ) for  $G_s$  this is seen to be the usual result.

To obtain the capacitance,  $\sum_n V_n V_{n-m}$  has to be evaluated for different value of m (equation ( 94 )). This is obtained as,

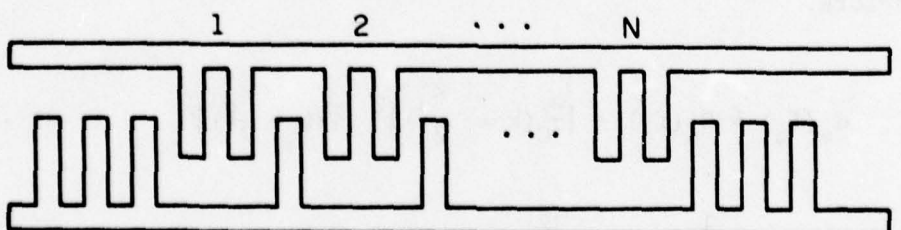
$$\begin{aligned} \sum_{n=1}^{N_E} V_n V_{n-m} &= N & m = 0 \\ &= 0 & m = \pm 1 \\ &= N - 1 & m = \pm 2 \end{aligned}$$



(a) Two Electrodes per Period



(b) Four Electrodes per Period



(c) Three Electrodes per Period

KP-1535

Figure 54. IDT structures

- a) two electrodes per period
- b) four electrodes per period
- c) three electrodes per period

The capacitance is therefore given by,

$$\begin{aligned} C &= C_s \cdot N [D_o + 2D_2] \text{ if } N \gg 1 \\ &= C_s \cdot N \end{aligned} \quad (105b)$$

since

$$D_o + 2D_2 = -2D_1 = 1$$

Figure ( 55a ) shows  $G_a$  as a function of frequency for 60 electrodes ( $N_E = 60$ ,  $N = 30$ ) and  $\eta = .45$ . The calculated capacitance agrees with the experimental results in Reference [ 45 ]. Since the load is not mentioned in the reference the insertion loss could not be compared.

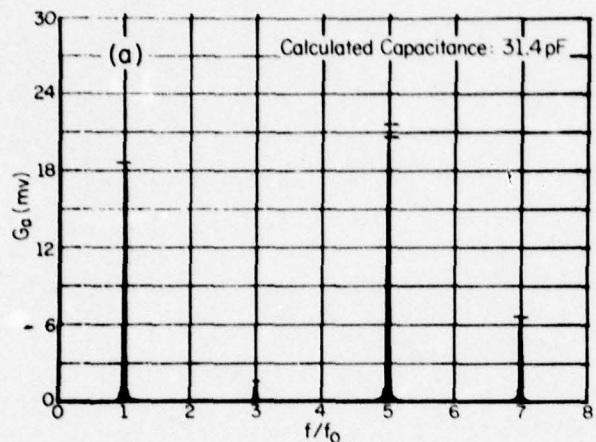
## 2. Four Electrodes per Period (Figure 54b)

In a double electrode transducer (four electrodes per period) the fundamental center frequency,  $f_c$  is half of  $f_o$ . The radiation conductance is therefore,

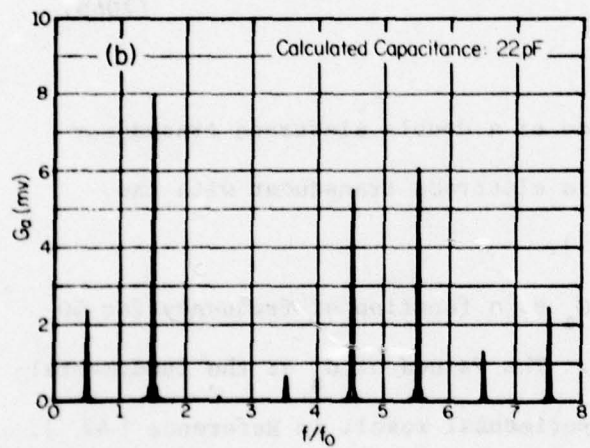
$$\begin{aligned} G_a(f_c) &= G_s(f_o) \cdot |\bar{\sigma}_G(k = \frac{k_o}{2})|^2 |\bar{v}(k = \frac{k_o}{2})|^2 \\ &= \frac{1}{2} G_s(f_o) N^2 \end{aligned} \quad (106a)$$

The  $f_o$  of a double electrode transducer is twice the  $f_o$  of a single electrode one for the same  $f_c$ . Thus, from ( 105a ) and ( 106b ) it is seen that  $G_a(f_c)$  is the same for both types of transducers with the same  $f_c$  and  $N$ . This agrees with Reference [ 42 ].

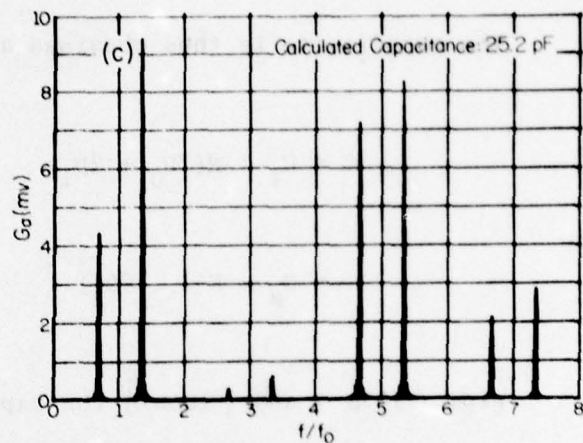
In this case, we obtain,



(a) Two Electrodes per Period



(b) Four Electrodes per Period



(c) Three Electrodes per Period

**Figure 55. Radiation conductance for IDT structures**  
**y-z LiNbO<sub>3</sub>, beam width = .274 cm**  
**60 electrodes p = 35 μm**  
**a) two electrodes per period**  
**b) four electrodes per period**  
**c) three electrodes per period**

In this case, we obtain,

$$\sum_{n=1}^{N_E} v_n v_{n-m} = 2N \quad m = 0$$

$$= N \quad m = +1$$

$$= 0 \quad m = -1$$

The capacitance is thus obtained as,

$$C = C_s \cdot N(2D_0 + 2D_1)$$

$$= C_s \cdot N(1 - 4D_2) \quad (106b)$$

From ( 105b ) and ( 106b ) the capacitance of a double electrode transducer is seen to be 1.4 times that of the single electrode transducer with the same N. This agrees with Reference [ 42 ].

Figure 55b shows a plot of  $G_a$  as a function of frequency for 60 electrodes ( $N_E = 60$ ,  $N = 15$ ) and  $\eta = .45$ . The values of  $G_a$  at the fundamental and the third harmonic agree with the experimental result in Reference [ 42 ].

### 3. Three Electrode per Period (Figure 54c)

In this case  $f_c = \frac{2}{3} f_o$ . The radiation conductance at the fundamental center frequency is therefore,

$$G_a(f_c) = \frac{1}{2} G_s(f_o) N^2 \quad (107a)$$

since  $\bar{\sigma}_G(k = 2k_o/3) = .7$  from Figure 48a.

Again, for the three electrode structure,

$$\sum_n V_n V_{n-m} = 2N \quad m = 0$$

$$= N \quad m = \pm 1$$

$$= N-1 \quad m = \pm 2$$

The capacitance is therefore,

$$C = C_s \cdot N(2D_0 + 2D_1 + 2D_2)$$

$$= C_s \cdot N(1 - 2D_2) \quad (107b)$$

From ( 105b ) and ( 107b ) the capacitance of this structure is seen to be 1.2 times that of the single electrode transducer.

Figure IX-10c shows a plot of  $G_a$  as a function of frequency for  $N_E = 60$ ,  $N = 20$  with  $\eta = .45$ . The calculated capacitance as well as the conductance at the fundamental and third harmonics agrees very well with the experimental results in Reference [ 42 ].

#### D. Conclusions

A simplified general theory of periodic interdigital transducers has been developed which provides harmonic responses and accounts for nearest neighbor interactions. This analysis is different from previous work in that the effect of electrode geometry on the excitation is accounted for by a suitably redefined element factor. Previous work has used the charge under a single electrode as the element factor. In this case the element factor varies from electrode to electrode and the transducer response does not separate into an array factor and an element factor. This work redefines the basis function as the charge under the single tap structure of Figure 46 . This basic charge distribution function is a complete solution of the electrostatic field equations; the charge distribution for an arbitrary sequence of voltages is obtained by a suitable translation and superposition of the basic charge distribution function. Using this approach the transducer response separates into an array factor and an element factor then simplifying filter analysis and design. The theory is sufficiently general to handle a nonapodized withdrawal weighted transducer with shorted elements, apodized transducers with shorted dummies, and capacity coupled structures. The inherent loss of apodized transducers and the coupling capacitors band limiting in capacity weighted structures are predicted. Filter synthesis is simplified since the single tap response is equalized simply by dividing the specified response by the element factor response before specifying the tap weights.

#### Acknowledgment

The authors have benefitted from many fruitful discussions with Dr. R. Adler.

## APPENDIX A

### TIME DOMAIN ANALYSIS PROCEDURE

The harmonic analysis steps are outlined in the flow chart (Figure 56). This technique begins with original frequency domain data from TETAM and manipulates it in such a way as to produce an expanded, high resolution impulse response of the segregated SAW excitation function. Each odd harmonic file is processed separately (due to file size limitations) and combined together at the end.

#### 1. Original data, deconvolution

The original data is a set of measured amplitude and phase at discrete frequency points ( $V_B/V_A$  and  $\phi_B - \phi_A$ , see Figure 64). In this example, the data is measured over the first seven harmonics (Figure 57) of two six double electrode unapodized  $15\lambda$  wide transducers fabricated on  $128^\circ \text{LiNbO}_3$ . This frequency domain harmonic data is deconvolved with the frequency response of the measurement system (Figure 58). The system response is created by replacing the test device with an attenuator whose attenuation is equal to the device insertion loss at the fundamental. The frequency responses are deconvolved by dividing the response magnitudes and subtracting their phases point by point.

#### 2. Phase slope adjustment

An initial frequency domain phase slope (time delay) adjustment is performed on the deconvolved data which will shift all time domain components and center the SAW impulse response about time zero (Figure 59). All harmonics are individually time shifted by the same amount as the fundamental. The amount of time shift is calculated by finding the phase slope between the -3db points of the frequency magnitude data. A least squares fit of the phase produces the slope which is subtracted and the process is applied again, repeating until the slope is zero within .01  $\Delta t$ .

### 3. Time domain filtering

After a fast Fourier transform from frequency to time, the data is truncated symmetrically about time zero (Figure 59). The time duration left must be greater than the total theoretical impulse response. To keep the file size down, the time data is shortened by a power of two, due to the FFT power of two dependence. Another Fourier transform from time to frequency is performed (Figure 60). Note that the response data is considerably smoother than the original, due to the absence of spurious responses in time.

### 4. Phase slope adjustment

At this point only the SAW components are present and a more accurate time shift to zero can be performed. Each harmonic is individually phase adjusted to zero slope and zero offset between the -3db magnitude points (Figure 60a,b). At this point the harmonic files are appended to one another to produce a transfer function as shown in Figure 61a,b.

### 5. Auto deconvolution

The auto-deconvolution process consists of two steps. First, the square root is taken of the frequency domain magnitude (Figure 62 a). Second, the phase is manipulated using a calculated phase response.

In auto-convolution frequency domain phases (from each transducer) the  $\pi$  radians are doubled to  $2\pi$  which cannot be differentiated from a phase of 0 radians in a mod  $2\pi$  system. For the case of auto-deconvolution, a theoretical calculated phase response is created using  $\sin x/x$  functions. The  $\sin x/x$  functions are centered about each odd harmonic and weighted by the square root of the experimental measured response at that harmonic. In places where the composite  $\sin x/x$  is negative, a phase shift of  $\pi$  is

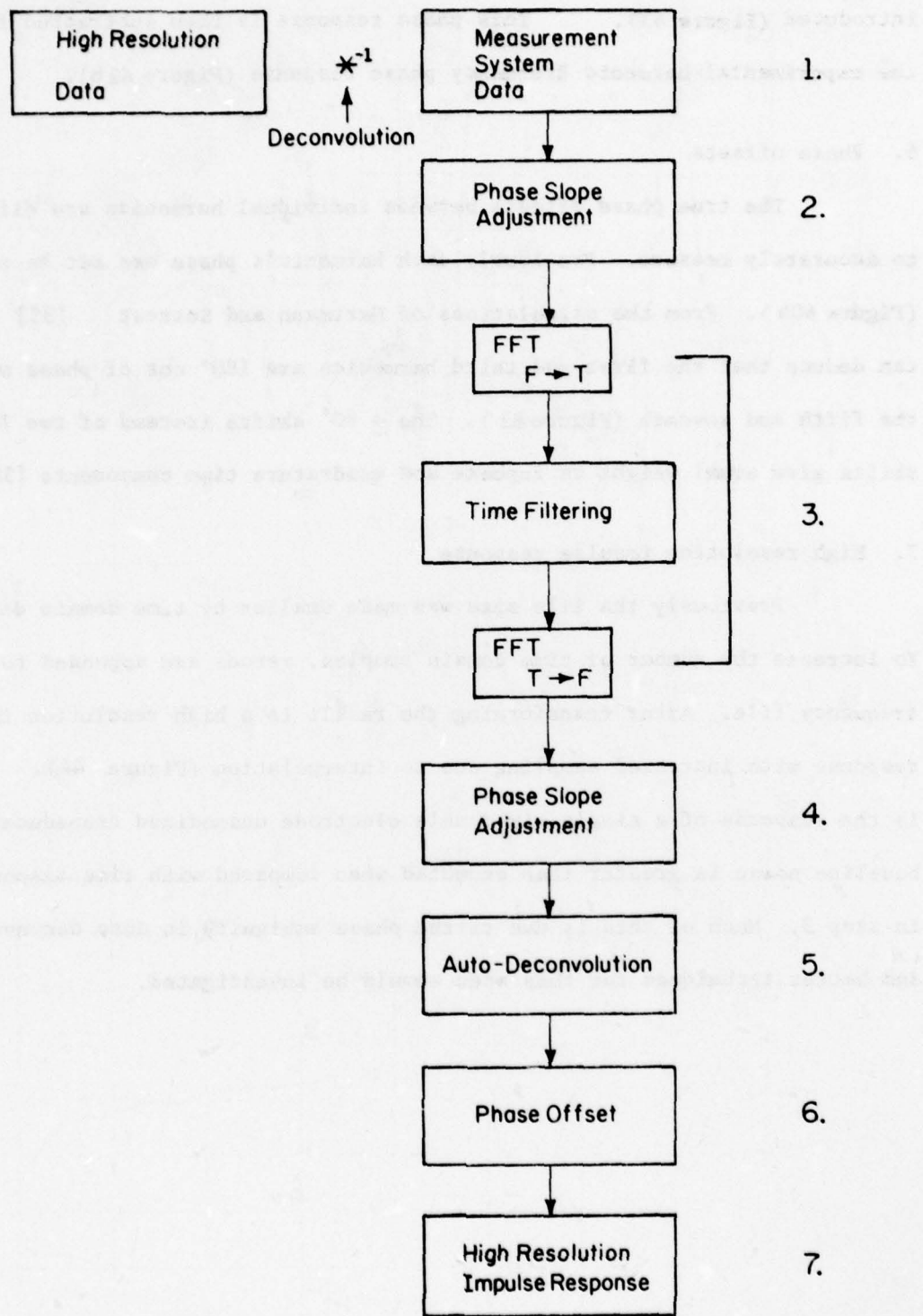
introduced (Figure 43). This phase response is then subtracted from the experimental harmonic frequency phase response (Figure 62 b).

#### 6. Phase offsets

The true phase offsets between individual harmonics are difficult to accurately measure. Previously each harmonic's phase was set to zero (Figure 60b). From the calculations of Hartmann and Secret [35] one can deduce that the first and third harmonics are  $180^\circ$  out of phase with the fifth and seventh (Figure 63). The  $\pm 90^\circ$  shifts instead of two  $180^\circ$  shifts give equal weight to inphase and quadrature time components [38]

#### 7. High resolution impulse response

Previously the file size was made smaller by time domain deletion. To increase the number of time domain samples, zeroes are appended to the frequency file. After transforming the result is a high resolution impulse response with increased sampling due to interpolation (Figure 44). This is the response of a single six double electrode unapodized transducer. The baseline noise is greater than expected when compared with time response data in step 3. Much of this is due to the phase ambiguity in auto deconvolution and better techniques for this step should be investigated.



KP-1518

Figure 56. Harmonic analysis flow chart

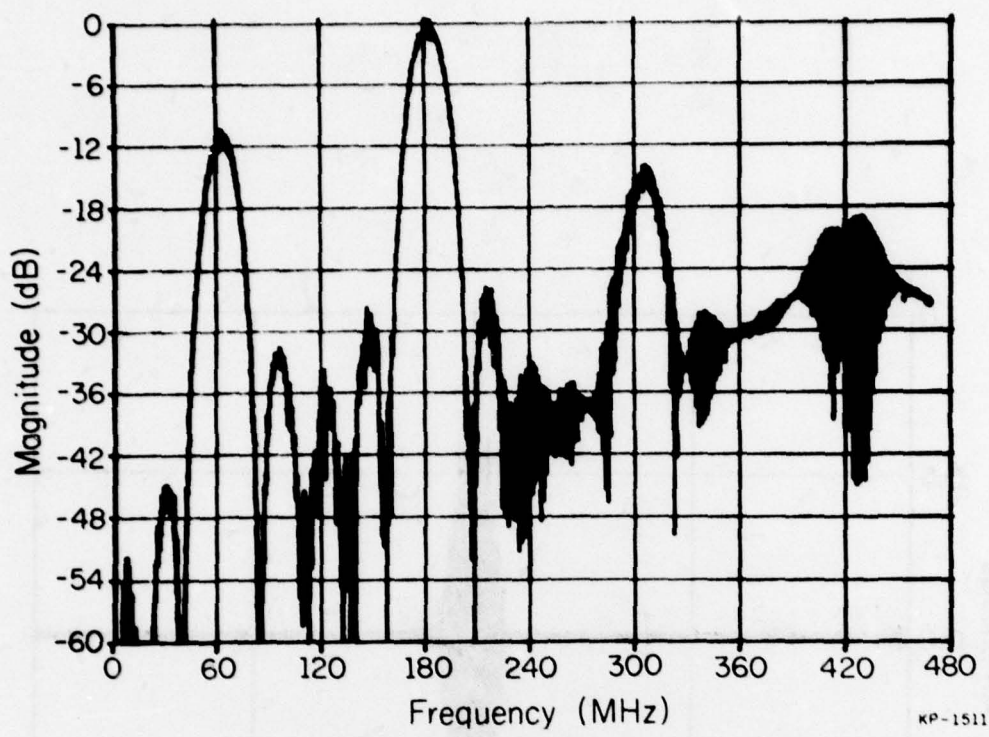


Figure 57. Original measured harmonic magnitude data

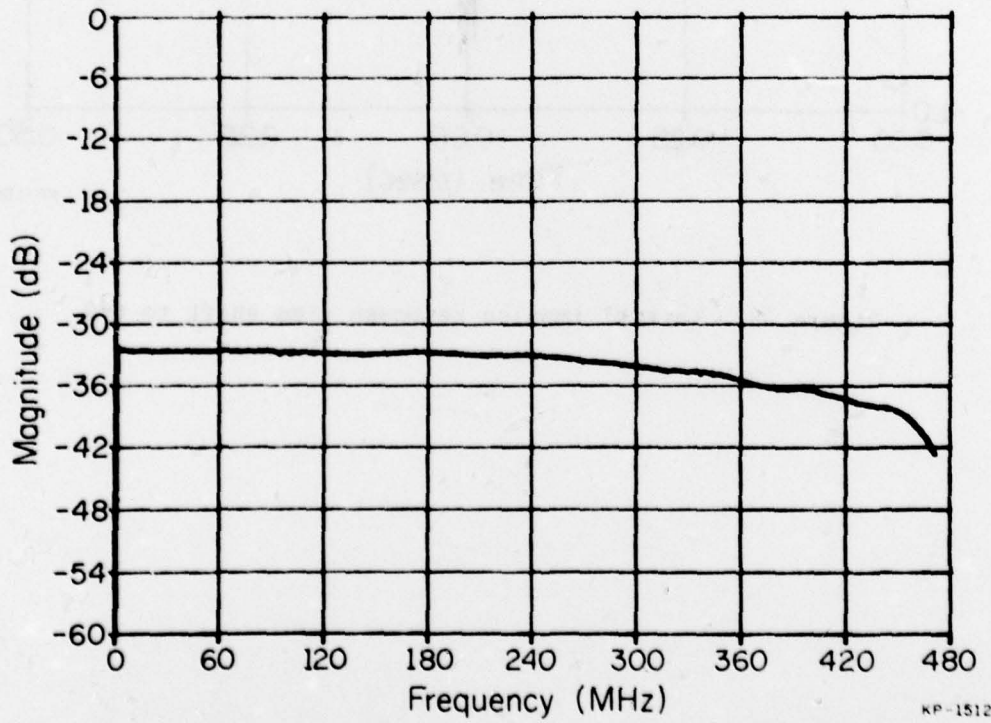


Figure 58. Measurement system harmonic frequency response magnitude

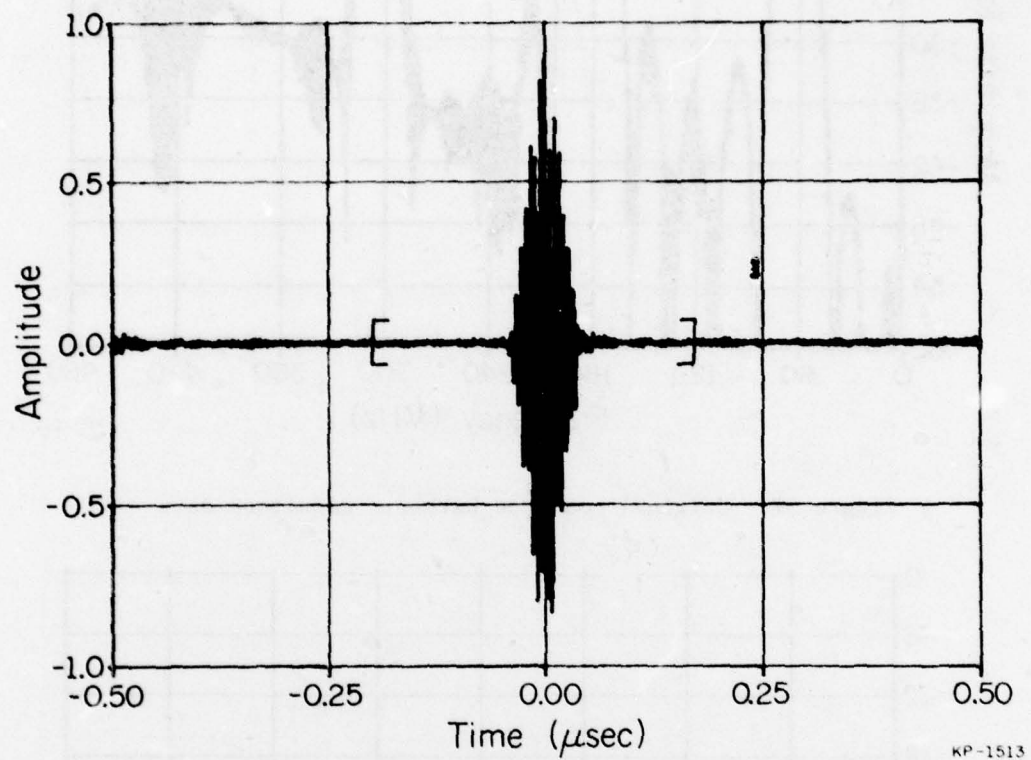
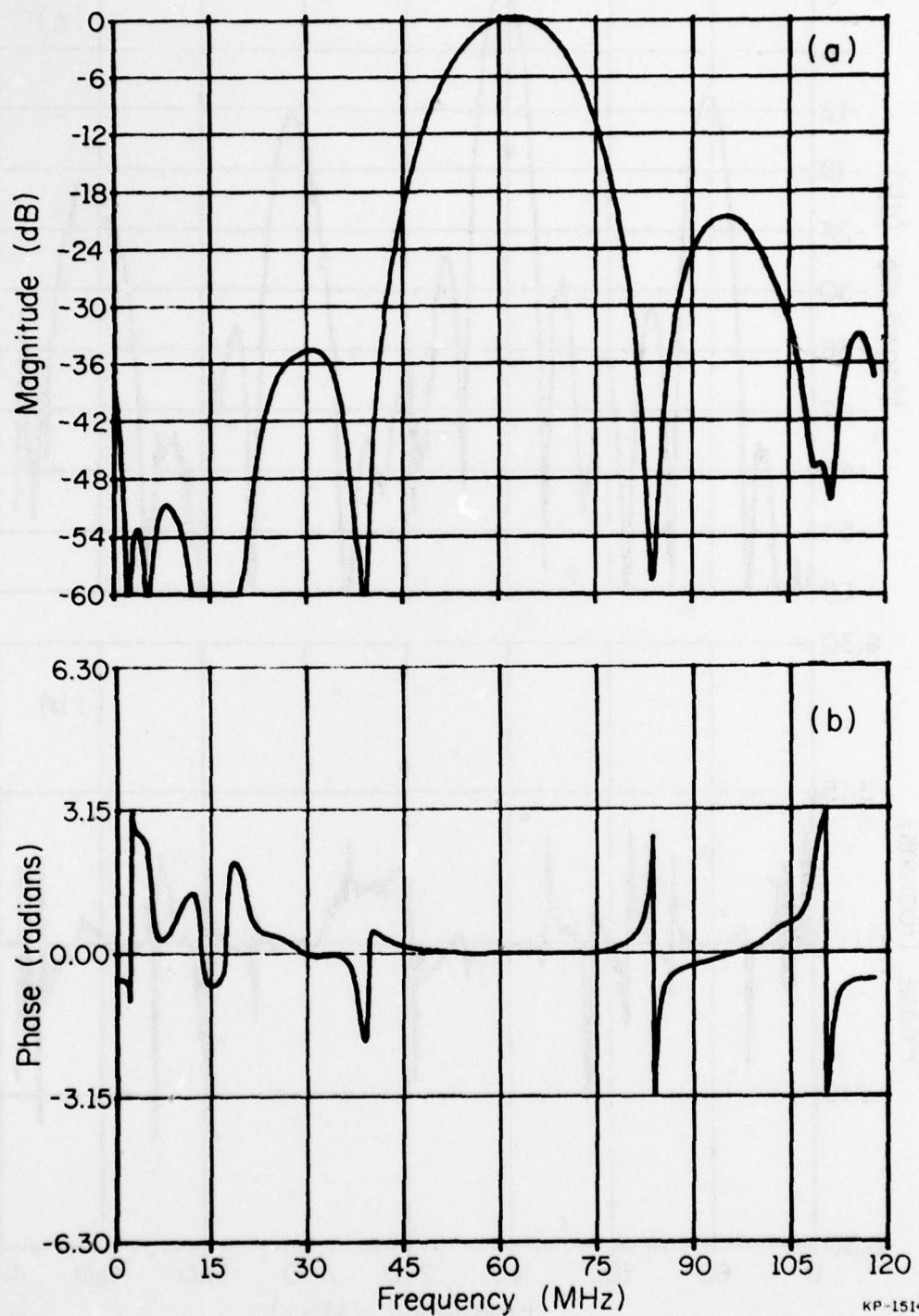


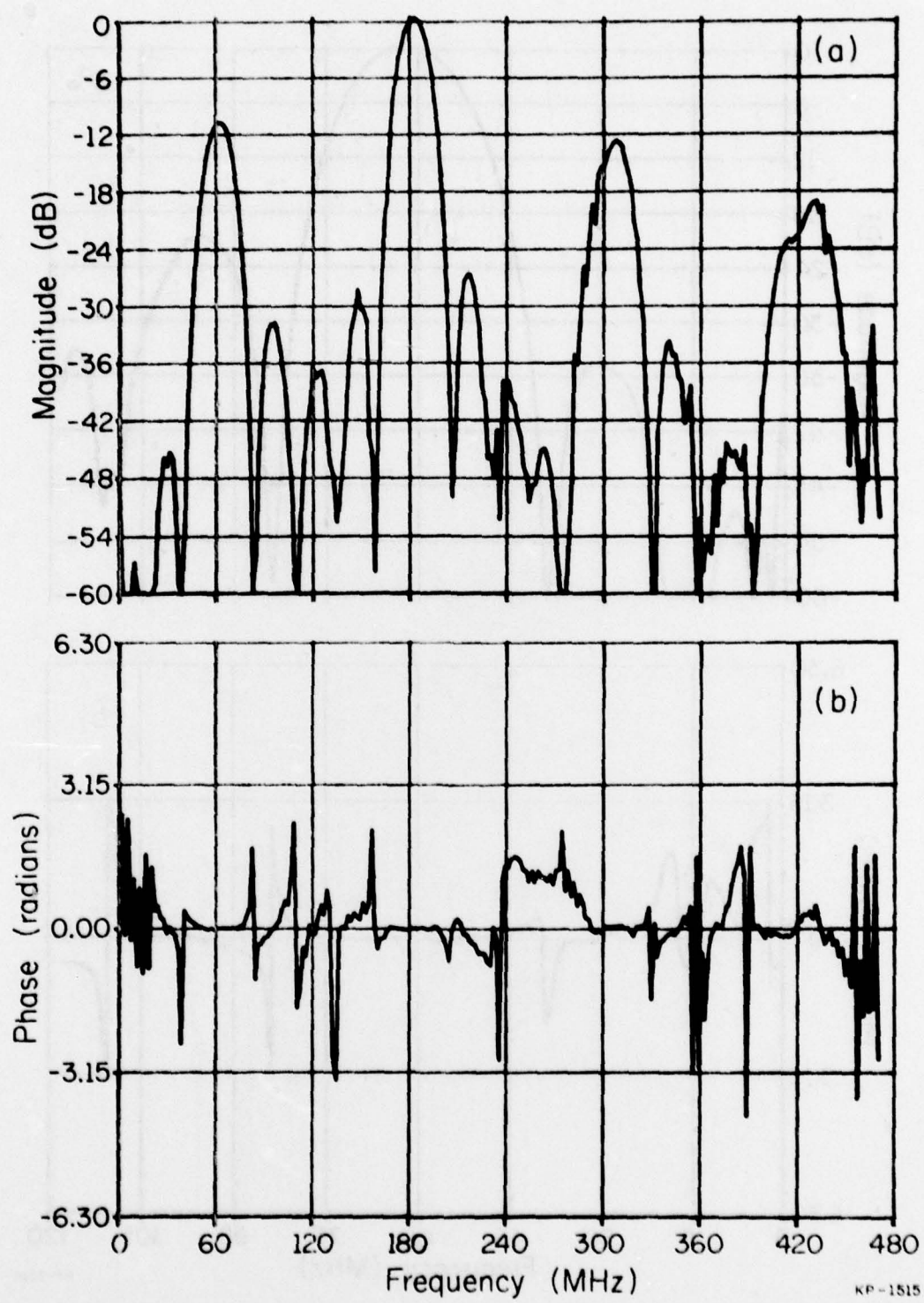
Figure 59. Initial impulse response time shift to  $t=0$



**Figure 60.** Frequency response of fundamental after deletion of all non-SAW time components.

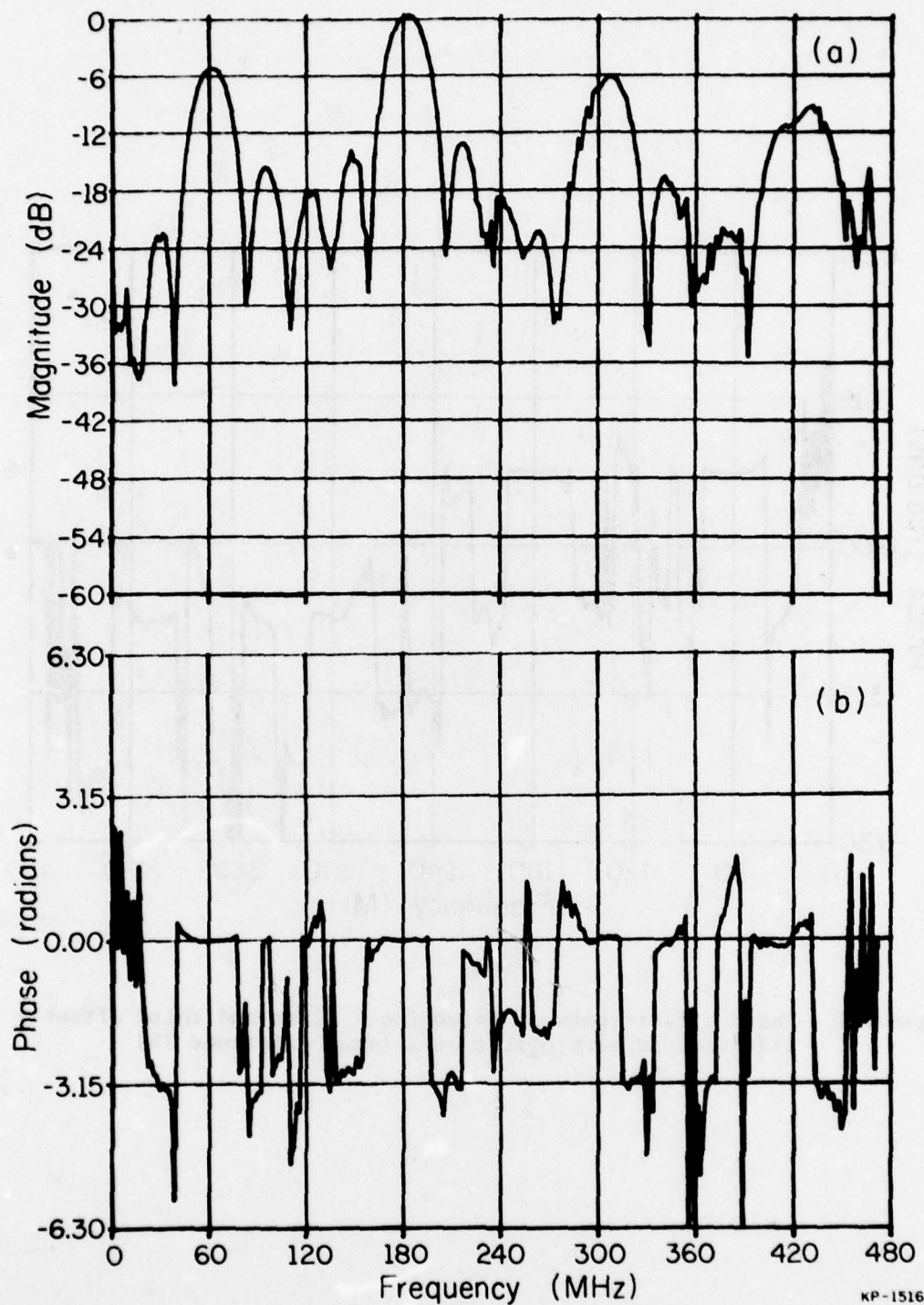
- a) magnitude
- b) phase

KP-1514



KP-1515

**Figure 61.** Composite frequency response  
 a) magnitude  
 b) phase



KP-1516

**Figure 62.** Auto deconvolution

a) square root of magnitude

b) phase response after subtraction of  
theoretical calculated phase response

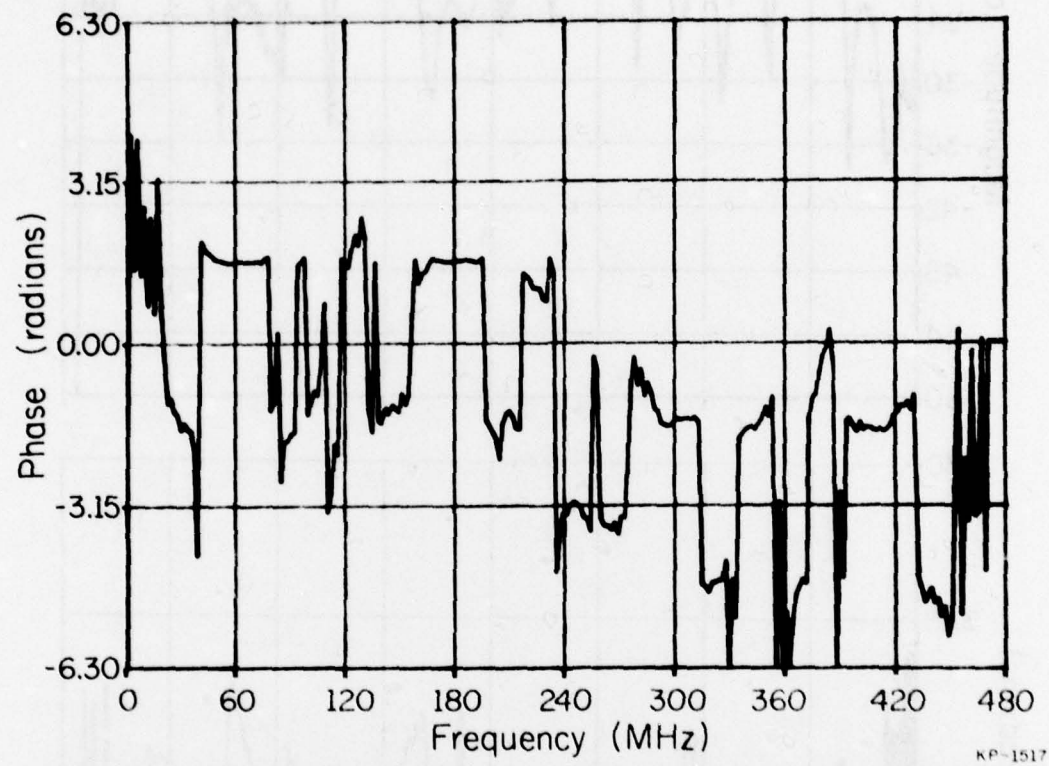


Figure 63. Phase offsets between harmonics. First and third offset  $\pm \pi/2$   
fifth and seventh offset  $-\pi/2$  [from Reference 35]

APPENDIX B  
TIME DOMAIN ANALYSES IMPLEMENTATION

The measurement system (Figure 64) consists of a digital computer and interface which control a frequency synthesizer, vector voltmeter and programmable attenuator. The computer calculates the specific frequency and programs the synthesizer through the interface. Two amplifiers are used as impedance buffers with an attenuator provided for system calibration runs. The signal levels of the vector voltmeter (ch B) and RF voltmeter (ch A) are read and converted into amplitude gain and phase shift across the buffered SAW device at this frequency.

Determinations are now made as to whether the magnitude and phase are in acceptable ranges. A programmable attenuator replaces the vector voltmeter range switch and is stepped until the magnitude is in range. The vector voltmeter phase reversal circuit has been accessed and is used to keep phase readings away from  $\pm 180^\circ$  where considerable error is introduced. The automatic phase control unlock light is also monitored. Once an acceptable signal level is read, the computer stores the data and sets the synthesizer to the next frequency, repeating the measurement process.

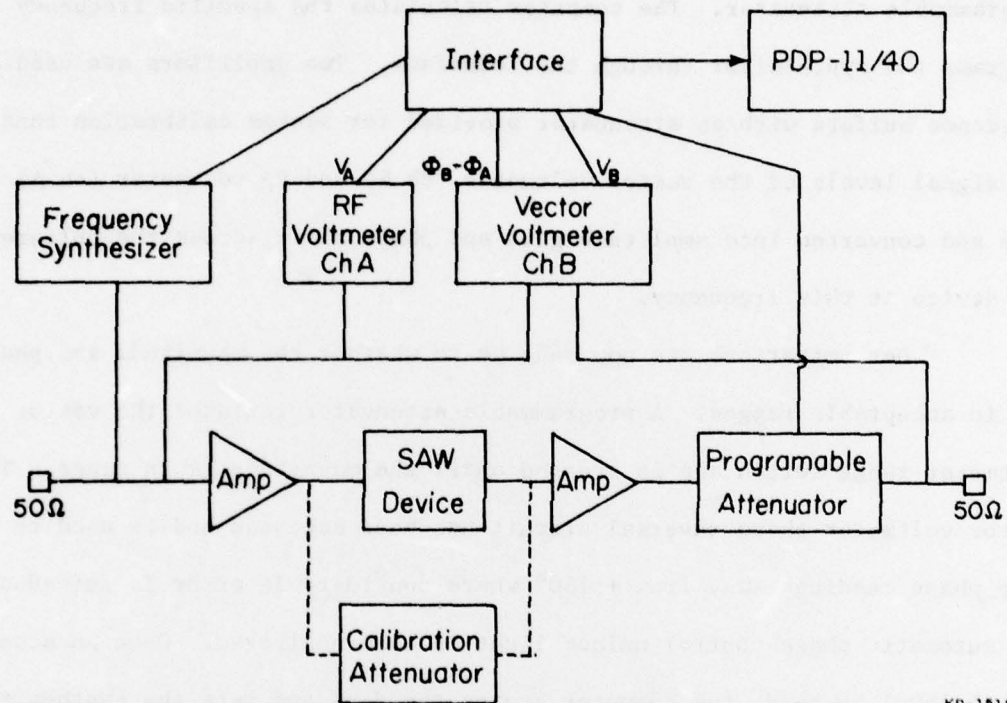


Figure 64. Measurement system block diagram.

APPENDIX C  
MODIFIED LAGUERRE POLYNOMIALS

The first three orthonormal functions are given below

$$f_0(x) = e^{-x/2}$$

$$f_1(x) = e^{-x/2}(1-x)$$

$$f_2(x) = e^{-x/2}(1-2x + \frac{1}{2}x^2)$$

$$f_3(x) = e^{-x/2}(1-3x + \frac{3}{2}x^2 - \frac{1}{6}x^3)$$

The recurrence formula satisfied by  $f_m(x)$  is

$$f_{m+1}(x) = \frac{2m+1-x}{m+1} f_m(x) - \frac{m}{m+1} f_{m-1}(x) .$$

The matrix elements  $M_{cd}$  are obtained by using the relations:

$$\langle j | m \rangle = \delta_{jm}$$

$$\begin{aligned} \frac{d}{dq} |m\rangle &= a_{mj} |j\rangle \quad \text{where } a_{mj} = -1 \quad j < m \\ &\quad = -1/2 \quad j = m \\ &\quad = 0 \quad j > m \end{aligned}$$

$$\begin{aligned} \frac{d^2}{dq^2} |m\rangle &= b_{mj} |j\rangle \quad \text{where } b_{mj} = m-j \quad j < m \\ &\quad = 1/4 \quad j = m \\ &\quad = 0 \quad j > m \end{aligned}$$

$$M_{11} = - \delta_{jm}$$

$$M_{12} = i \left( -\frac{1}{2} \delta_{jm} - \theta(m-j-1) \right)$$

$$M_{21} = i \left( 1 - \frac{1}{2} \delta_{jm} - \theta(m-j-1) \right)$$

$$M_{22} = \frac{1}{4} \delta_{jm} + (m-j) \theta(m-j-1) - (m + \frac{1}{2})$$

The multiplying factor  $i$  in  $M_{12}$  and  $M_{21}$  refers to  $\sqrt{-1}$ .

The matrix elements for  $H_{cd}$  and  $\langle j | \theta(q_2 - kh) | m \rangle$  are obtained by writing  $|m(q_2 + kh)\rangle$  as

$$|m(q_2 + kh)\rangle = a_{mj} |j(q_2)\rangle$$

where coefficients  $a_{mj}$  are to be elevated. It is obvious that

$$a_{00} = e^{-kh/2}$$

$$a_{10} = -kh \cdot e^{-kh/2}$$

$$a_{11} = e^{-kh/2}$$

Other coefficients are obtained using the recursion relation

$$a_{m+1,j} = \frac{1}{m+1} [a_{mj}(2m-2j-kh) - ma_{m-1,j} + ja_{m,j-1} + (j+1)a_{m,j+1}]$$

## REFERENCES

1. D. Malocha and B. J. Hunsinger, "Capacitive Weighted Tap SAW Transducers," IEEE Ultrasonics Symposium, 411-413 (1975).
2. D. Malocha and B. J. Hunsinger, "Capacitive Tap Weighted SAW Transducers," IEEE Trans. on Sonics and Ultrasonics, 24, 293-301 (1977).
3. D. Malocha and B. J. Hunsinger, "Capacitive Tap Weighted SAW Transducers with Reduced Losses," IEEE Ultrasonic Symposium (1977).
4. C. S. Hartmann, et al., "Impulse Model Design of Acoustic Surface Wave Filters," IEEE Trans. on Sonics and Ultrasonics, 20, 80-93 (1973).
5. B. J. Hunsinger and R. J. Kansy, "SAW Filter Sampling Techniques," IEEE Trans. on Sonics and Ultrasonics, 22, 270-273 (1975).
6. W. R. Smith and W. F. Pedler, "Fundamental and Harmonic Frequency Circuit Model Analysis of Interdigital Transducers with Arbitrary Metallization Ratios and Polarity Sequences," IEEE Trans. on Microwave Theory and Techniques, 23, 853-864 (1975).
7. D. C. Malocha, S. Datta and B. J. Hunsinger, "Tap Weight Enhancement for Broadband Filters," IEEE Trans. on Sonics and Ultrasonics, 25, 51-54 (1978).
8. C. S. Hartmann, "Weighting Interdigital Surface Wave Transducers by Selective Withdrawal of Electrodes," IEEE Ultrasonics Symposium Proceedings, pp. 423-426, 1973.
9. W. J. Tanski, "Technique for Capacitive Voltage Weighting Inter-digital Surface Acoustic Wave Transducers," Applied Physics Letters, 26, pp. 35-37, 1975.
10. B. R. Potter and C. S. Hartmann, "Low Loss Surface Acoustic Wave Filters", IEEE Trans. on Parts, Hybrids and Packaging, 13, pp. 348-353, 1977.
11. D. C. Malocha and B. J. Hunsinger, "Reduced Reactance Capacitively Weighted Transducers", to be published.
12. F. Yamanouchi, F. Nyffeler and K. Shebayama, "Low Insertion Loss Acoustic Surface Wave Filter Using Group Type Nondirectional Transducer", 1975 Ultrasonics Symposium, pp. 317-321.
13. R. C. Rosenfeld, R. B. Brown and C. S. Hartmann, "Unidirectional Acoustic Surface Wave Filters with 2 dB Insertion Loss", 1974 Ultrasonics Symposium, pp. 425-428

14. D. C. Malocha and B. J. Hunsinger, "Group Type Capacitively Weighted Unidirectional Transducers for Highly Selective Filters", to be published.
15. W. R. Jones, J. J. Campbell and S. L. Veilleux, Final Report to AFCRL, Contract No. F19628-69-C-0132.
16. L. P. Solie, J. App. Phys., 619 (1973).
17. A. A. Maradudin, R. F. Wallis, D. L. Mills and R. L. Ballard, Phys. Rev. B 6, 1106 (1972).
18. S. L. Moss, A. A. Maradudin and S. L. Cunningham, Phys. Rev. B 8, 2999 (1973).
19. T. M. Sharon, Proc. IEEE Ultrasonics Symposium, 126 (1973).
20. A. A. Maradudin, Jap. J. App. Phys., Suppl. 2, Pt. 2, 871 (1974).
21. S. Datta and B. J. Hunsinger, Phys. Rev. B (to be published).
22. W. Ludwig and B. Lengeler, Solid State Commun. 2, 83 (1964).
23. A. A. Maradudin, E. W. Montroll, G. H. Weiss and I. P. Ipatovia, Theory of Lattice Dynamics in the Harmonic Approximation, 2nd ed. (Academic, New York,) pp. 524, (1971).
24. The use of the  $\theta$ -function in the constitutive relations equations (43 a) and (43 b) satisfies the boundary conditions only in the sense of distributions. However, this makes possible a semivariational determination of the dispersion relation as discussed in Reference 17 for an infinite quarter space and in References 22 and 23 for an infinite half space.
25. B. A. Auld and G. S. Kino, IEEE Transactions Ed-18, 898 (1971).
26. T. E. Parker and M. B. Schultz, Proc. IEEE Ultrasonics Symposium, 295 (1974).
27. F. G. Marshall, C. O. Newton and E. G. S. Paige, IEEE Trans., MIT-21, 216 (1973).
28. K. Blotekjaer, K. A. Ingebrigtsen and H. Skeie, IEEE Trans., ED-20, 1139 (1973).
29. C. Maerfeld, Wave Electronics, 2, 82 (1976).
30. G. S. Kino and W. R. Shreve, J. Appl. Phys., 44, 3960 (1973).
31. C. W. Chapman and T. W. Bristol, Research and Development Technical Report, Hughes Aircraft Company, ECOM-73-0276-F.

32. S. G. Joshi and P. Sudhakar, IEEE Trans., SU-24, 201 (1977).
33. H. Engan, "Surface Acoustic Wave Multielectrode Transducers," IEEE Trans. on Sonics and Ultrasonics, Vol. SU-22, No. 6, pp. 395-401, (1975).
34. H. Engan, "Excitation of Elastic Surface Waves by Spatial Harmonics of Interdigital Transducers," IEEE Trans. on Electron Devices, Vol. ED-16, pp. 1014-1017, Dec. 1969.
35. C. S. Hartmann and B. G. Secrest, "End Effects in Interdigital Surface Wave Transducers," in 1972 IEEE Ultrasonics Symp. Proc., pp. 413-416, Oct., 1972.
36. A. J. Bahr and R. E. Lee, "Equivalent Circuit Model for Interdigital Transducers with Varying Electrode Widths," Electronics Letters, Vol. 9, pp. 281-282, June 28, 1973.
37. T.L. Szabo, K. R. Laker and E. Cohen, "Accurate IDT Design Using Spectral Weighting," in 1976 IEEE Ultrasonics Symp. Proc., pp. 543-546, Oct., 1976.
38. C. M. Panasik and B. J. Hunsinger, "Precise Impuse Response Measurement of SAW Filters," IEEE Trans. On Sonics and Ultrasonics, Vol. SU-23, No. 4, July, 1976.
39. K. R. Laker, E. Cohen and A. J. Slobodnik, "Electric Field Interactions within Finite Arrays and the Design of Withdrawal Weighted SAW Filters at Fundamental and Higher Harmonics," Proc. IEEE Ultrasonics Symposium (1976).
40. B. J. Hunsinger, "Surface Acoustic Wave Universal Blank Study", Interim Report AF Contract No. F33615-75-C-1291.
41. W. R. Smith and W. F. Pedler, "Fundamental-and Harmonic-Frequency circuit Model Analysis of Interdigital Transducers with Arbitrary Metallization Ratios and Polarity Sequences," IEEE Trans. on Microwave Theory and Techniques, Vol. MTT-23, No. 11, Nov. 1975, pp. 853-864.
42. H. Engan, "Surface Acoustic Wave Multielectrode Transducers," IEEE Trans. on Sonics and Ultrasonics, Vol. SU-22, No. 6, Nov. 1975, pp. 395-401.
43. K. R. Laker, E. Cohen and A. J. Slobodnik, "Electric Field Interactions within Finite Arrays and the Design of Withdrawal Weighted SAW Filters at Fundamental and Higher Harmonics," Proc. IEEE Ultrasonics Symposium (1976).
44. T. L. Szabo, K. R. Laker and E. Cohen, "Accurate IDT Design Using Spectral Weighting", Proc. IEEE Ultrasonics Symposium (1976).

45. D. C. Malocha and B. J. Hunsinger, "Capacitive Tap Weighted SAW Transducers", IEEE Trans. on Sonics and Ultrasonics, Vol. SU-24, No. 5, Sept. 1977.
46. B. J. Hunsinger, "Surface Acoustic Wave Universal Blank Study", Interim Report AF Contract No. F33615-75-C-1291.